

March 2017

Ph.D. in Electrical and Electronics Engineering

AHMED MAMOON MAHMOOD

**UNIVERSITY OF GAZIANTEP
GRADUATE SCHOOL OF
NATURAL & APPLIED SCIENCES**

**ELECTROMAGNETIC BANDGAP METAMATERIALS AS THE
COMBINATION OF INDUCTIVE AND CAPACITIVE
RESONATORS**

**Ph.D. THESIS
IN
ELECTRICAL AND ELECTRONICS ENGINEERING**

**BY
AHMED MAMOON MAHMOOD
30 March 2017**

**Electromagnetic Bandgap Metamaterials as the Combination of
Inductive and Capacitive Resonators**

Ph.D. Thesis

in

Electrical and Electronics Engineering

University of Gaziantep

Supervisor

Assoc. Prof. Dr. Gölge ÖGÜCÜ YETKİN

Co-Supervisor

Assoc. Prof. Dr. Cumali SABAHA

by

AHMED MAMOON MAHMOOD

March 2017



© 2017 [Ahmed Mamoon MAHMOOD]


REPUBLIC OF TURKEY
UNIVERSITY OF GAZIANTEP
GRADUATE SCHOOL OF NATURAL & APPLIED SCIENCES
Electrical and Electronics Engineering

Name of the thesis: Electromagnetic bandgap metamaterials as the combination of inductive and capacitive resonators

Name of the student: Ahmed Mamoon MAHMOOD

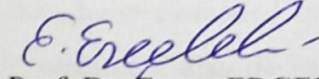
Exam date: 30/03/2017

Approval of the Graduate School of Natural and Applied Sciences


Prof. Dr. A. Necmeddin YAZICI

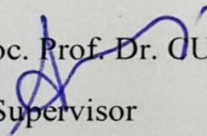
Director

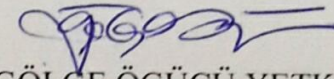
I certify that this thesis satisfies all the requirements as a thesis for the Doctor of Philosophy.


Prof. Dr. Ergun ERÇELEBİ

Head of Department

This is to certify that we have read this thesis and that in our consensus/majority opinion it is fully adequate, in scope and quality, as a thesis for the degree of Doctor of Philosophy.


Assoc. Prof. Dr. CUMALİ SABAH
Co-Supervisor


Assoc. Prof. Dr. GÖLGE ÖGÜCÜ YETKİN
Supervisor

Examining Committee Members

Prof. Dr. SAVAŞ UÇKUN

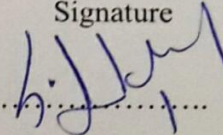
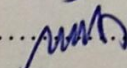
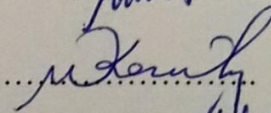
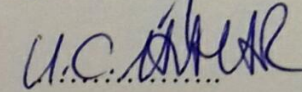
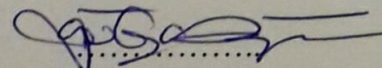
Assoc. Prof. Dr. EMİN ÜNAL

Assoc. Prof. Dr. MUHARREM KARAASLAN

Assoc. Prof. Dr. UĞUR CEM HASAR

Assoc. Prof. Dr. GÖLGE ÖGÜCÜ YETKİN

Signature


.....

.....

.....

.....

.....

I hereby declare that all information in this document has been obtained and presented in accordance with academic rules and ethical conduct. I also declare that, as required by these rules and conduct, I have fully cited and referenced all materials that are not original to this work.

Ahmed Mamoon MAHMOOD

ABSTRACT

ELECTROMAGNETIC BANDGAP METAMATERIALS AS THE COMBINATION OF INDUCTIVE AND CAPACITIVE RESONATORS

MAHMOOD, AHMED MAMOON

Ph.D. in Electrical and Electronics Eng.

Supervisor: Assoc. Prof. Dr. Gülge ÖGÜCÜ YETKİN

Co-Supervisor: Assoc. Prof. Dr. Cumali SABAH

March 2017

88 pages

In this study, first, a novel MTM, which exhibits a wideband double negative behavior in X-band and is comprised of a modified S-shaped split-ring resonators (S-SRR), is proposed, designed and investigated both numerically and experimentally. This MTM has been used in an MTM absorber (MA) application. The proposed MA provides a stable frequency response for $\theta < 40^\circ$. Maximum absorption rate is 99.99% at 8.912 GHz with absorption over 90% in 8.825-9.0 GHz.

A fishnet-mushroom-like MTM is the next MTM studied. The electromagnetic behaviour of this structure is provided in terms of S-parameters numerically and experimentally for X-band frequency regime. The proposed design provides an electromagnetic bandgap (EBG) characterization with desired characteristic parameters; i.e. a double negative left-handed region in X-band with negative permittivity and negative permeability. This EBG is utilized to reduce the mutual coupling between arrays of antennas. The simulation results prove that the isolation has been improved while the radiated fields of the antennas are not affected by the EBG structure.

Keywords: Metamaterial, electromagnetic bandgap structure, absorber, mutual coupling reduction.

ÖZET

INDÜKTİF VE KAPASİTİF REZONETÖRLERİN BİRLEŞİMİNDEN OLUŞAN ELEKTROMANYETİK BANTARALIKLI METAMATERYALLER

MAHMOOD, Ahmed Mamoon

Doktora Tezi, Elektrik-Elektronik Müh. Bölümü

Tez Yöneticisi: Doç. Dr. Gölge ÖGÜCÜ YETKİN

Yardımcı Tez Yöneticisi: Doç. Dr. Cumali SABAH

Mart 2017

88 sayfa

Bu çalışmada ilk olarak X bandında geniş bantlı çift negatif özellik sergileyen ve modifiye S şeklinde parçalı halka rezonatörlerinden (S-SRR) oluşan yeni bir MTM numerik ve deneysel olarak önerilmekte, tasarlanmakta ve araştırılmaktadır. Bu MTM, MTM soğurucu (MA) uygulamasında kullanılmıştır. Önerilen MA $\theta < 40^\circ$ için kararlı bir frekans tepkisi vermiştir. Maksimum soğurma oranı, 8.825-9.0 GHz aralığında %90'nın üzerinde olmakla birlikte 8.912 GHz'te %99.99'tir. Üretilmiş prototipin deneysel sonuçları nümerik simülasyonlarla uyumluluk göstermektedir.

Balık ağı-mantar biçimli MTM çalışılan bir diğer MTMdir. Bu yapının elektromanyetik davranışı, X bandı frekans rejimi için S-parametreleri ile sayısal ve deneysel olarak temsil edilmektedir. Önerilen tasarım, arzu edilen karakteristik parametrelerle, yani X bandında negatif elektrik geçirgenliği ve negatif manyetik geçirgenliği olan çift negatif sol-elli bölgeyle, bir elektromanyetik bant aralığı (EBG) özelliği sunmuştur. Bu EBG, anten dizileri arasında karşılıklı bağlaşımı azaltmak için kullanılmıştır. Simülasyon sonuçları, antenin ışıma alanlarının EBG yapısından etkilenmemesi ile birlikte izolasyonun geliştiğini ortaya koymuştur.

Anahtar Kelimeler: Metamalzemeler, elektromanyetik bant aralıklı yapılar, soğurucu, karşılıklı bağlaşımı düşürme



To my parents and to my beloved wife, for their love, support and understanding

ACKNOWLEDGMENTS

The author wishes to express his deepest gratitude to his supervisor Assoc. Prof. Dr. Gölge Ögücü Yetkin and co-supervisor Assoc. Prof. Dr. Cumali Sabah for their guidance, advice, criticism, encouragements and insight throughout the research.

I would like to express my appreciation and gratefulness to my colleges special Mr. Ahmed Mahros for his help.

I would like to express my special appreciation and gratefulness to my father Mr. Mamoon Alkadi for his endless favors and his support during my study and my life.

I would like to express my thanks to my family, my mother, wife, sister and brother for their support to me.

TABLE OF CONTENTS

	Page
ABSTRACT	v
ÖZET	vi
ACKNOWLEDGMENTS	viii
TABLE OF CONTENTS	ix
LIST OF FIGURES	xii
LIST OF TABLES	xvi
LIST OF ABBREVIATIONS	xvii
CHAPTER 1	1
INTRODUCTION	1
1.1 Historical Background	1
1.2 Motivation and Objectives	5
1.3 Thesis organization	6
CHAPTER 2	7
METAMATERIAL ^[1] _[SEP]	7
2.1 Metamaterial theory	7
2.1.2 Electromagnetic wave propagation in metamaterials	9
2.1.3 Metallo-dielectric representation of metamaterials	12
2.2 Metamaterial Classification	14
2.3 Snell's Law and Negative Refraction	15
2.4 Dispersion Diagram	17
2.4.1 Brillouin Zone	18
2.4.2 Dispersion Diagram and Photonic Band Gap	19
2.5 Metallo-Dielectric Structures	21
2.5.1 SRR MTMs	21

2.5.2 Electromagnetic Bandgap MTMs	22
2.6 Surface waves	23
2.7 Microstrip Antenna Design.....	27
2.8 Microstrip Antenna Array and Mutual Coupling Reduction	28
2.9 Boundary Conditions	29
2.10 Nicholson-Ross-Weir Tecnique	29
2.11 Computer Simulation Technology.....	30
CHAPTER 3	30
METHODOLOGY	30
3.1 Metamaterials Flowchart Design.....	31
3.2 S-Shaped Split-Ring Resonator Design Specification.....	31
3.2.1 Simulation and Boundary Conditions	32
3.2.2 Experimental Method.....	33
3.2.3 Absorber Application	35
3.3 Fishnet-Mushroom-like MTMs Structure Modeling	36
3.3.1 Fishnet-Mushroom-like MTMs Design Specification	36
3.3.2 Array Structure Design and Simulations settings.....	37
3.3.3 Dispersion Diagram.....	38
3.3.4 EBG Experimental Method.....	39
3.5 Mutual Coupling Reduction Application.....	39
3.5.1 Microstrip Antenna Characteristics.....	39
3.5.2 Microstrip Two Array Antennas Structure.....	40
3.5.3 Microstrip Antenna Characteristics.....	41
CHAPTER 4	43
RESULTS AND DISCUSSION.....	43
4.1.1 S-SSR RESULTS	43
4.1.2 Electric Field, Magnetic Field and Surface Current Distributions	46
4.1.3 Absorber Application and Result	48
4.2 Fishnet Mushroom-Like EBG Results.....	52
4.2.1 Dispersion Diagram and EBG Location.....	52
4.2.2 S-Parameters and reiterative characteristic parameters	53
4.2.3 Simulated and Measured Results for 4x8 Array Arrangement	56
4.2.4 Mutual Coupling Reduction of Dual-Band For Two Microstrip Antennas.....	59
4.2.5 Mutual Coupling Reduction of Dual-Band Microstrip Antennas	68

CHAPTER 5	73
CONCLUSION	74
CHAPTER 6	76
Future Research	76
REFERENCES	77



LIST OF FIGURES

		Page
Figure 1. 1	Left-handed metamaterial at lens consisting of 3D an array arrangement with metamaterial unit cells.	4
Figure 2. 1	Electric field propagation direction magnetic with direction of propagation.	8
Figure 2. 2	Wave traveling in two different materials with $n_1, n_2 > 0$	8
Figure 2. 3	Incident wave propagating in positive medium index to negative medium index material.	9
Figure 2. 4	(a) right-handed material, (b) left-handed material.	11
Figure 2. 5	The general circuit representation of a (MD) unit cell.	12
Figure 2. 6	The Possible unit cell realizations of metallo-dielectric periodic structures as (a) DPS, (b) ENG, (c) MNG, (d) DNG.	13
Figure 2. 7	The material classifications depending on the Permittivity-permeability (ϵ - μ) real value.	15
Figure 2. 8	Propagation of a wave that incident on a DPS-DNG interface.	15
Figure 2. 9	Conventional material rays refraction.	17
Figure 2. 10	Left-handed material rays refraction.	17
Figure 2. 11	(a) The physical lattice of an EBG made using a square lattice. An arbitrary vector r is shown. b) The Brillouin zone of the reciprocal lattice, centered at the origin (Γ) An arbitrary wave vector k is shown. The irreducible Brillouin zone is the light blue triangular edge. The special points at the center, corner and face are conventionally known as Γ , M and X.	18
Figure 2. 12	(a) Dispersion relation (band diagram), (b) Bandgap has	

	been opened.	19
Figure 2. 13	a) A two-dimensional dispersion diagram for a two-dimensional EBGs [illustrated in xii Figure. (2.12)], in which a complete bandgap is shown by the light blue color; b) A two-dimensional dispersion diagram where an incomplete bandgap can be found.	20
Figure 2. 14	Different geometries for modified SRR.	21
Figure 2. 15	Different EBGs geometry: (a) rabbet spiral EBG structure [51], (b) uniplanar EBG[52].....	22
Figure 2. 16	Surface wave propagation inside the grounded dielectric slab	24
Figure 2. 17	Surface wave on an impedance surface.	24
Figure 2. 18	Microstrip schematic (Top view).....	27
Figure 3. 1	CSTWs flowchart program of designing metamaterial unit cell.	31
Figure 3. 2	The proposed S-SRR unit cell.	32
Figure 3. 3	The proposed unit cell simulations setting the boundary conditions.	33
Figure 3. 4	Location of excitation ports.	33
Figure 3. 5	Vector network analyser, two horn antennas with coaxial cables.	34
Figure 3. 6	S-SRR manufactured sample.	35
Figure 3. 7	Absorption experiment setting.....	35
Figure 3. 8	The EBG unit cell schematic, (a) side view, (b) top view.....	36
Figure 3. 9	EBG array simulation settings achieved by the bandgap	37
Figure 3.10	Dispersion diagram boundary conditions setting.....	38
Figure 3. 11	Experimental set-up schematic representation (VAN) vector network analyzer.	39
Figure 3. 12	Microstrip antenna top view.	40
Figure 3. 13	(a) two coupling antennas w/o EBG, (b) two coupling antennas	

	with EBG.....	41
Figure 3. 14	Top view for microstrip antennas schema, (a) without EBG (b) with EBG.	42
Figure 4. 1	S-SRR simulated and measured S-parameters magnitude (dB).....	43
Figure 4. 2	S-SRR simulated and measured S-parameters, reflection phase (degrees).....	44
Figure 4. 3	The simulated and experimental results for the real parts of, (a) permittivity (b) permeability and (c) refractive index.....	45
Figure 4. 4	The surface current distribution at 10.75 GHz.	47
Figure 4. 5	(a) Electric field, (b) magnetic field distributions for the proposed unit cell at 10.75 GHz.....	48
Figure 4. 6	Reflection and absorption ratio simulated and measured results.	49
Figure 4. 7	Frequency response of for different polarization angles $\theta = 0^\circ$ and ϕ varies, (b) θ varies and $\phi = 0^\circ$	50
Figure 4. 8	Absorption for different polarization angles, (a) θ varies and $\phi = 0^\circ$ (b) $\theta = 0^\circ$ and $\phi = 0^\circ$	51
Figure 4. 9	EBG Dispersion Diagram.	52
Figure 4. 10	3x8 Array arrangement, simulated parameters (a) magnitude in dB (b) phase in degree, (c) retrieval characteristic parameters.....	53
Figure 4. 11	4x8 Array arrangement Simulated parameters, (a) magnitude in dB, (b) phase in degree, (c) retrieval characteristic parameters.....	54
Figure 4. 12	6x8 Array arrangement Simulated parameters, (a) magnitude in dB, (b) phase in degree, (c) retrieval characteristic parameters.....	54
Figure 4. 13	(a) The simulated 4x8 arrangement sample, (b) the fabricated 4x8 arrangement sample.....	56
Figure 4. 14	Comparison of the simulated and measured S-parameters.....	57
Figure 4. 15	Comparison of the simulated and measured retrieval characteristic parameters.....	57
Figure 4. 16	SNG and DNG regions.	58
Figure 4. 17	The return loss and the coupling coefficient (a)without EBG structure, (b)with EBG structure.	60

Figure 4. 18	E-field intensity, a) without EBG, b) with EBG at 8.42 GHz.	61
Figure 4. 19	H- field intensity, a) without EBG, b) with EBG at 8.42 GHz.	62
Figure 4. 21	H-field intensity, (a) without EBG, (b) with EBG at 9.415 GHz.	63
Figure 4. 22	The radiation pattern compression between with and without EBG structure at 8.52 GHz, (a) directivity, (b) Gain.	64
Figure 4. 23	The radiation pattern compression between with and without EBG structure at 8.52 GHz, a) E-Field, b) H-Field.	65
Figure 4. 24	The radiation pattern compression between with and without EBG structure at 9.415 GHz, (a) directivity, (b) Gain.	66
Figure 4. 25	EBG structure at 9.415 GHz, (a) E-Field, (b) H-Field.	67
Figure 4. 26	The return loss and the coupling coefficient for the four coupling antennas S-parameters, (a) w/o EBG .(b) with EBG.	69
Figure 4. 27	E-field intensity, (a) without EBG, (b) with EBG at 8.89 GHz.	70
Figure 4. 28	H-field intensity, (a) without EBG, (b) with EBG at 8.89 GHz.	71
Figure 4. 29	The radiation pattern compression between with and without EBG structure at 9.415 GHz, a) E-Field, b) H-Field	72

LIST OF TABLES

	Page
Table 3. 1 S-shaped SRR dimensions (in mm).....	33
Table 3. 2 Structure dimensions for the EBG unit cell.....	38
Table 3. 3 Microstrip antenna structure dimensions.....	40
Table 3. 4 Four microstrip antennas structures dimensions.....	44
Table 4. 1 Comparison between 8.52GHz and 9.415GHz conventional and EBG's antenna	70
Table 4. 2 Comparison Between with and without EBG structure at 8.89 GHz for a conventional four array microstrip antenna.....	75

LIST OF ABBREVIATIONS

AMC	Artificial magnetic conductor
BW	Bandwidth
DE	Differential evolution
DNG	Double-negative
DPS	Double-positive ^[1] _{SEP}
EBG	Electromagnetic band gap ^[1] _{SEP}
EM	Electromagnetic ^[1] _{SEP}
ENG	Epsilon-negative ^[1] _{SEP}
FEM	Finite element method
FIT	Finite integration technique ^[1] _{SEP}
GA	Genetic algorithm ^[1] _{SEP}
GP	Ground plane ^[1] _{SEP}
GPS	Global positioning system ^[1] _{SEP}
LH	Left-handed ^[1] _{SEP}

MD- EBG	Metallo-dielectric electromagnetic band gap
MNG	Mue-negative ^{[1][1]} _[SEP]
MOM	Method-of-moment ^{[1][1]} _[SEP]
MWS	Microwave Studio ^{[1][1]} _[SEP]
PBC	Periodic boundary condition
PBG	Photonic band gap ^{[1][1]} _[SEP]
PEC	Perfect electric conductor ^{[1][1]} _[SEP]
PMC	Perfect magnetic conductor ^{[1][1]} _[SEP]
PML	Perfectly matched layer ^{[1][1]} _[SEP]
RH	Right-handed ^{[1][1]} _[SEP]
SNG	Single negative
SRR	Split ring resonator
TE	Transverse electric ^{[1][1]} _[SEP]
TM	Transverse magnetic ^{[1][1]} _[SEP]
VNA	Vector network analyzer
c	Light velocity in free space constant
d	Via diameter
f	Frequency ^{[1][1]} _[SEP]
f_c	Center frequency
f_r	Resonant frequency
h	Height or thickness ^{[1][1]} _[SEP]

\vec{k}	Wave vector
\hat{k}	Normalized wave vector
k	Propagation constant or wave number
k_0	Propagation constant or wave number in free space
n	Refractive index
n_{eff}	Effective refractive index
w	Unit cell parameter ^[SEP] ; weighting coefficient
$\mathbf{B}^{\text{[SEP]}}$	Magnetic flux density vector
C	Capacitance; crossover constant
$\mathbf{D}^{\text{[SEP]}}$	Electric flux density vector; translation vector
D	Period or lattice constant; directivity
$\mathbf{E}^{\text{[SEP]}}$	Electric field intensity vector
$E_{x, y, z}$	x-, y-, z-component of electric field vector
$E_{\tan}^{\text{[SEP]}}$	Tangential component of electric field vector
F	Fitness function, mutation scale factor
\mathbf{H}	Magnetic field intensity vector
$H_{x, y, z}$	x-, y-, z-component of magnetic field vector
H_{\tan}	Tangential component of magnetic field vector
L	Inductance
Γ	Center of the Brillouin zone
X, Y	Face of the Brillouin zone

M

Corner of the Brillouin zone



CHAPTER 1

INTRODUCTION

1.1 Historical Background

Metamaterials (MTMs) (“meta” means “beyond” in Greek) are the materials that not found in nature and designed by placing tiny resonant structures at regularly spaced distances to create the electromagnetic properties of a different bulk propagation medium [1].

The study of the fundamental theories about the true nature of electricity has been challenging scientists for centuries. Notwithstanding, the first empirical observations and written documents about electric physical phenomena have their origins in ancient Egypt, from about 3000 B.C.E., which referred to the study of electric shocks produced by Sh, who so called, as the Thunders of Nile (cited in Moler, 1991). These kind of phenomena have also fascinated and intended the studies made by the following civilizations (Greeks, Roman, Arabic, ...) [2]. Ancient writers, such as Pliny the Elder (23 C.E.) and Scribonius Larges (47 C.E.), observed that some materials, as they were rubbed against fur, attracted objects. Based on this observation, Thales of Miletus (600 B.C.E.) wrote some results about the nature of static electricity, where some amber objects, after being rubbed, rendered magnetic properties in contrast with other materials that needed no rubbing, such as magnetite [3]. Even though Thales was incorrect by believing that the nature of the attraction phenomenon was magnetic, later on science could prove that there was in fact a direct link between magnetism and electricity.

The recognition about a connection between the electric and magnetic phenomena was made by Andre-Marie Ampere and Hans Christian Oersted in the beginning of the XIX century [3]. This electromagnetic unification theory is first observed by Michael Faraday but extended by James Clerk Maxwell, and then partially reformulated by Oliver Heaviside and Heinrich Hertz, is one of the key accomplishments of XIX century mathematical physics. After Maxwell's publication

of his Treatise on Electricity and Magnetism (1873 C.E.)[4], electricity and magnetism were no longer two separate physical phenomena.

The equations obtained by Maxwell, along with the Lorentz force law (that was also derived by Maxwell under the name of Equation for Electromotive Force) fully describe classical electromagnetism. The equations show the existence of electro-magnetic waves, propagating in vacuum and in matter, which is of major scientific and engineering importance even nowadays [5]. As a consequence of the development of the comprehension of electromagnetism, many researchers have explored the interaction between electromagnetic fields and specific media. Artificial electromagnetic materials, with negative permeability and permittivity, have proven to have extraordinary electromagnetic properties. The study of these kind of artificial materials appears in the end of the XIX century, when Bose published his work on the rotation of the plane of polarization by man-made twisted structures in 1898 [5]. Lindman studied artificial chiral media formed by a collection of randomly oriented small wire helices in 1914 [6]. Afterwards, there were several other investigators in the first half of the XX century who studied various man-made materials. In the 1950s and 1960s, artificial dielectrics were explored by Kock, and its application for lightweight microwave antenna lenses. The 'bed of nails' wire grid medium was used in the early 1960s to simulate wave propagation in plasmas. The research on these kind of artificial materials increased as the development of various potential device and component applications appear [7].

The modern metamaterials started in the ends of 1960s, the grace for the modern developments is referred to three researchers papers by Victor Veselago in 1967 [8], Pendry in 2000 [9], and David Smith in 2000 [10], and researchers certainly are inspired by these papers in field of optical metamaterials.

A material with negative permittivity and/or permeability can be obtained using periodic structures. Electromagnetic wave propagation in such a media was observed in 1887 by Lord Rayleigh [11] first. The structure in his experiment with periodic repetition of dielectric layers with different permittivity was exactly a photonic crystal with 1D periodicity [12]. In 1968, V.G. Veselago described the basic properties of a material with simultaneously negative permittivity and permeability. He found out that a DNG media has a number of anomalous physical properties such as reversed Doppler shift, reversed Snell's law and reversed Cerenkov radiation [8]. Theoretical and experimental investigations of periodic structures were renewed in

1987 by E. Yablonovitch and S. John and the concept of a 2D and 3D photonic crystal was worked out [13], [14]. After many successes in optics, photonic crystals were implemented also in microwave and antenna engineering under the name of photonic band gap (PBG) that terminology was popularly used in the early studies, or electromagnetic band gap (EBG) structures [15].

EBG structures “*Generally speaking, electromagnetic band gap structures are defined as artificial periodic or sometimes non-periodic objects that prevent assist the propagation electromagnetic waves in a specified band of frequency for all incident angles and all polarization states*” [16].

Application of EBGs in antenna technology is very wide; for example superstrates for very narrow beamwidth and high gain [17], artificial magnetic conductors (AMC) for low-profile antenna design [18], special substrates with forbidden frequency band for surface wave propagation [19]. However, even if many analytical and approximate approaches were worked out, an exact design of EBGs is possible only by full-wave techniques. And due to the complexity of these structures, stochastic methods are mainly preferred. Nonetheless, their application in the field of EBGs as special substrates with suppressed electromagnetic wave propagation was explored only superficially up to now.

A paper published by Veselago in 1967 [8], gave the description for left-handed (LH) material, in which he assumed a homogeneous isotropic electromagnetic material in a certain frequency provide a negative real part values of the permittivity and permeability. Moreover, such medium supports a wave where the direction of the Poynting vector is in the opposite direction of its phase velocity direction, and thus exhibits a backward-wave propagation, which results a negative refractive index. This was until Smith inspired by the work of Pendry [9] constructed a composite medium in the microwave regime by arranging periodic arrays of small metallic wires and splitting resonators and demonstrated the anomalous refraction at the boundary of this medium, which is the result of negative refraction in this artificial medium.

The permittivity and/or permeability of these materials are in a certain frequency range smaller than zero. Depending on the negative value of the permittivity, permeability or both, metamaterials can be classified as epsilon-negative (ENG), mu-negative (MNG) or double-negative (DNG) identified as (LH) materials inside or negative index material (NIM) [10], which the electric field direction, magnetic field direction, and propagation direction satisfy a left-hand relation,

conventional materials have permittivity and also permeability larger than zero in all frequency ranges and they are called double-positive (DPS) which identified as Right-hand material (RHM).

Periodic structures have been studied for many years. At the end of 1980s, a 3D periodic structure, especially at microwave frequencies was operated, and followed by Yablonovitch *et al* realization [20], in which holes were applied into a block of dielectric material using mechanical drilling, leading to prevent any 3D propagation directions of the EM radiation, So that the material is transparent at these wavelengths in its solid form. Such artificially engineered periodic materials are generically known as electromagnetic bandgap (EBG) structures.

These new EBGs designs exhibit improved electromagnetic performance; one important category is wideband EBG design [21,22], compact EBG size is another goal for many EBG designs, which has attracted a broad attention from EBG researchers [23-29]

The strategy to acquire the negative permeability is to create exciting circular currents that can generate a strong magnetic resonance, while expected to produce the negative permittivity by virtue of the electric plasma response with added continuous wires. When negative refraction index is consistent with the negative permeability, consequently most of fishnet structure researches concentrated on characterizing and modeling their magnetic resonance [30-33].

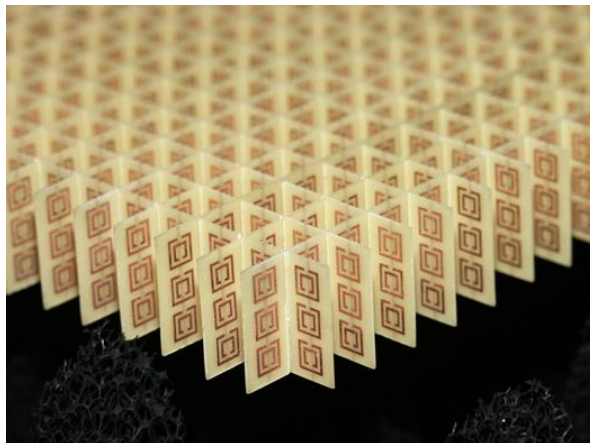


Figure 1. 1 Left-handed metamaterial at lens consisting of 3D an array arrangement with metamaterial unit cells. [34]

1.2 Motivation and Objectives

With the introduction of these new physical properties of EBG metamaterials, the study and interpretation of the associated results is in fact very attractive and challenging. There are many established physical concepts that must be reinterpreted in order to comply with this new paradigm and there is also the probability of finding new effects associated with this kind of materials, since there is a whole new set of resulting physical phenomena. In this dissertation, we have the possibility to associate and consolidate the more conventional and well-known electromagnetic concepts. With the introduction of the EBG metamaterials, in a more generalized perspective, we study the physical effects found even on simple guiding structures. As up to date the demonstrations and experiments of the new physical phenomena associated with (SNG) and (DNG) metamaterials have lead to the construction of new types of microwave structures whose applications to mobile communication systems have attracted a lot of attention from the scientific community. Such metamaterials could help improve the performance of several communication devices, such as antennas, absorbers and a lot of effort is being made on the design of antenna using this kind of periodic structures.

Typologically, after understanding the new physical phenomena that is associated with (SNG) and (DNG) media and the effects when applied to specific guid structures which have the ability to direct that process (MTMs properties) in X-Band frequency arena which will be the target of our study, the following designs achieve the aforementioned objectives:

1- A novel wideband metamaterial comprised of S-shaped SRR is proposed for X-band frequencies.

2- Two cases of Fishnet-Mushroom-like MTMs are studied. The first one is a wide band ENG, and the second one is a DNG MTMs. In both cases, the electromagnetic behaviour are represented in S-parameters numerically and experimentally studied. Basically, these kinds of structures are formed from the periodic configurations consisting of either an array of metallic patches or apertures which can be used in several MTM applications such as wireless communications, electromagnetic filtering, and so on.

1.3 Thesis organization

The dissertation consists of six chapters. The first chapter deals with the introduction and the literature review, in which a brief historical background analysis is included as well as key researchers and publications are chronologically documented. And also results are stated. Furthermore, the main motivations and objectives of this dissertation, as well as the explanation of the work's structure are represented.

In the second chapter we study the MTMs as periodic structures. First, the basic phenomena of electromagnetic wave propagation in metamaterials are briefly discussed. Second, the metallo-dielectric (MD) representation of DPS, ENG, MNG and DNG media is introduced. The implications of having a negative permittivity and permeability leads into studying the characterization of the medium and the physical phenomena such as the appearance of backward waves and the emergence and implications of negative refraction. Then, the propagation of surface waves on dielectric substrates and their suppression by periodic structures are described. Two basic structures split ring resonator (SRR) and EBG structure description that have been discussed and investigated in this work. Also briefly basic microstrip antenna design is presented.

The third chapter deals with the guided wave propagation with MTMs medium properties. We have chosen to study two new designed structures. First, S-Shaped Strip Ring Resonator (S-SRR) modal analysis is made, as an absorber. A mushroom-Like Fishnet EBG is the second structure is demonstrated, and the proposed EBG is utilized in mutual coupling of reduction array antennas.

The fourth chapter is dedicated to the study of the achieved results and the properties of the designed metamaterials. The designs applied on absorption and antennas structure dealing with such materials.

In the fifth chapter, main conclusions are exposed and some developing potential applications and further investigation hypothesis of the subjects addressed in this dissertation are introduced.

Finally, the future work is presented in the sixth chapter.

CHAPTER 2

METAMATERIAL

The advantage of the artificially designed MTM's is the presence of a gap (Stopband) in the frequency spectrum of propagating EM waves [13, 20,29,35]. This frequency bandgap depends on the permittivity of the dielectric inclusions or background used, the dimensions of the inclusions defects, their periodicity and the incidence angle of electromagnetic waves [36]. This feature leads to a variety of phenomena of both fundamental [37, 38] and practical [36, 39] interests in the way. In this chapter, the basic theory, numerical methods and applications of the EBGs will be reviewed.

2.1 Metamaterial theory

MTMs are a kind of a material with electromagnetic properties that define as artificial engineered electromagnetic structures with an effective permittivity and permeability, which are not readily available in nature. Metamaterial exhibits unusual characteristic behaviour like negative permittivity ($-\epsilon$) and negative permeability ($-\mu$) in certain frequency band, and exhibit reversal off Snell's Law (negative refractive index NRI) or (LHM). This relationship can be expressed by the refractive index formula $n = \pm\sqrt{\mu\epsilon}$.

Maxwell's equations describe the electromagnetic wave behaviours, which include both electric and magnetic studies. The magnetic and the electric fields as shown in Figure 2.1, propagate perpendicularly to each other. The fields directions in a plane wave also form right angles with respect to their direction of travel (the propagation direction). When an electromagnetic wave goes through the material medium, the fields of the waves interact with the electrons and other charges of the atoms and molecules that compose the material, causing them to move about Figure 2.2 shows that the wave traveling through two positive refractive index materials

from ($n_1 \rightarrow n_2$). The velocity of the wave decreases as the refractive index of the material increase.

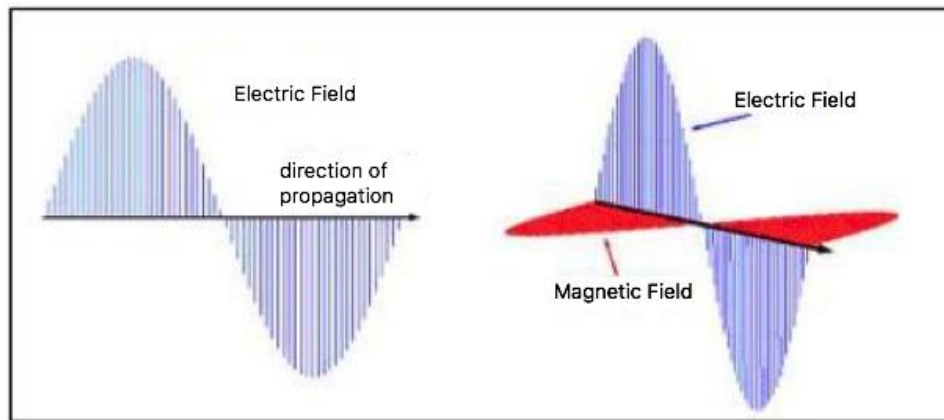


Figure 2. 1 Electric field propagation direction magnetic with direction of propagation. [40]

This interaction of the wave has an effect on speed or wavelength, recognizing the material can be represented by its permittivity and permeability they are unique properties that relevant in changing or tuning the wave behaviour, this values yields a higher degree of freedom in designing MTMs.

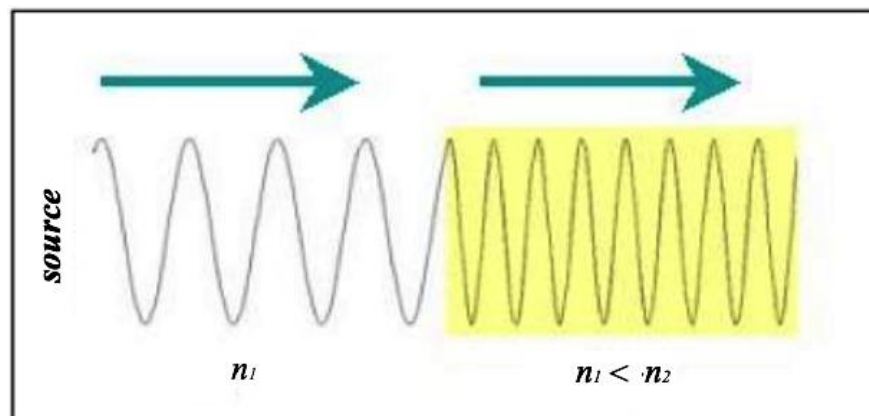


Figure 2. 2 Wave traveling in two different materials with $n_1, n_2 > 0$. [40]

As a result of NRI, the wave velocity is also negative, as shown in Figure 2.3. Thus, in LHM, wave propagates in the diametrical way of the energy currents.

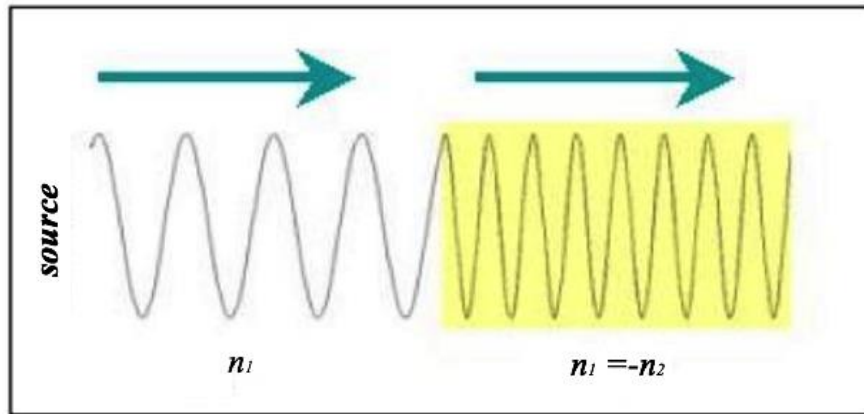


Figure 2. 3 Incident wave propagating in positive medium index to negative medium index material. [40]

2.1.2 Electromagnetic wave propagation in metamaterials

As mentioned already, metamaterials can be realized as periodic structures. A periodic structure in electrical engineering means medium, whose electromagnetic properties (permittivity, permeability, conductivity) change periodically in space. If the period D is much smaller than the wavelength λ of the propagating electromagnetic wave ($D \ll \lambda$), the periodic media can be considered as homogenous, and effective material properties of the periodic structure (effective permittivity ϵ_{eff} and effective permeability μ_{eff}) can be defined as follows [41]

$$\mathbf{D} = \epsilon_{eff} \epsilon_0 \mathbf{E}, \dots \dots \dots (2.1.a)$$

$$\mathbf{B} = \mu_{eff} \mu_0 \mathbf{H}, \dots \dots \dots (2.1.b)$$

where the electric flux density is presented by \mathbf{D} , the electric field intensity is \mathbf{E} , the magnetic flux density is \mathbf{B} and the magnetic field intensity is \mathbf{H} , ϵ_0 and μ_0 are the permittivity and permeability of free space, respectively.

The effective refractive index n_{eff} is related to both the effective permittivity and the effective permeability according to [42] Optimal design of artificial magnetic conductors including angular response [SEP]

$$n_{eff} = \pm \sqrt{\epsilon_{eff} \mu_{eff}} \dots\dots\dots(2.2)$$

The defined propagation constant k is using the effective refractive index [41], [42]

$$k = \frac{\omega}{c} n_{eff} \dots\dots\dots (2.3)$$

with ω being the angular frequency and c the light velocity in free space.

Based on Maxwell’s equations for plane wave propagation in isotropic media, the following relationship between the vectors of electric and magnetic field intensity can be written [41]

$$\hat{\mathbf{k}} \times \mathbf{E} = \sqrt{\frac{\mu_{eff} \mu_0}{\epsilon_{eff} \epsilon_0}} \mathbf{H}, \dots\dots\dots (2.4.a)$$

$$\hat{\mathbf{k}} \times \mathbf{H} = -\sqrt{\frac{\epsilon_{eff} \epsilon_0}{\mu_{eff} \mu_0}} \mathbf{E}, \dots\dots\dots (2.4.b)$$

where $\hat{\mathbf{k}}$ is the normalized wave vector ($\hat{\mathbf{k}} = \frac{\mathbf{k}}{|\mathbf{k}|}$, $k = |\mathbf{k}|$). For ϵ_{eff} and μ_{eff} positive, the effective refractive index n_{eff} in (2.2) is real and positive as well as the propagation constant k in (2.3). The wave vector \mathbf{k} and the Poynting vector $\mathbf{p} = \mathbf{E} \times \mathbf{H}$ have the same orientation (“forward wave”). For this case, \mathbf{E} , \mathbf{H} and \mathbf{k} form a right-handed rectangular system as depicted in Figure 2.4a. Due to that, DPS materials are called “right-handed” (RH).

If ϵ_{eff} or μ_{eff} is negative (i.e. the material is the type of ENG or MNG, respectively), the effective refractive index n_{eff} is imaginary as well as the propagation constant k . Electromagnetic waves in such a media are strongly attenuated. If both ϵ_{eff} and μ_{eff} are negative, the effective refractive index n_{eff} and the wave vector k are real, however with the negative sign [42]. The wave vector \mathbf{k} and the Poynting vector \mathbf{p} have opposite orientation (“backward wave”). Vectors \mathbf{E} , \mathbf{H} and \mathbf{k} form a left-handed rectangular system as depicted in Figure 2.4b, DNG materials are “left-handed” (LH).

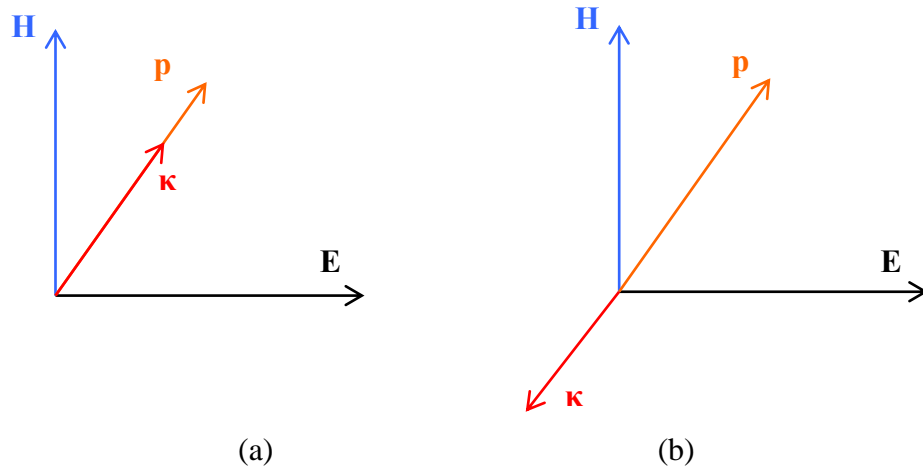


Figure 2.4 (a) Right-handed material, (b) Left-handed material.

Now, let us consider the interface of two media. The continuity of the tangential electric and magnetic field components $E_{1,tan}, E_{2,tan}, H_{1,tan}, H_{2,tan}$ at that interface can be expressed as [43]

$$-\frac{1}{j\omega\mu_1} \left. \frac{\partial E_{1,tan}}{\partial n} \right|_{Interface} = -\frac{1}{j\omega\mu_2} \left. \frac{\partial E_{2,tan}}{\partial n} \right|_{Interface}, \dots \dots \dots (2.5.a)$$

$$-\frac{1}{j\omega\varepsilon_1} \left. \frac{\partial H_{1,tan}}{\partial n} \right|_{Interface} = -\frac{1}{j\omega\varepsilon_2} \left. \frac{\partial H_{2,tan}}{\partial n} \right|_{Interface}, \dots \dots \dots (2.5.b)$$

In (2.5.a) and (2.5.b), $\partial/\partial n$ represents the normal derivative and $\varepsilon_i, \mu_i, i = 1, 2$, are the permittivity and permeability in these two media, respectively. For $\varepsilon_1, \varepsilon_2$ and/or μ_1, μ_2 with opposite signs, the normal derivatives of the tangential fields on both sides of the interface will have opposite signs. It means a discontinuity at the boundary of the two media, which may imply a concentrated resonant phenomenon at that interface, which is similar to the current and voltage distribution at the junction between an inductor and a capacitor at the resonance of an L-C circuit. The mechanism behind this “interface resonance” can be described in several ways.

2.1.3 Metallo-dielectric representation of metamaterials

Realization of metamaterials as periodic metallo-dielectric (MD) structures was intensively studied in the last decade. Nowadays, the easy in fabrication and adjustable with variety of microwave circuits made the (MD) metamaterials became the most widely used types of electromagnetic band gap structures in microwave and antenna techniques.

The general circuit representation of a (MD) unit cell is shown in Figure 2.5, If $D \ll \lambda$, the effective permittivity and permeability of the periodic media can be expressed by using the series impedance Z and shunt admittance Y of the unit cell as [44]

$$\epsilon_{eff} \epsilon_o = \frac{Y}{j \omega D}, \dots\dots\dots (2.8.a)$$

$$\mu_{eff} \mu_o = \frac{Z}{j \omega D}, \dots\dots\dots (2.8.b)$$

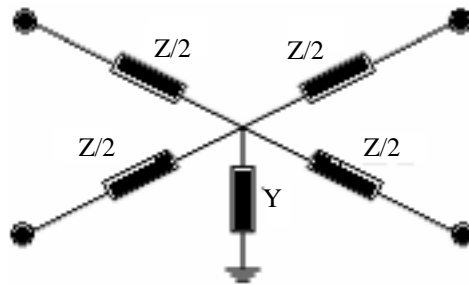
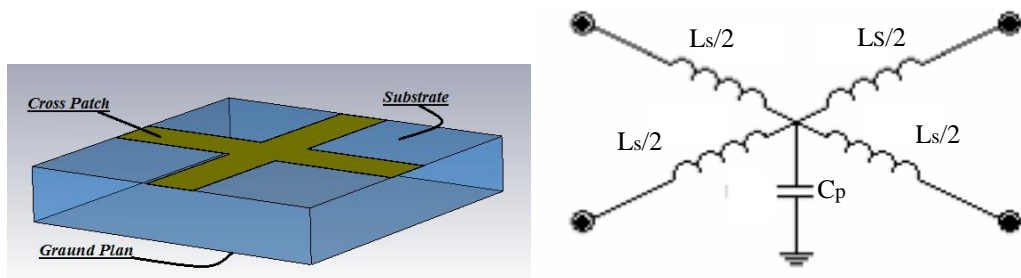


Figure 2.5 The general circuit representation of a (MD) unit cell.

Depending on the L and C elements as the series and shunt components arrangements of the unit cell, we can obtain four types of materials (DPS, ENG, MNG and DNG) as depicted in Figure 2.6. (square unit cells are assumed for simplicity).



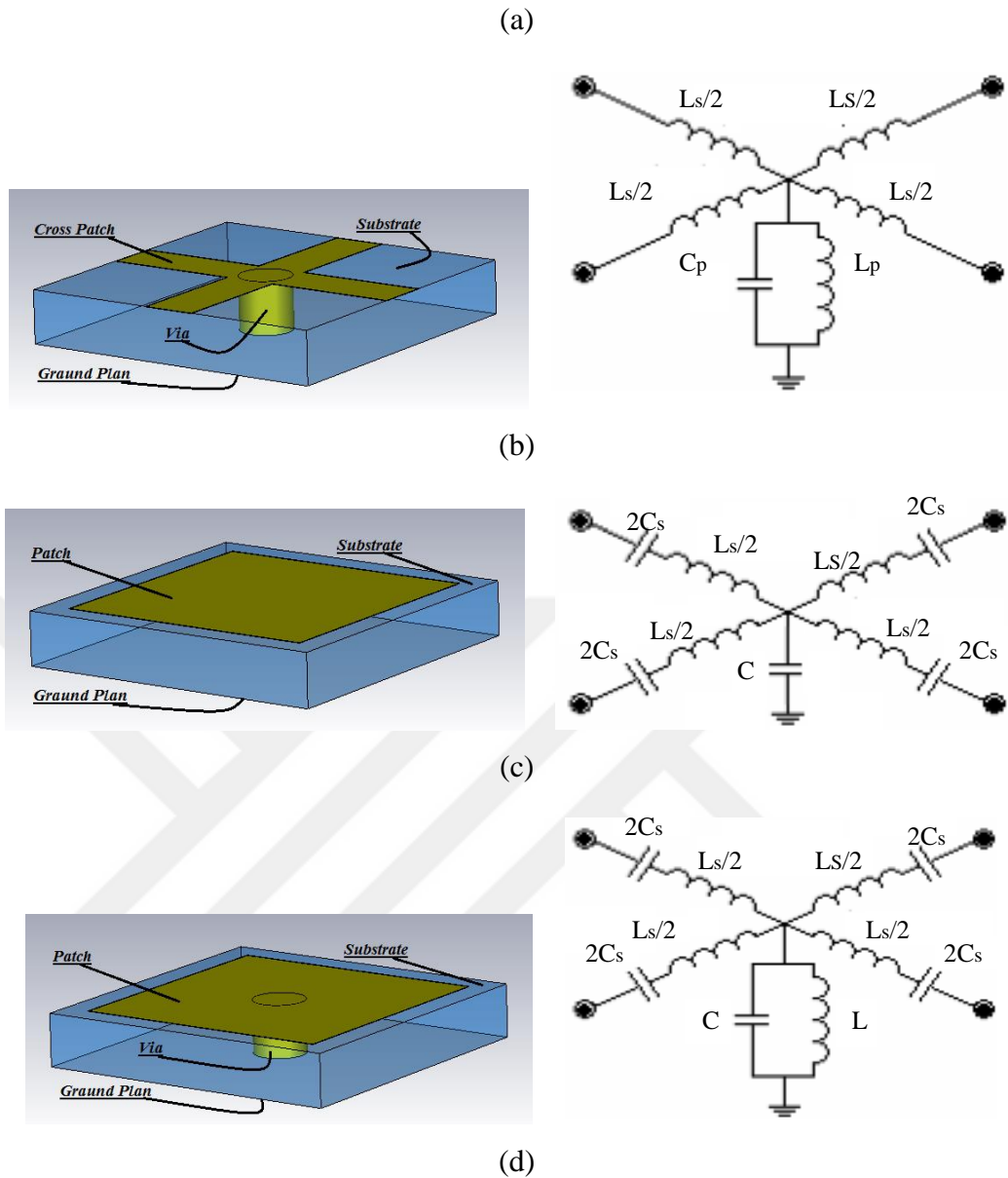


Figure 2. 6 The basic unit cell realizations of metallo-dielectric periodic structures as (a) DPS, (b) ENG, (c) MNG, (d) DNG.

A DPS material can be implemented as a 2D mesh of microstrip lines (a series inductance and a shunt capacitance to the ground plane), Figure 2.6.a. For ENG behavior, a shunt inductance is needed in addition to a series inductance and a shunt capacitance, Figure 2.6.b. A metallic patch on a dielectric substrate in Figure 2.5.c represents a series inductance and a series capacitance to neighboring cells and a shunt capacitance to the ground plane – its behavior corresponds to MNG. A metallic patch on a dielectric substrate with a shorting via Figure 2.6.d, acts as a DNG material due

to the series inductance and the capacitance to neighboring cells, and the shunt inductance and the capacitance to the ground plane.

Based on the circuit representation of four types of materials, only the DNG can generate backward waves and thus behaves as LH media. However, the circuit model of materials is valid only if the period is much shorter than the wavelength. In fact, all the periodic structures generate backward waves if the lattice constant becomes approximately half of the wavelength (Bragg's condition).

2.2 Metamaterial Classification

The reaction of a system to the presence of electromagnetic field can be defined by the properties of the materials used. By using permittivity and permeability the MTMs can be classified in four medium categories as follows of the medium illustrated as in Figure 2.7. At the intersection (point 0) it is the zero refractive index diagrams.

- I. A DPS medium is obtained when the homogenous medium provide simultaneously permittivity and permeability more than null ($\epsilon > 0, \mu > 0$). Most natural media (e.g. Dielectrics) fall within this category.
- II. An ENG medium is obtained with permittivity less than zero & permeability more than null ($\epsilon < 0, \mu > 0$). Many electric types of plasma exhibit these features.
- III. A DNG medium is obtained when the homogenous medium provide simultaneously permittivity & permeability less than null ($\epsilon < 0, \mu < 0$). Only artificial structures are in this category because there is no such material that behave and exist in nature.
- IV. A MNG medium is obtained with permittivity is more than zero & permeability less than zero ($\epsilon > 0, \mu < 0$). Many magnetic types of plasma exhibit these features.

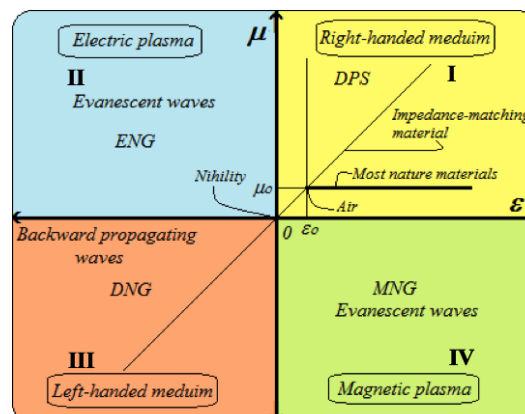


Figure 2.7 The material classifications depending on the Permittivity-permeability (ϵ - μ) real value. [45]

2.3 Snell's Law and Negative Refraction

As in the previous section, the phase velocity of the wave in a DNG media is negative and this has important implications. Let us consider the scattering of a wave that is incident on a DPS-DNG interface as shown in Figure 2.8.

We Assume that we have a DNG medium, with a negative refraction index ($n_2 < 0$) in the area with green background ($x < 0$ and $z > 0$) and a DPS media, with a positive refraction index ($n_2 > 0$, in $x > 0$ and $z > 0$). We also assume that the losses on both the DPS and the DNG materials can be neglected.

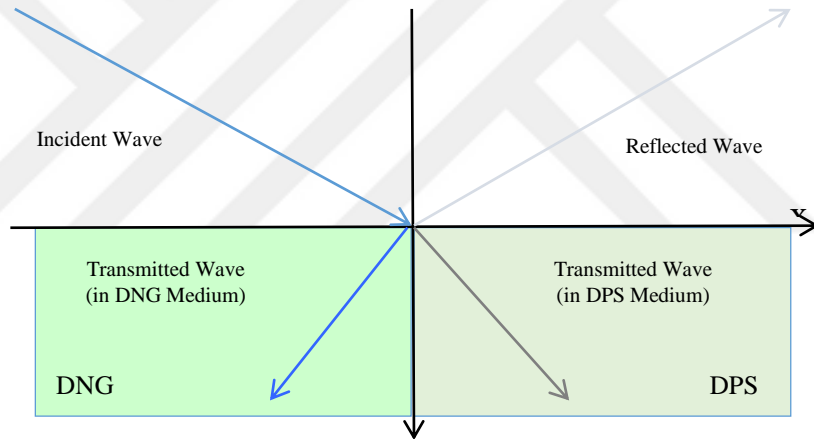


Figure 2.8 Propagation of a wave that incident on a DPS-DNG interface.[46]

The Snell's law of reflection assures us that the angle of reflection is equal to the angle of incidence:

$$\theta_r = \theta_i \dots \dots \dots (2.9)$$

We can also obtain, from the Snell's law of refraction, the relation between the angle of the transmitted wave and the angle of the incident wave [47], which is given by:

$$n_1 \sin \theta_i = n_2 \sin \theta_t \dots \dots \dots (2.10)$$

For a DNG material with a NRI n_2 we see that, to obtain the correct angle of the transmitted wave one must write (2.10) in the following form:

$$\theta_t = \text{sgn}(n_2) \arcsin \left[\frac{n_1}{|n_2|} \sin(\theta_i) \right], \dots \dots \dots (2.11)$$

Note that if the refraction index of a medium is negative, according the *Snell's Law*, the refracted angle should also become negative and then, as we have seen in the previous section, the direction of the energy flux, given by \mathbf{S} , is the opposite of the wave propagation, given by \mathbf{k} . Moreover,

Considering this, we can define a complex refractive index as :

$$n = n' + in'' \dots \dots \dots (2.12)$$

where $n' = \Re(n)$ and $n'' = \Im(n)$.

It's also important to notice that we are considering the solution where $n'' > 0$, as we have mentioned in the previous section, because we are dealing with a passive media, where n'' is called the extinction coefficient. On the other hand, if we have chosen to use $n'' < 0$ [SEP] refracted angle but a positive one instead, which is the same result as if the transmitted wave was propagating in a DPS material, with one very important difference, as we have mentioned before, that the energy flux was then propagating in the direction of the interface (and the source) which is the opposite of a causal direction and makes no sense for a passive media.

In addition, Figures 2.9 and 2.10 show the scattering patterns of the waves on entering and exiting the conventional and LHM material respectively. For conventional material, the refracted waves are spreading away after getting in and exiting the medium. For LHM, the waves are refracted in such a manner as to develop a focus within the material and then another just outside.

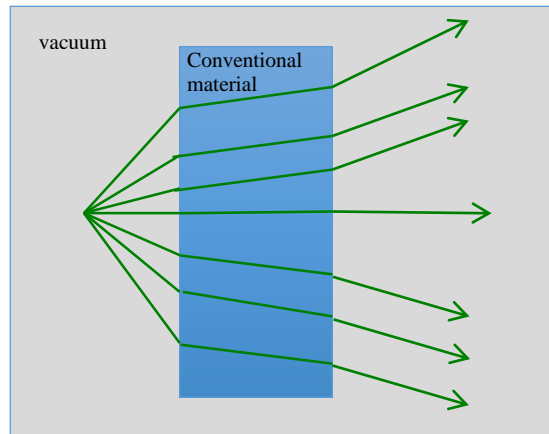


Figure 2. 9 Conventional material rays refraction.

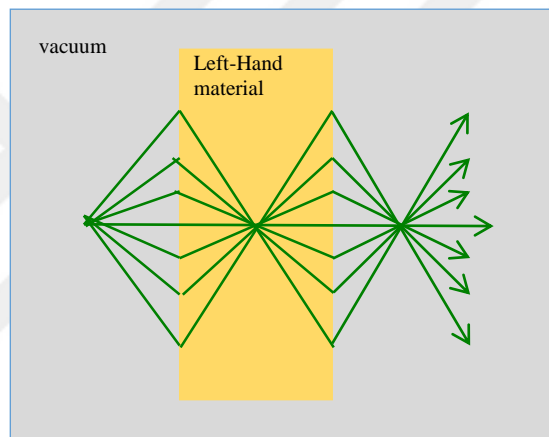


Figure 2. 10 Left-handed material rays refraction.

2.4 Dispersion Diagram

Symmetry in an electromagnetic structure or system is important in the analysis of wave behaviour. Most theoretical studies on EBGs are based on an interesting symmetry property as the EBGs show periodicity in the dielectric of the material. As a consequence, a dispersion diagram can be derived to describe the frequency behaviour of EBGs.

2.4.1 Brillouin Zone

A key fact about Bloch's states is that a Bloch state with wave vector \mathbf{k}_y and a Bloch state with wave vector $\mathbf{k}_y + m\mathbf{b}$ are identical, where $\mathbf{b} = 2\pi/a$ and m is an integer. That means the mode frequencies are also periodic in \mathbf{k}_y : $\omega(\mathbf{k}_y) = \omega(\mathbf{k}_y + m\mathbf{b})$. So we only need to consider \mathbf{k}_y to exist in the range $-\frac{\pi}{a} < k_y \leq \frac{\pi}{2}$. This region of important, no redundant values of \mathbf{k}_y is called the Brillouin zone.

For example as shown in consider square elements periodically laid in a square lattice Figure 2.11.a. And the Brillouin zone of the lattice plotted in Figure 2.11.b. This structure shows not only discrete translational symmetries along the x and y directions, but also rotation, mirror-reflection and inversion symmetry.

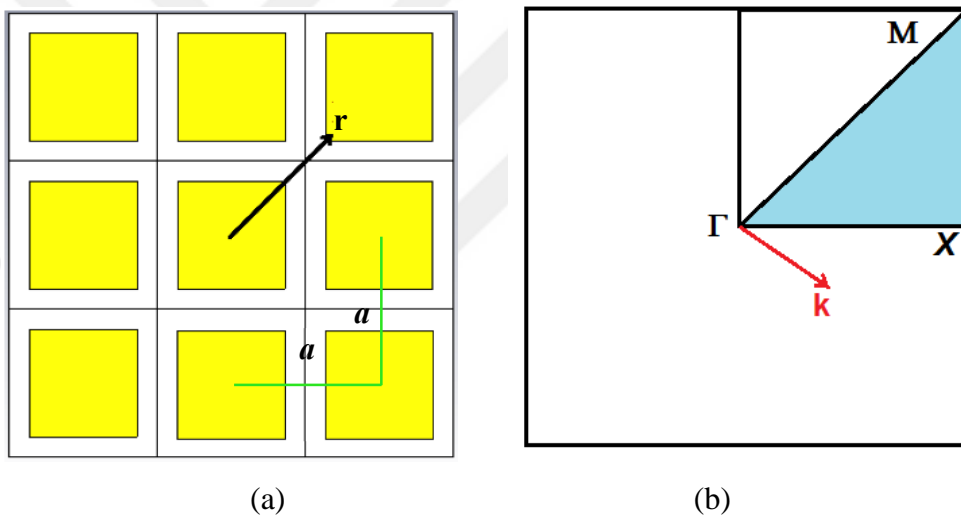


Figure 2.11 (a) The physical lattice of an EBG made using a square lattice. An arbitrary vector \mathbf{r} is shown. (b) The Brillouin zone of the reciprocal lattice, centered at the origin (Γ). An arbitrary wave vector \mathbf{k} is shown. The irreducible Brillouin zone is the light blue triangular edge. The special points at the center corner and face are conventionally known as Γ , M and X . [48]

It is shown [48] that when these symmetries are shown in physical space, the reciprocal space (\mathbf{k} space) shows the same kinds of symmetry. As a result, in the Brillouin zone shown in Figure 2.11.b, every \mathbf{k} -point included in it needs not to be considered, but only the \mathbf{k} vector symmetry within the region Brillouin zone blue

triangle need to be considered. That smallest region is termed as the irreducible Brillouin zone, shown in light blue color; the rest of the Brillouin zone contains redundant copies of the irreducible zone.

2.4.2 Dispersion Diagram and Photonic Band Gap

With the knowledge of the irreducible Brillouin zone, the possible modes versus the wave vector \mathbf{k} can be plotted. This curve can be plotted in one dimension, two dimensions or three dimensions. These plots provide the dispersion relation and information on the flow of energy in an intuitive way. Figure 2.12, shows two examples of one-dimensional diagrams of one-dimensional EBG materials.

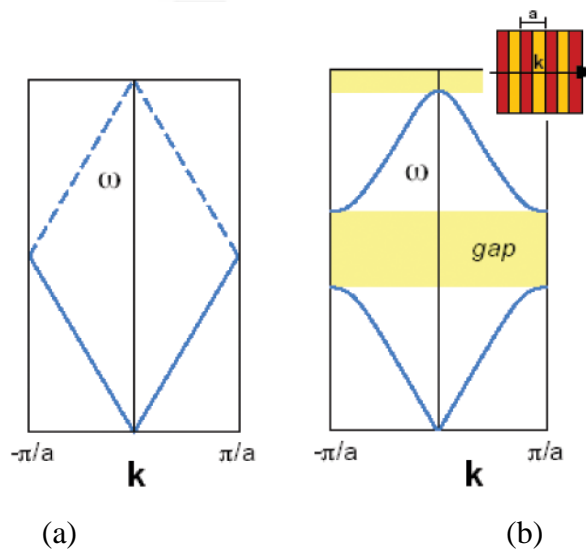


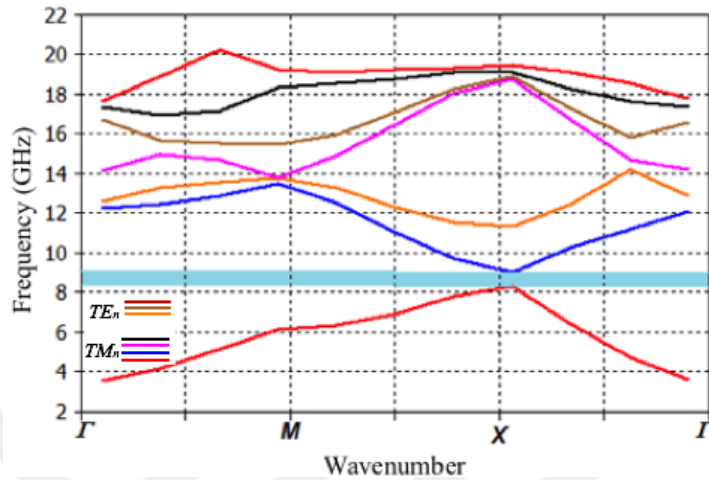
Figure 2. 12 (a) Dispersion relation (band diagram), (b) Bandgap has been opened. [49]

Figure 2.12.a, is the dispersion diagram for a uniform dielectric medium, to which a periodicity of a has been artificially assigned. It is known that in a uniform medium, the speed of light is reduced by the index of refraction. So the plot is just the light-line given by

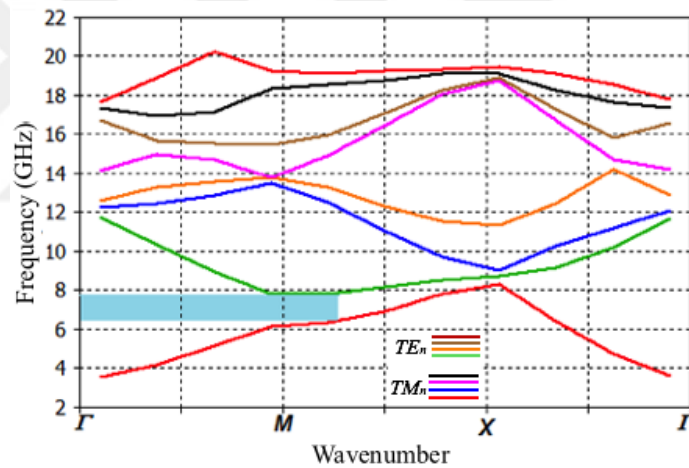
$$\omega(k) = \frac{ck}{\sqrt{\epsilon}} \dots\dots\dots (2.13)$$

Because the wavevector \mathbf{k} repeats itself outside the Brillouin zone, the lines fold back into the zone when they reach the edges. The dashed lines show the folding effect of applying Bloch's theorem with an artificial periodicity a .

In Figure 2.13.a, b, there is a gap in frequency between the upper and lower branches of the lines - a frequency gap in which no mode, regardless of \mathbf{k} can propagate through the structure. This gap is called an electromagnetic band gap, which can be further classified as:



(a)



(b)

Figure 2. 13 (a) A two-dimensional dispersion diagram for a two-dimensional EBGs [illustrated in Figure. (2.12)], in which a complete bandgap is shown by the light blue color; (b) A two-dimensional dispersion diagram where an incomplete bandgap can be found.

a. Complete Electromagnetic Bandgap: the range of ω in which there are absence for any electromagnetic modes and no propagating (real \mathbf{k}) solutions of Maxwell's equations for any \mathbf{k} , the first mode starts at zero and the eigen mode-frequency increases the wave number. When it reached a turning point at 8.2GHz, it decreases as the wave number increased, it is noticed that the field for the first mode is TM_0 dominant. The second mode starts to appear at frequency higher than 9 GHz, it is clear

that no eigen-mode exists in the frequency range from 8.2GHz to 9 GHz. Thus, this frequency region is defined as a surface wave bandgap; no surface waves can propagate in the EBG structure inside this frequency bandgap.

b. Incomplete Electromagnetic Bandgap: This bandgap only exists over a subset of all possible wavevectors, polarizations, and/or symmetries.

2.5 Metallo-Dielectric Structures

There are two basic structures that have been discussed and investigated in this work is SRR and EBG respectively.

2.5.1 SRR MTMs

A SRR is a component part of a negative index MTM's (NIM), also known as double negative MTMs (DNG). They are also component parts of other types of MTMs such as Single Negative MTMs (SNG). SRRs are also used for research in terahertz MTM's, acoustic MTMs, and MTMs antennas. SRRs are a pair of concentric annular rings with splits in them at opposite ends. The rings are made of nonmagnetic metal like copper and have small gap between them. There are varieties of SRR structures have been reported in literatures like square, circular, triangular, omega, and labyrinth resonator, some of these structures is shown in Figure 2.14.

The SRR can be excited by a magnetic field, which directed along its axis to exhibits a large magnetic dipole moment depending on the symmetry of the SRR; the SRR also exhibits an electric response that can be orientation of respect to the electric component of the field. Thus, while the SRR medium can be considered as having a predominantly magnetic response for certain orientations with respect to the incident wave, it is generally the case that the SRR exhibits magneto electric coupling, and hence a medium of SRRs arranged so as to break mirror symmetry about one of the axes will exhibit bianisotropy.



Figure 2. 14 Different geometries for modified SRR. [50]

2.5.2 Electromagnetic Bandgap MTMs

Metamaterials are based on periodic or non-periodic artificial engineered structures that exhibit unusual characteristic behaviors like negative permeability and negative permittivity, simultaneously over a common resonance frequency band. EBG based on frequency selective surfaces (FSS) is one type of MTM's with electrical properties. Application of truncated FSS appears as EBG technique. FSS based MTM's have become an alternative to the fixed frequency MTMs.

In current years, there have many researches that have made growing interest on EBG structures. In solid-state physics and related applied fields, a band gap, also called an energy gap or band gap, is an energy range in a solid where no electron states exist, due to their ability to influence the propagation of electromagnetic waves.

The unique structure of EBG, which have led to provide electromagnetic properties for wide range of applications, depending on the exhibited electromagnetic properties, names have been achieved in the literature, including: DNG materials, LH materials, NRI materials, magneto-dielectric materials with artificially controlled high permeability, Soft and hard surfaces that stop or support the propagation of waves, high impedance surfaces with relatively large surface impedances for both TE and TM waves, magnetic conductor. Figure 2.15 shows two EBG structures in antenna designs.

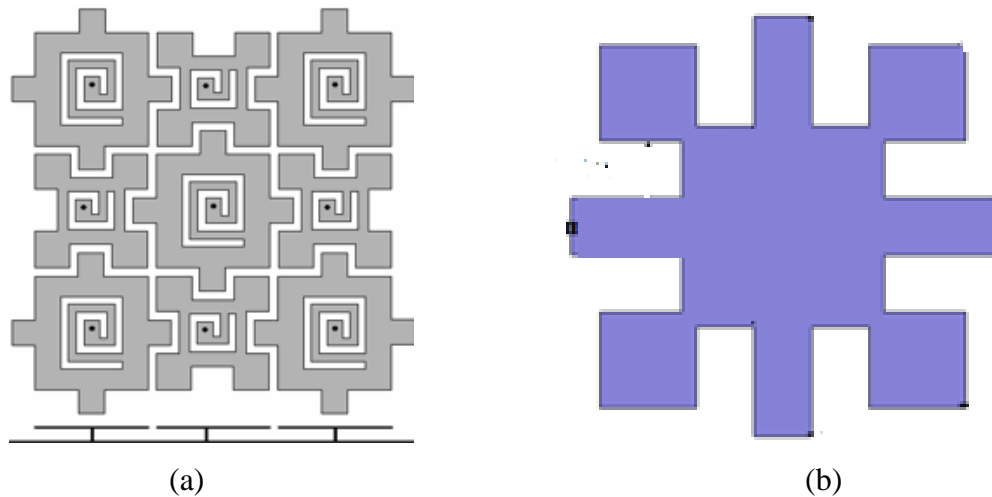


Figure 2.15 Different EBGs geometry: (a) rabbet spiral EBG structure [51],
(b) uniplanar EBG[52]

Control the electromagnetic wave propagation direction through the ground plane instead of radiation into free space is taken in account, as known, the surface

waves decreases the antenna gain and efficiency. The back lobe radiations is increased with the diffraction of surface waves existing, which it causes the signal to noise ratio in wireless communication systems deterioration such as Global Positioning System (GPS) receivers. EBG structures produce a band gap feature has found useful applications in suppressing the surface waves in deferent antenna designs. An example for previous, the effective design to increase gain and power pattern, an EBG structure is used to surround a microstrip antenna [53].

One of objectives in modern wireless communication systems the prevalent of EBG application that design antennas with a low profile provide good radiation efficiency. The electric current that is directed in a vertical to a Perfectly Electric Conducting (PEC) ground plane, can exhibit an image current with same direction and reinforces the radiation from the original current. In result, an antenna with good radiation efficiency has obtained, but, on the other hand, the antenna suffers a high profile due to the vertical placement of the current.

2.6 Surface waves

Dimensions of a microwave device can be significantly reduced by placing the planar layout on high-permittivity dielectrics. If the device is a patch antenna, the increase of the permittivity of the substrate causes the decrease of its operational bandwidth. A thicker dielectric slab is a potential solution to eliminate the negative effect of the increasing substrate permittivity on the antenna bandwidth. By increasing permittivity and height of dielectrics, the impact of surface wave propagation on antenna performance becomes more crucial.

Surface waves are electromagnetic waves trapped on the interface of two dissimilar materials (metal-dielectrics or dielectrics-dielectrics). In Figure 2.16, the propagation of surface waves within a grounded dielectric slab is depicted. A wave impinging at the dielectric-air interface undergoes complete internal reflection for incident angles greater than the critical angle θ_c given by the expression [54]

$$\theta_c = \sin^{-1} \left(\frac{1}{\sqrt{\epsilon_r}} \right) \dots\dots\dots (2.14)$$

where ϵ_r is the relative permittivity of the dielectrics. In fact, if the radiation source is a planar elementary dipole, the ratio of the power radiated into the substrate to the

power radiated into the air is approximately $1/\sqrt{\epsilon_r^3}$ [54]. Diffraction of surface waves at the boundaries of the antenna substrate causes the deformation of the radiation pattern and a worse front-to-back ratio.

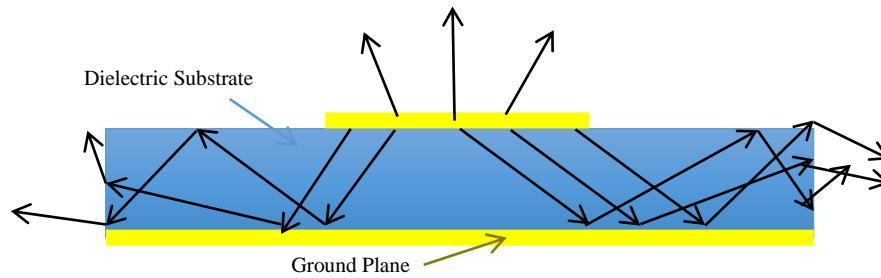


Figure 2. 16 Surface wave propagation inside the grounded dielectric slab.

The TM and TE surface wave propagation can be investigated on a general impedance surface whose properties can be described with a single parameter the surface impedance Z_s [55], [56]. The surface is positioned in the y - z plane. A surface wave propagates in the $+z$ direction with the fields drop exponentially with constant α decrease in the $+x$ direction as shown in Figure 2.17.

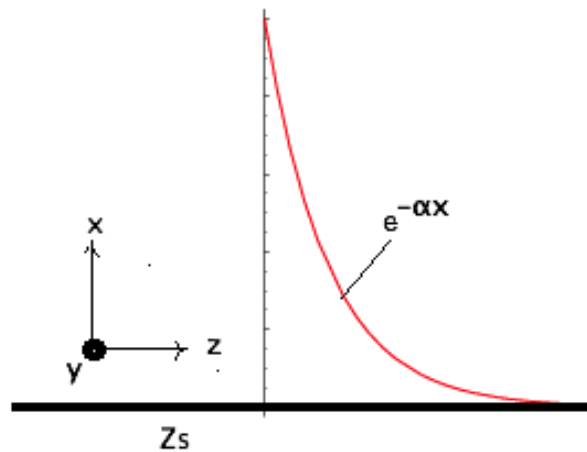


Figure 2. 17 Surface wave on an impedance surface.

For TM polarized surface waves, the x and z components of the magnetic field intensity and the y component of the electric field intensity are equal to zero, $H_x = H_z = E_y = 0$. The z component of the electric field intensity E_z can be expressed as

$$E_z = C e^{-jkz-x}, \dots\dots\dots (2.15)$$

where C is a constant and k is the propagation constant in the z direction. Recalling Ampère's law

$$\nabla \times H = \varepsilon \frac{\partial E}{\partial t} \dots\dots\dots (2.16)$$

And keeping in mind that only the y component of the magnetic field intensity is non-zero, equation (2.16) can be rewritten in the following form –

$$\frac{\partial H_y}{\partial x} = j\omega\varepsilon E_z \dots\dots\dots (2.17)$$

Combining (2.15) with (2.17) and evaluating the integral

$$H_y = j\omega\varepsilon \left(-\frac{1}{\alpha}\right) E_z \dots\dots\dots (2.18)$$

$$Z_s(TM) = \frac{E_z}{H_y} = -\frac{\alpha}{j\omega\varepsilon} = \frac{j\alpha}{\omega\varepsilon} \dots\dots\dots (2.19)$$

The surface impedance Z_s is the electric field over the magnetic field at the surface ratio [55, 56]. In accordance with (2.19), TM waves can only occur as a positive (i.e. inductive) reactance on surfaces, and so on, the permittivity of the medium must be positive also.

In the case of the TE waves, the z component of the magnetic field intensity H_z expressed as:

$$H_z = C e^{-jkz-ax} \dots\dots\dots (2.20)$$

Considering Faraday's law

$$\nabla \times E = -\mu \frac{\partial H}{\partial t} \dots\dots\dots (2.21)$$

The surface impedance for TE waves can be derived [10], [12]

$$Z_s(TE) = -\frac{E_y}{H_z} = -\frac{j\omega\varepsilon}{\alpha}, \dots \dots \dots (2.22)$$

Taking (2.22) into account, TE waves obviously require the negative (i.e. capacitive) impedance on surface, and thus, the permeability of the medium must be positive also.

The dispersion relation of *TM* and *TE* surface waves on a grounded dielectric slab (GDS) with the relative permittivity ε_r and the height h can be obtained by evaluating ξ (normalized wave impedance) in (2.23) and substituting into (2.24) [55, 56]. Parameter $k_0 = \omega/c$ is the free space wave number.

We can write for even TM modes (TM_0, TM_2, \dots)

$$\frac{1}{\varepsilon_r} \xi \tan(\xi) - \sqrt{(\varepsilon_r - 1) (k_0 h)^2 - \xi^2} = 0, \dots \dots \dots (2.23.a)$$

For even TE modes (TE_2, TE_4, \dots)

$$\frac{1}{\varepsilon_r} \xi \cot(\xi) - \sqrt{(\varepsilon_r - 1) (k_0 h)^2 - \xi^2} = 0, \dots \dots \dots (2.23.b)$$

And for odd TE modes (TE_1, TE_3, \dots)

$$\xi \cot(\xi) - \sqrt{(\varepsilon_r - 1) (k_0 h)^2 - \xi^2} = 0, \dots \dots \dots (2.23.c)$$

For odd TM modes (TM_1, TM_3, \dots)

$$\xi \tan(\xi) - \sqrt{(\varepsilon_r - 1) (k_0 h)^2 - \xi^2} = 0, \dots \dots \dots (2.23.d)$$

Then the wave number k can be calculated using

$$k = \sqrt{k_0^2 \varepsilon_r - \left(\frac{\xi}{h}\right)^2}, \dots \dots \dots (2.24)$$

A typical surface wave dispersion diagram of a MTM structure is depicted in Figure 2.13.a. Clearly, the dominant TM_0 wave has no cutoff and propagates from zero

frequency (the surface impedance is inductive). At the frequency for which the dielectric slab thickness equals approximately $\lambda/4$, the surface impedance becomes capacitive and the first TE wave occurs. However, the TM wave is still propagating; the wave simply adjusts its position toward the ground plane and the apparent surface impedance remains inductive [55, 56]. In consequence, there is no band gap between the surface waves on a grounded dielectric slab without any periodic loading.

As discussed above, surface waves can be successfully suppressed using a periodic structure that exhibits the negative permittivity (TM wave suppression) or the negative permeability (TE wave suppression) in a certain frequency band.

2.7 Microstrip Antenna Design

A conventional scheme of microstrip antenna with rectangular patch shape is shown in Figure 2.18 [57].

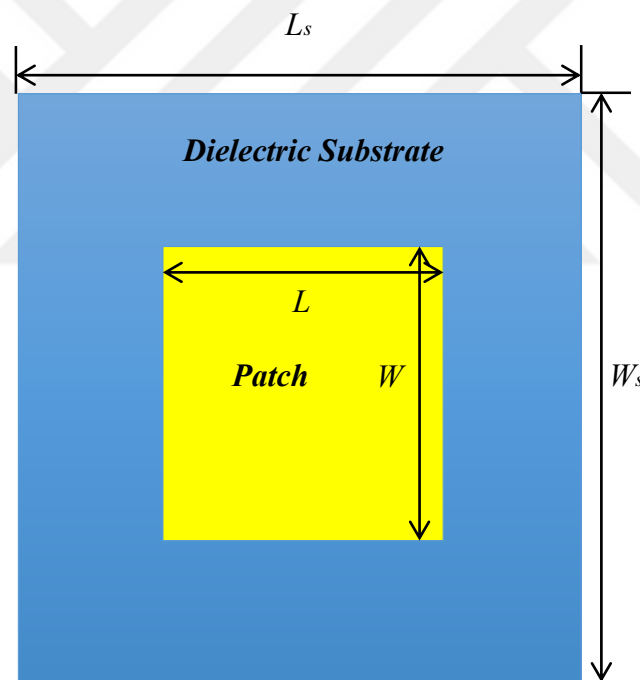


Figure 2. 18 Microstrip schematic (Top view).

The realizations for the conventional patch antenna equations are shown as below: [57, 58]

$$W = \frac{c}{2f_r} \left(\frac{\epsilon_r + 1}{2} \right)^{-\frac{1}{2}} \dots\dots\dots(2-25)$$

where the patch antenna width is presented by W , and the operational frequency by f_r and the substrate permittivity by ϵ_r .

Additionally, note that the EM fields are propagate outside of the patch as well but they are not contained entirely within the microstrip patch. This phenomena result to fringing effect. A capacitor will be formed with the two parallel plates of microstrip and ground; the electric field does not end willingly with end of plate's edge. There is some field outside those plates that curves from one to the other, leads to changing as will the fringing effect, the effective length and the effective permittivity.

$$L = \frac{c}{2f_r\sqrt{\epsilon_{eff}}} - 2\Delta l \dots \dots \dots (2-26)$$

where the patch antenna length is presented by L and c (3×10^8 m/s) is speed of EM wave in vacuum.

$$\Delta l = 0.412h \left(\frac{\epsilon_{eff} + 0.3}{\epsilon_{eff} - 0.258} \right) \left(\frac{\frac{w}{h} + 0.264}{\frac{w}{h} + 0.8} \right) \dots \dots \dots (2-27)$$

Using the Equations (28) and (29), the substrate length and width dimensions can be found:

$$W_s = W + 6h \dots \dots \dots (2-28)$$

$$L_s = L + 6h \dots \dots \dots (2-29)$$

where the substrate width represented by W_s is and the substrate length represented L_s is and h is substrate thickness. [57, 58]

2.8 Microstrip Antenna Array and Mutual Coupling Reduction

The EBG structure is applied to antenna array which consists of the multiple stationary antenna elements, because the multiplicity of elements allows improved performance such as gain and directivity enhancement. However, low impedance bandwidth and excitation of surface waves are the major disadvantages of antenna array. Excitation of surface waves increases the mutual coupling between antenna elements. Because the presence of mutual coupling severely degrades the performance of array such as blind angles, side lobes in almost all type of antenna arrays.

Recent years, many EBG structures have been examined and studied extensively [59-71]. Over the decades, mutual coupling is one of the most common problems in the application of antenna arrays. The mutual coupling reduction or isolation between closely packed antenna elements is the current demand in the advancement of the multiple input multiple output (MIMO) wireless communication systems [68].

2.9 Boundary Conditions

An ideal EBG structure that has infinite periodicity does not exist in the real world. Any EBG structure used in the real world is with boundaries. However, it is always in interest and beneficial to study infinite EBGs before the application of its finite sized dual. Periodic boundary condition (PBC) is the tool that enables the computation of an infinite EBG through a limited computational domain. So EBGs, which are infinite in one-dimension, two-dimension and three-dimension, can be modeled efficiently by studying a few unit cells (or one unit cell) and applying proper PBCs.

2.10 The Nicolson-Ross-Weir Technique

The Nicolson-Ross-Weir (NRW) technique is a tool for converting scattering parameter from the simulation or measurement into electrical properties, which are permittivity, ϵ_r , and permeability, μ_r [72-74].

In the NRW algorithm, the reflection coefficient is

$$\Gamma = \chi \pm \sqrt{\chi^2 - 1} \dots \dots \dots (2-30)$$

where

$$\chi = \frac{s_{11}^2 - s_{21}^2 + 1}{2s_{11}} \dots \dots \dots (2-31)$$

In acquiring the correct root, the magnitude of the reflection coefficient must be less than one ($|\Gamma| < 1$) according to the passivity condition. The following stage is to be followed to calculate the transmission coefficient of the metamaterial.

$$T = \frac{s_{11} + s_{21} - \Gamma}{1 - (s_{11} + s_{21})\Gamma} \dots \dots \dots (2-32)$$

Furthermore,

$$k = \left[\log \left(\frac{1}{|\Gamma|} \right) \right] + (2m\pi - \text{phase}(\Gamma))/d \dots \dots \dots (2-33)$$

$$\epsilon_r = \left(\frac{k}{k_0} \right) ((1 - \Gamma)/(1 + \Gamma)) \dots \dots \dots (2-34)$$

$$\mu_r = \left(\frac{k}{k_0} \right) ((1 + \Gamma)/(1 - \Gamma)) \dots \dots \dots (2-35)$$

where k_0 is the propagation constant of free space.

m is the branch index ($0, \pm 1, \pm 2, \pm 3, \dots$), and d is the thickness of the slab. The integer m has multiple choices, and it is not straightforward to assign the exact solution for the permittivity and permeability. To extract value of the integer m , the group delay technique [73] is calculated at each frequency, and then by taking the difference in phase of the S_{21} data at adjacent frequency points and comparing it with the group delay caused with the assumed value of m , the convergence on the correct value of m is achieved.

2.11 Computer Simulation Technology

The Computer simulation technology (CST) microwave studio is a full-featured software package for electromagnetic analysis and design in the high frequency range. The simulation software in order to design and optimization the devices can choose the most appropriate method for operating in a wide range of frequencies. And can be used to analyze and design transmission lines with arbitrary geometry and number of conductors.

The 2D eigenmode solver used to calculate waveguide port modes can be used to quickly and efficiently characterize the transmission line's properties and the built-in optimizers can be used to optimize line geometry for multiple modes. [L SEP]

CHAPTER 3

METHODOLOGY

This chapter deals with the design methodology used for this project, which includes the description on the selected MTMs structures, simulation and experiment process-the design is being optimized accordingly .The fabrication process is started after the simulation results are the agreed upon.

3.1 Metamaterials Flowchart Design

The implementations of these projects consist of two main parts—software design and samples hardware fabrication. The main steps of the project design are represented in the flowchart in Figure 3.1. The software simulation includes the designing of proposed metamaterials structures and CST Microwave Studio software is used for microwaves simulation.

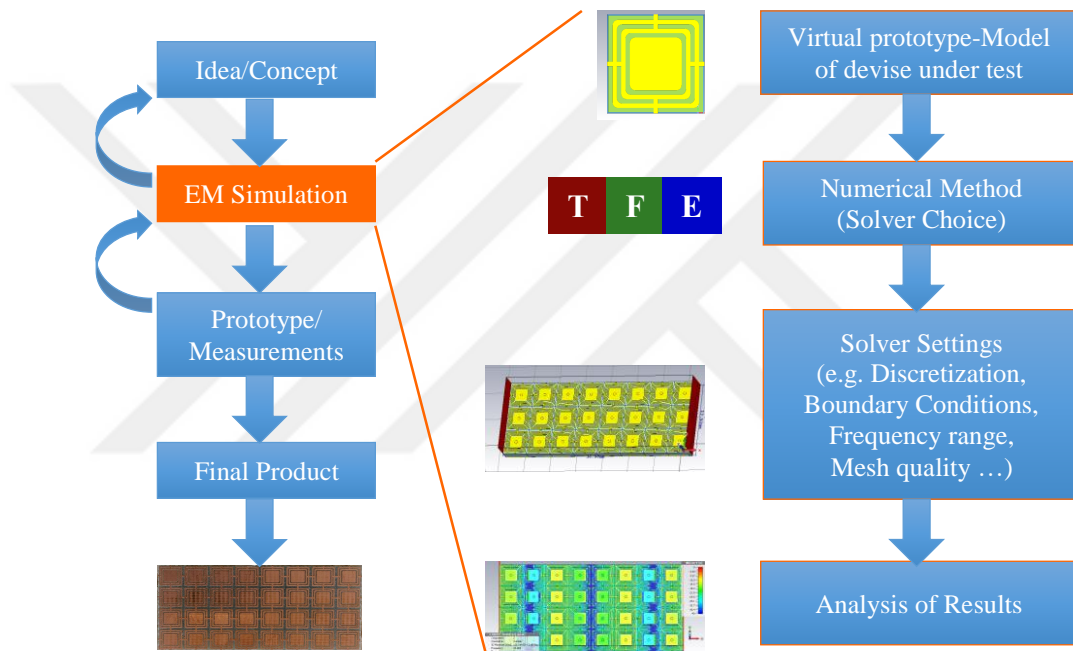


Figure 3. 1 CSTW's flowchart program of designing metamaterial unit cell.

3.2 S-Shaped Split-Ring Resonator Design Specification

A unit cell of the proposed structure is composed of an S-shaped Split-Ring Resonator (S-SRR) which is printed on the front side of a square substrate of side length 16 mm and thickness 1.6 mm [75]. The two ends of the S-shaped SRR are elongated so that they are in the form of C-shaped SRRs. The values of the dimensions of S-shaped SRR with C-shaped SRR ends are provided in Table. 3.1. In the design, FR-4 Epoxy of permittivity $\epsilon_r = 4.3$ and loss tangent $\delta = 0.025$ is chosen as the substrate and copper of electrical conductivity $\sigma = 5.8 \times 10^7$ S/m with coating thickness 0.017 mm is chosen for printing the SRRs see Figure 3.2.

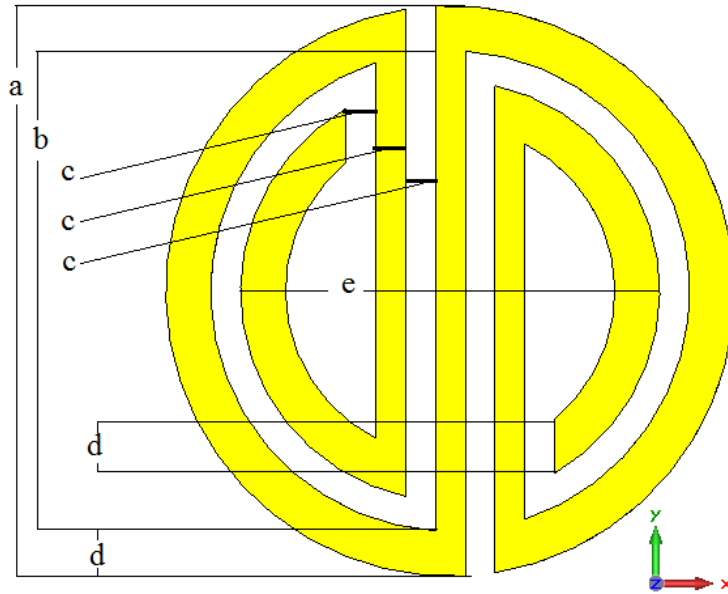


Figure 3. 2 The proposed S-SRR unit cell.

Table 3. 1 S-shaped SRR dimensions (in mm).

a	9.69
b	8.78
c	0.51
d	0.455
e	8.25

3.2.1 Simulation and Boundary

Conditions

A unit cell of the proposed structure together with the ports applied in the simulations is shown in Figures (3.3, 3.4) respectively. In the simulations, the unit cell is placed between two-waveguide ports, which are perpendicular to the direction of the wave propagation, which is along negative z-direction. To imitate the infinite structure, perfect electric boundary conditions are set at the boundary surfaces perpendicular to the E-field while perfect magnetic boundary conditions are at the boundary surfaces perpendicular to the H-field in which the chosen frequency band is the X-band region (8-12 GHz).

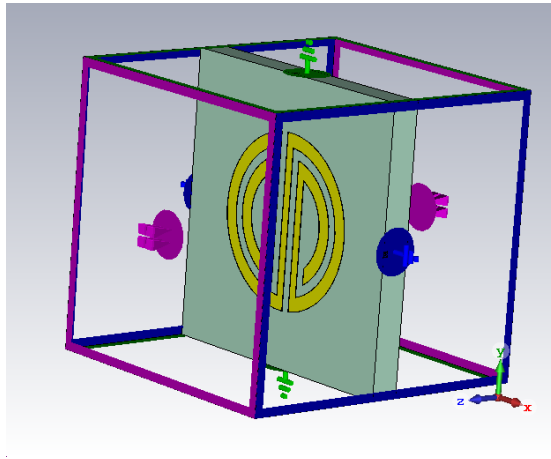


Figure 3. 3 The proposed unit cell simulations setting the boundary conditions.

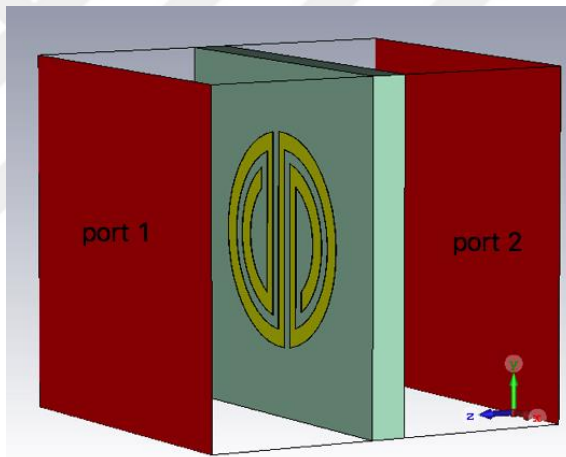


Figure 3. 4 Location of excitation ports.

3.2.2 Experimental Method

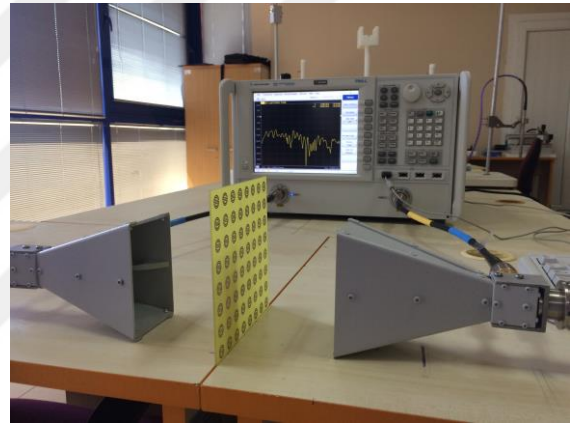
The experiments in this dissertation were performed in the Microwave Laboratory of Electrical and Electronics Engineering Department in Iskenderun Technical University. Before presenting the comparison of the simulated and the experimental results, it would be better to give some information about the experimental setup: 1) the calibration procedure is done using the calibration kit as in Figure 3.5.a, 2) experiment layout is prepared by placing the designed sample between

two horn antennas, which are separated by 16 cm, and connected to a vector network analyzer (VNA) through coaxial cables as in Figure 3.5.b [75,76]. By this way, the surface of the sample shown in Figure 3.6 is guaranteed to be perpendicular to the direction of wave propagation. The incident electromagnetic wave propagates along negative z-axis to excite the combined materials of the sample.

The electric field vector E and magnetic field vector H are in the y-axis, and negative x-axis, respectively see Figure 3.3. For calibration purposes, a measurement is conducted without the sample, then the sample is placed between the two horn antennas and the S-parameters are measured via VNA. The simulated and the measured S-parameter results presented in between (8-12 GHz) will be discussed in the Chapter 4.



(a)



(b)

Figure 3. 5 (a) The VNA calibration kit, (b) VNA, two horn antennas with coaxial cables [75].

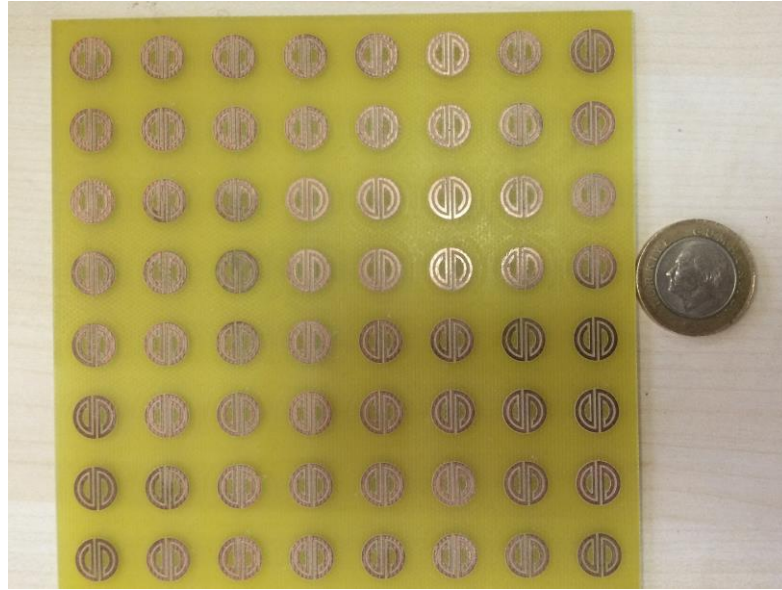


Figure 3. 6 S-SRR manufactured sample.

3.2.3 Absorber Application

Figure 3.7 shows the VNA and the experiment alignment setting. After the calibration test without the testing sample is applied, the horn antenna is used to illuminate the sample in X-band frequency range with distance equal to far-field distance determination. The mathematical expression for determining the minimum separation distance is $R > \frac{2D^2}{\lambda}$, where R is the separation distance between transmitter and receiver antennas, D is the maximum aperture dimension and λ is the wavelength (shortest of the tested).

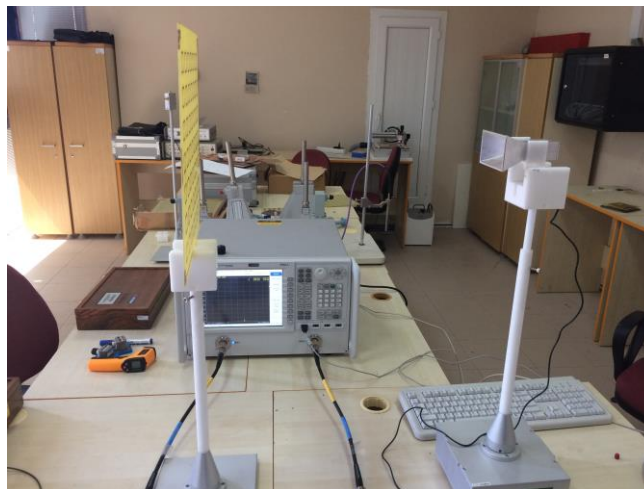


Figure 3. 7 Absorption experiment setting [75].

3.3 Fishnet-Mushroom-like MTMs Structure Modeling

It becomes very desirable to design and fabricate MTMs that can achieve these properties, according to their possible applications in diverse engineering and scientific fields. The metamaterials are designed to use dielectric as host and metal containment, which have been fabricated and then tested intensively in the form of different periodical arrangement [77, 78]. Concerning the flowchart designing process shown on Figure 3.1, the following steps are pursued to complete the required unit cell.

3.3.1 Fishnet-Mushroom-like MTMs Design Specification

The proposed metamaterial EBG unit cell consisted of a square substrate with 4.5 mm at side length and 1.6 mm at thickness [79]. The (FR-4 epoxy) with a permittivity $\epsilon_r = 4.3$ and loss tangent $\delta = (0.025)$ is chosen to represent the substrate material. The metal shape is printed on the substrate front side which is composed of a squared patch surrounded by two square rings connected from their center sides like a net. A cylindrical via with a diameter of 0.5 mm is also located in the unit cell center as shown in Figure 3.8.b, by which the square patch and the ground plan in the bottom side are connected. Copper of electrical conductivity $\sigma = 5.8 \times 10^7$ S/m with coating thickness 0.017 mm is chosen for printing as shown in Figure 3.6.a. the unit cell dimension parameters are mentioned in the Table 3.2.

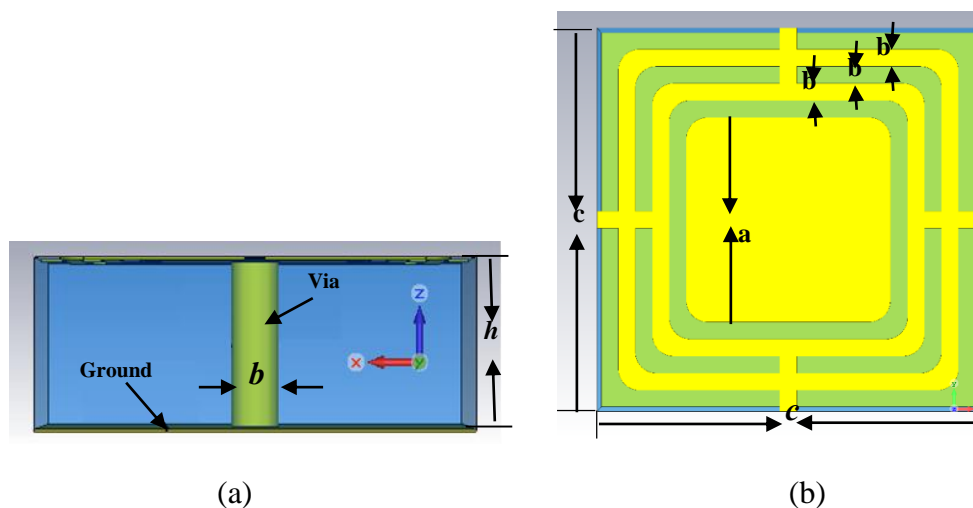


Figure 3. 8 The EBG unit cell schematic, (a) side view, (b) top view.

Table 3.2 Structure dimensions for the EBG unit cell

Parameter	mm	Parameter	mm
a	2.5	d	0.5
b	0.2	h	1.6
c	4.5		

3.3.2 Array Structure Design and Simulations settings

The simulations include the proposed unit cell and are ordered by varying different arrays arrangements [80], like 1x8-cell array and in 3x8, 4x8, and 6x8-cell arrays. These arrangements are set between two waveguide ports in the x-directions in order to simulate S-parameters and obtain the reiterative characteristic parameters, and the Bandgap effect of varying the amount of metamaterial is so.

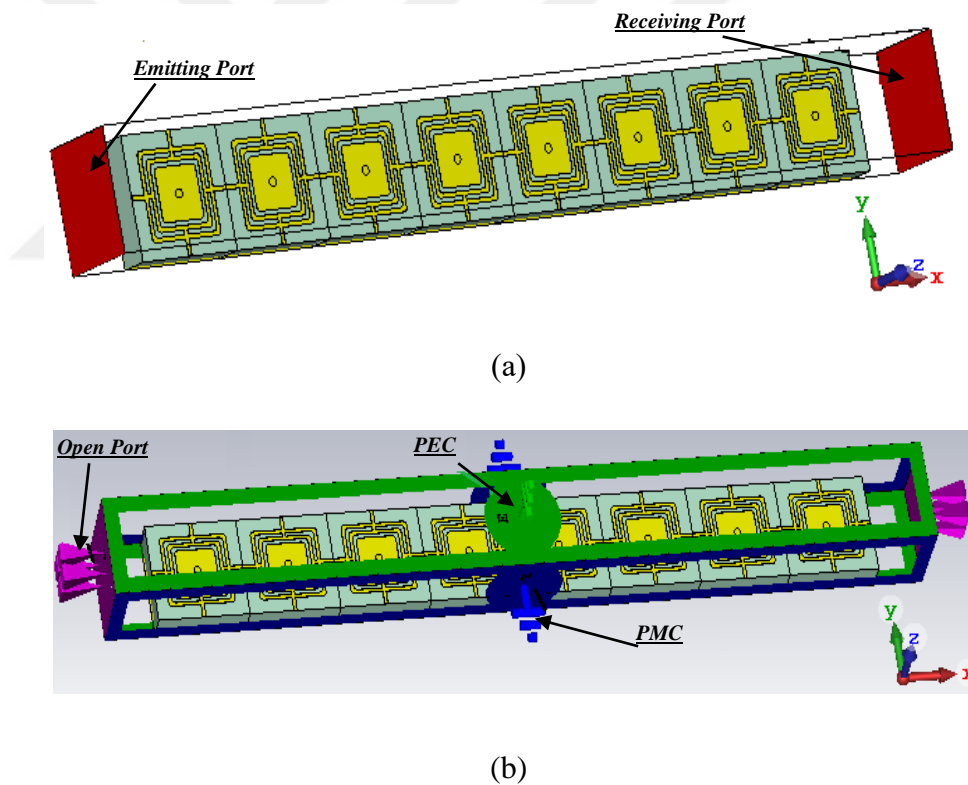


Figure 3.9 EBG array simulation settings achieved by the bandgap measurements, (a) EBG characterization principle, (b) waveguide boundary conditions.

The EBG is analyzed and simulated by applying the sample to a surface wave propagation measurement through the setting procedures that presented in Figure 3.9.a, b.

Furthermore, microwave ports are set on the x-axis sides, on which one port is located as a transmitter generating electromagnetic wave (\mathbf{E} , \mathbf{H}) as shown Figure 3.9.a, and the second port as a receiver. These boundary conditions are chosen in order to define a waveguide structure Figure 3.9.b. Moreover, a perfect magnetic boundary condition (PMC) set in the y-directions in which an infinite periodic repeating in the same directions for the eight-EBG, and a perfect electric boundary condition (PEC) are set in the z-directions, considering a ground plan set in the blow side of the EBG structure, and with the open boundaries in the x-directions which the ports are set.

3.3.3 Dispersion Diagram

The concept of this paper states that the wave propagation direction is assumed in the same direction of the unit cells periodicity. The space harmonics share the same group velocity even if they have different phase velocities for they cannot occur separately. Each single harmonic does not satisfy the boundary conditions of the periodic structure, but their summation does so. Thus, summation is considered to be the same mode. Hence, by simulating a single proposed EBG unit cell structure, an infinite periodic structure model is carried out by CSTMWs Eigen mode simulator (see Figure 3.10).

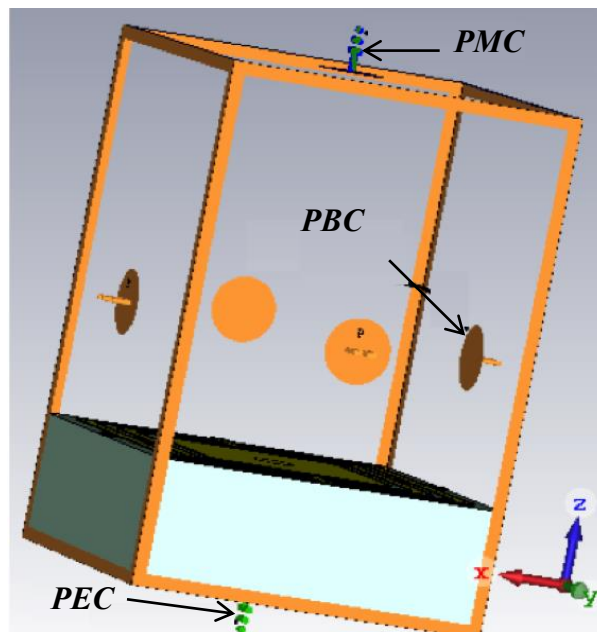


Figure 3. 10 Dispersion diagram boundary conditions setting.

3.3.4 EBG Experimental Method

The experiment steps as followed; first, the WR-90 waveguide is connected with input and the output ports with the network analyzer by the two coaxial probes, and the network analyzer is calibrated. Second, the fabricated sample is fixed at the center of a WR-90 waveguide; all the metallic part that used is unconnected to the waveguide walls schematic experimental is shown in the Figure 3.11.

The dielectric substrate thickness has chosen to be as thin as possible to minimize the dielectric loss. The selected structure dimensions, which severed the optimization goal, proved the double negative performance at around X-Band arena [81, 82].

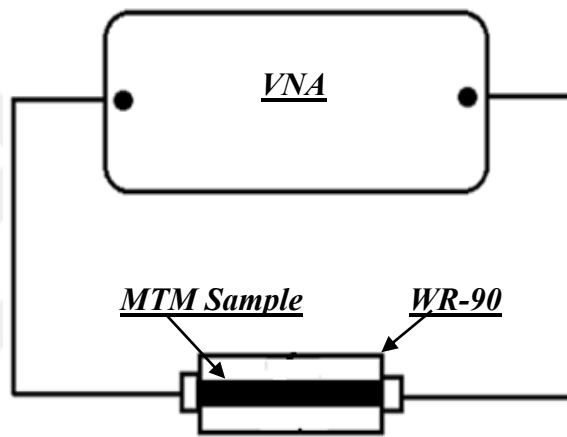


Figure 3. 11 Experimental set-up schematic representation (VAN) vector network analyzer.

3.5 Mutual Coupling Reduction Application

3.5.1 Microstrip Antenna Characteristics

A probe-fed rectangular microstrip antenna with height h 1.6 mm thickness, dielectric Epoxy FR.4 $\epsilon_r = 4.3$ is used, the single microstrip antenna with dimensions described in Table 3.3. The surface waves launch most of the energy supplied to the antenna and significantly deform the radiation pattern due to wave diffraction on the edges of the substrate.

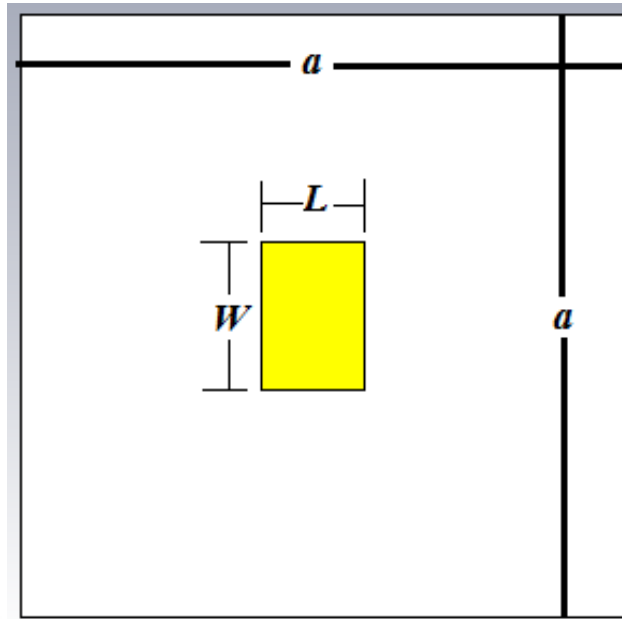


Figure 3. 12 Microstrip antenna top view.

Table 3. 3 Microstrip antenna structure dimensions

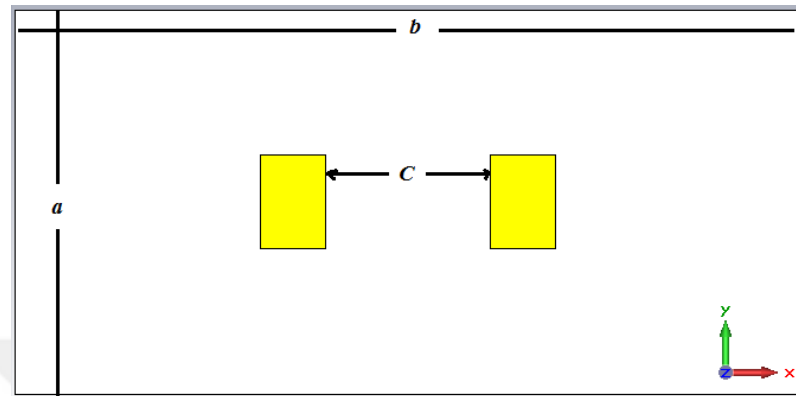
Dimension	mm	Dimension	mm
a	36	S	13.5
b	73.5	W	8.77
c	15.5	h	1.6
L	6.143		

3.5.2 Microstrip Two Array

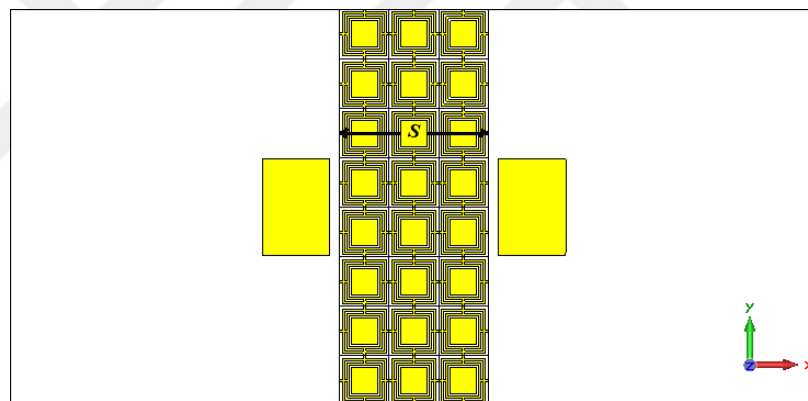
Antennas Structure

A high permittivity substrate exhibits at the E-plane coupled microstrip antennas have been founded and provided very strong mutual coupling due to the severe surface wave, while the electromagnetic band-gap (EBG) structures have the capability to stop the propagation of the surface wave and reduce mutual coupling between antenna elements at certain operating frequency or in a specific band. [83].

Two conventional microstrip antennas separated with 15.5mm as shown in Figure 3.13 a, and, three column with eight elements (3x8) of the proposed EBG has been inserted between the two microstrip antennas as shown in Figure 3.13 b. All structures parameters are given in the Table 3.3.



(a)



(b)

Figure 3. 13 (a) two coupling antennas w/o EBG, (b) two coupling antennas with EBG.

3.5.3 Microstrip Antenna Characteristics

Figure 3.14.a, b, shows a rectangular microstrip antennas with substrate height h 1.6 mm thickness, dielectric Epoxy FR.4 $\epsilon_r = 4.3$ is used, the single microstrip antenna with dimensions described in Table 3.4.

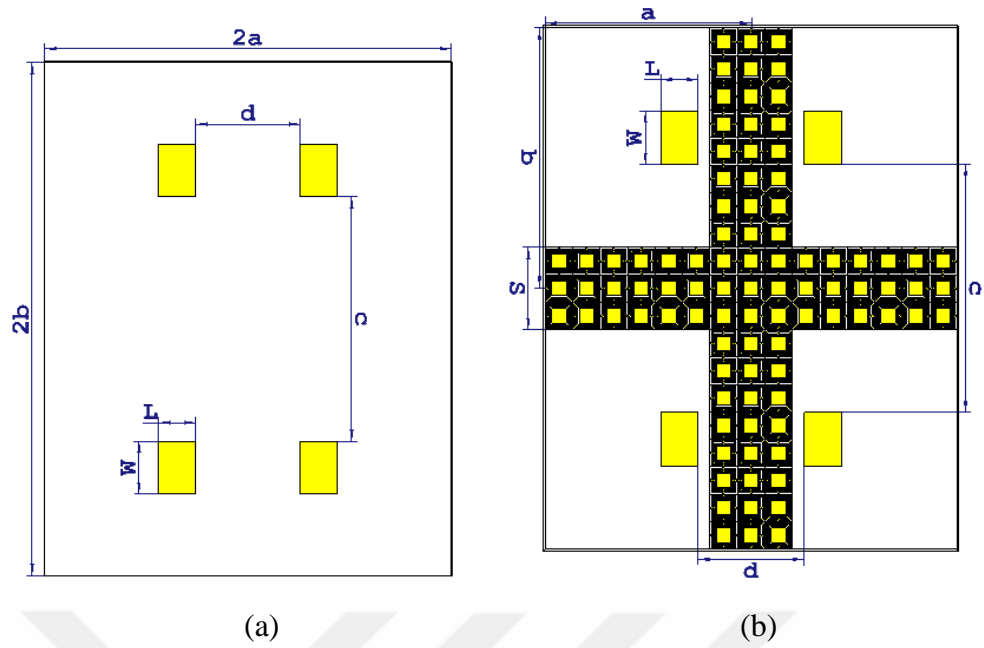


Figure 3.14 Top view for microstrip antennas schema, (a) without EBG, (b) with EBG.

Table 3.4 Four microstrip antennas structures dimensions.

Dimension	mm	Dimension	mm
a	33.75	S	13.5
b	42.75	W	8.77
c	40.73	h	1.6
d	17.36	L	6.143

CHAPTER 4

RESULTS AND DISCUSSION

4.1.1 S-SSR RESULTS

The simulated and the measured S-parameter results between 8-12 GHz (X-Band regime) are presented in Figure 4.1 in phase (degree) and Figure 4.2 in magnitude (dB), respectively. There are some small differences between the two obtained data, which may be due to the manufacture tolerances related to the dielectric dispersion and the etching process.

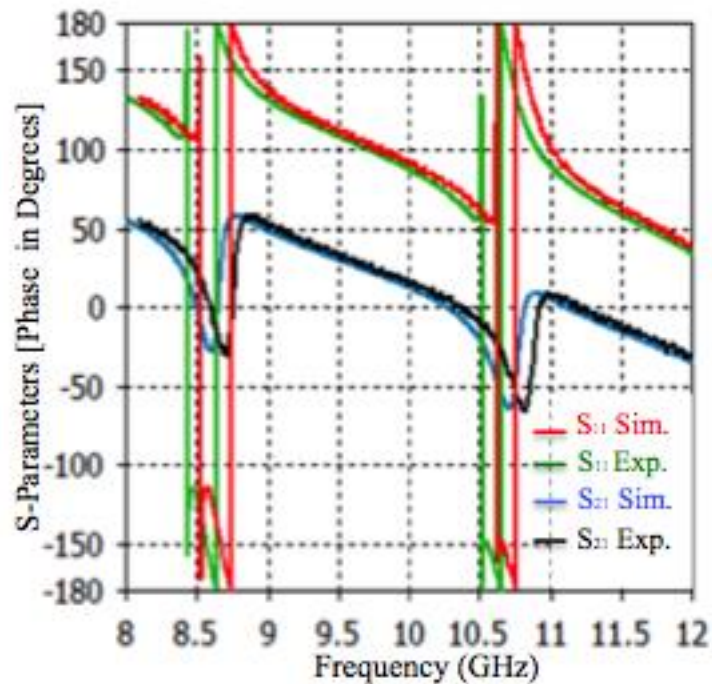


Figure 4.1 S-SRR simulated S-parameters (a) magnitude (dB), (b) reflection phase (degrees).

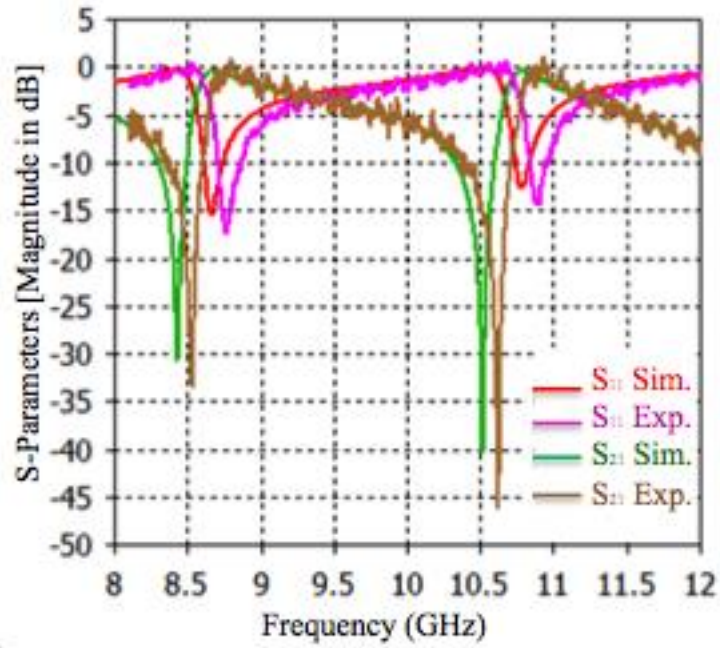


Figure 4.2 S-SRR measured S-parameters, (a) magnitude (dB),
(b) reflection phase (degrees)

Figure 4.3 presents the simulated and the experimental results for the real parts of the effective permittivity and permeability together with the real part of the refractive index of the structure. The effective permittivity and permeability are obtained by the use of Nicholson-Ross-Weir method [72-74]. The structure has negative real parts in the frequency bands ~ 8 -10.45 GHz and ~ 10.65 -11.75 GHz for the permittivity and in the frequency band ~ 8.5 -12 GHz for the permeability. Thus, the proposed structure exhibits a wideband metamaterial behavior.

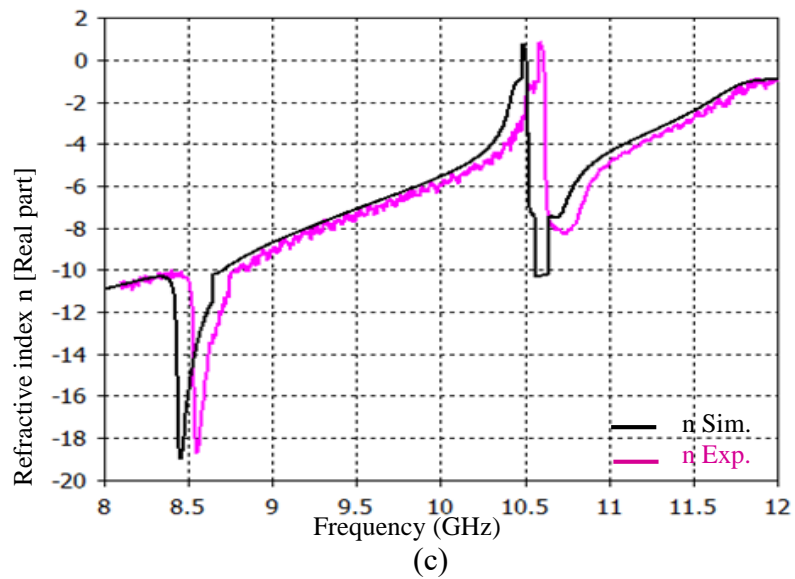
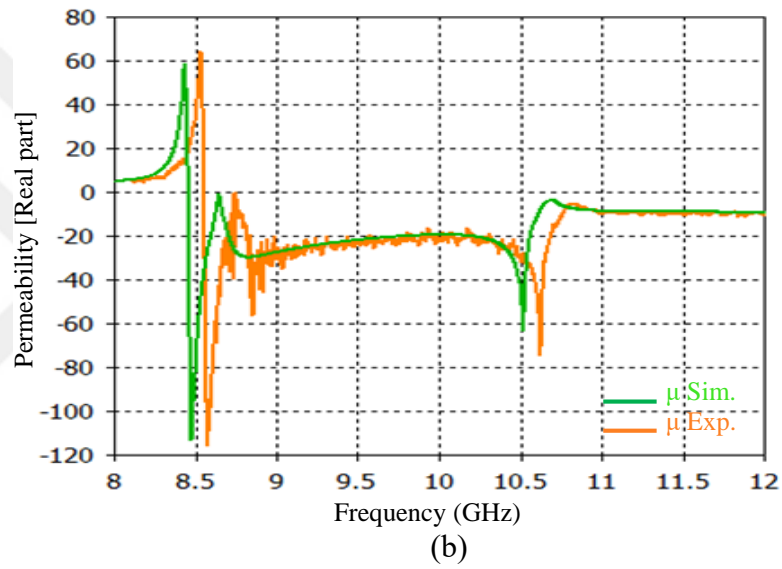
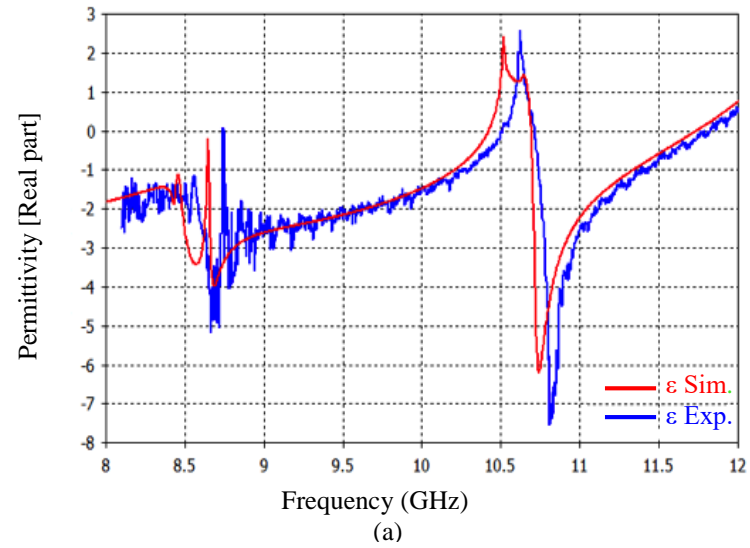


Figure 4.3 The simulated and experimental results for the real parts of, (a) permittivity (b) permeability and (c) refractive index.

4.1.2 Electric Field, Magnetic Field and Surface Current Distributions

Basically, the non-homogenous metamaterial structures provide a resonant RLC circuit behaviour in some certain frequency band. For the specificity geometric design in this study, the S-shaped SRRs behave like inductors and the gaps as capacitors. To understand how the structure behaves when placed in an electromagnetic region, the surface current distribution is presented in Figure 4.4, and the magnetic and electric field densities presented in Figure 4.5 at the operation frequency 10.75 GHz. Hence, both figures show the formation of the magnetic between the top and bottom edges of both SRRs in which the current flow identifies the magnetic field distribution. Furthermore, the electric field is localised around the gaps, and it is in consistent with the magnetic field as seen in Figure 4.5 at which the structure behaves like a left-handed material has both negative effective permittivity and permeability [84, 85].

It can be observed from Figure 4.4 that the current is highly concentrated on the central wire and the copper shape structure. The magnetic field shows similar distribution as the current in Figure 4.5 b. The gathering between the virtual gaps which are represented by the current minimum points and with the actual gaps, providing an additional capacitance-like response by being the voltage maxima points simultaneously [84, 85].

In addition, the electric field distribution in Figure 4.5 a, shows that the concentration of the electric field is high at regions where there is capacitive effect. One of the reasons behind this capacitive effect is the Gaps in the structure. The other reason is the occurrence of the current minima due to the alternating current on the copper. Furthermore, the alternating currents on the copper structure are providing virtual gaps on each side, the surface current flow on conductor and in every virtual gap is divided into two oppositely directed pieces, nearly gave the same image in the both sides and balancing each other.

Furthermore, the surface current flows are moving toward the actual gaps and they start their circulations from conductor ends. These dynamics exist in wide band, at which the effective permittivity and permeability are simultaneously negative. Moreover, the surface current densities are forming as if they are going to spread out from a common point in opposite directions as shown in Figure 4.4 [84, 85].

The stronger the surface current flows excited, and the larger the amount of magnetic field clouds concentrating at the ring resonators. The gaps placed at the centres of the rings are behaving well as capacitors, so the induced magnetic energy densities are diffused at the edges of the gaps, including the virtual ones.

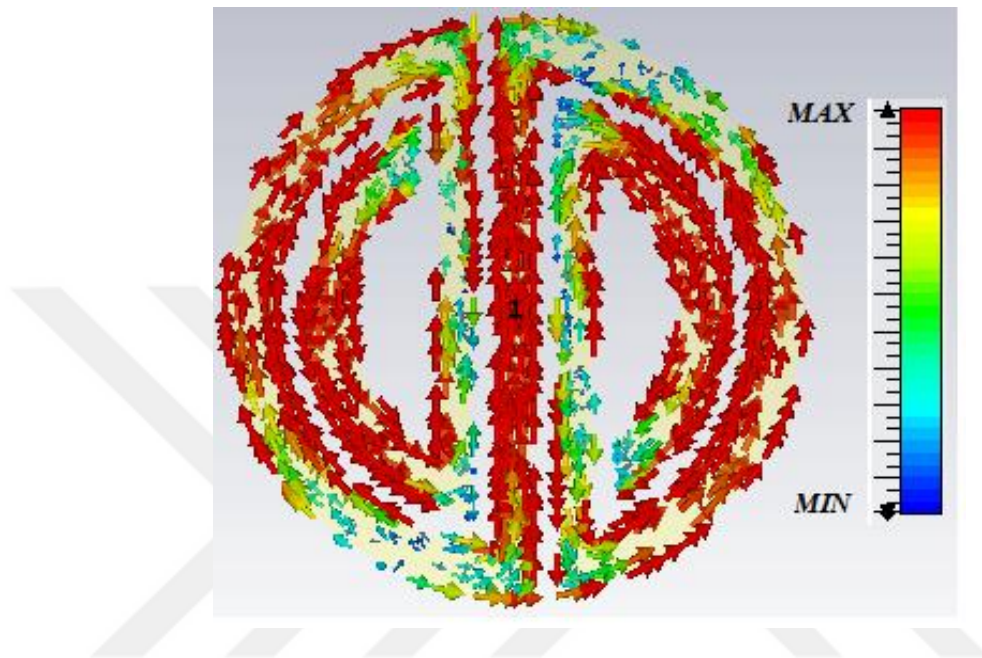
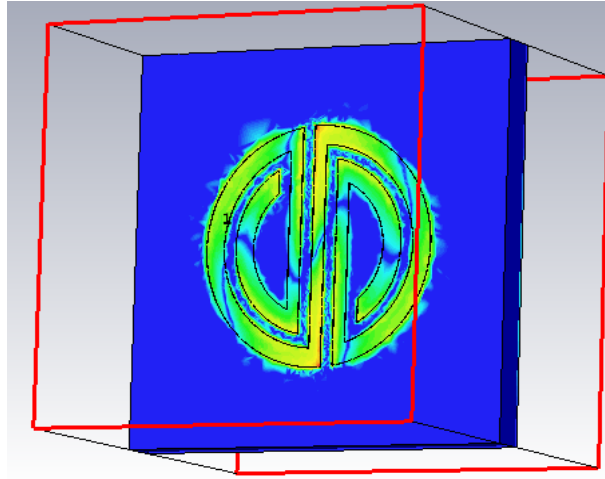
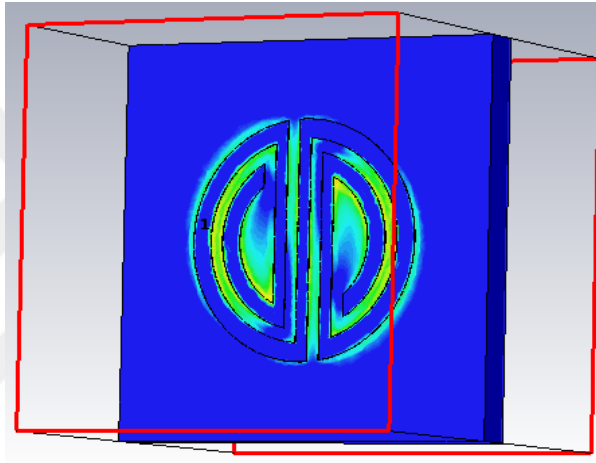


Figure 4. 4 The surface current distribution at 10.75 GHz.



(a)



(b)

Figure 4.5 (a) Electric field, (b) magnetic field distributions for the proposed unit cell at 10.75 GHz.

4.1.3 Absorber Application and Result

To scrutinize the performance of the proposed S-shaped SRR, the absorption characteristics of the structure are studied. The absorption of a material function of frequency can be formulated by $A(\omega) = 1 - R(\omega) - T(\omega)$, where $R(\omega) = |S_{11}|$ and $T(\omega) = |S_{21}|$ represent the reflection and the transmission characteristics, respectively [9]. In order to maximize the absorption, both the reflection and the transmission can be minimized at the resonance frequency. In this study, a copper layer on the backside of the substrate material is added, so that the absorption expression is reduced to $A(\omega) \approx 1 - R(\omega)$, and it almost depends only on reflection now.

The measurement results show good agreement with the simulation results see Figure 4.6. The suggested model provide maxima in the absorption are experimentally obtained around 99.99% at 8.94GHz, in which a perfect absorption numerically and experimentally is seen apparently.

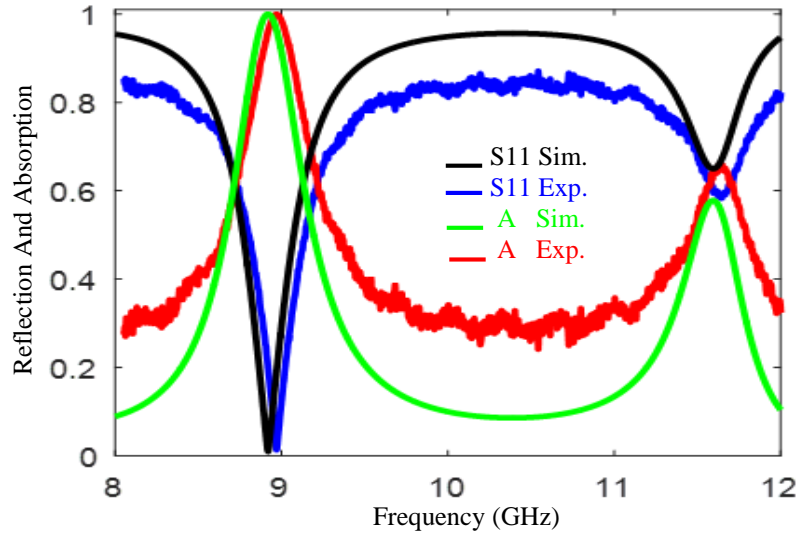
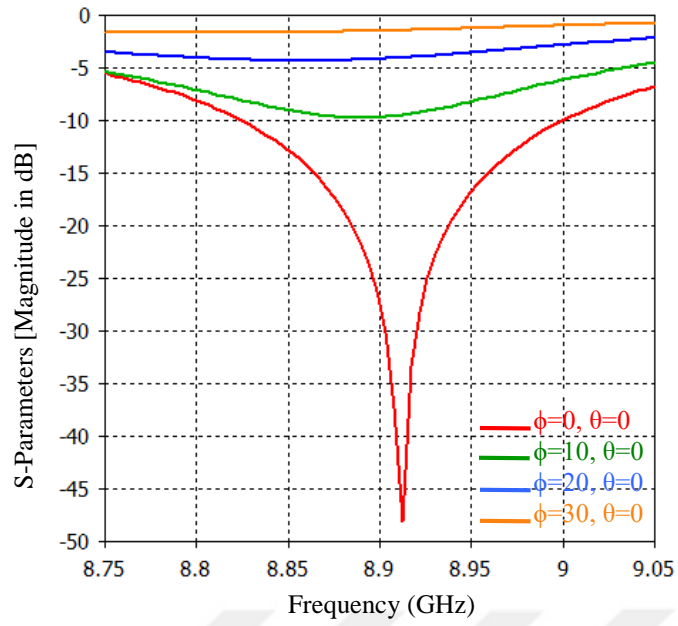


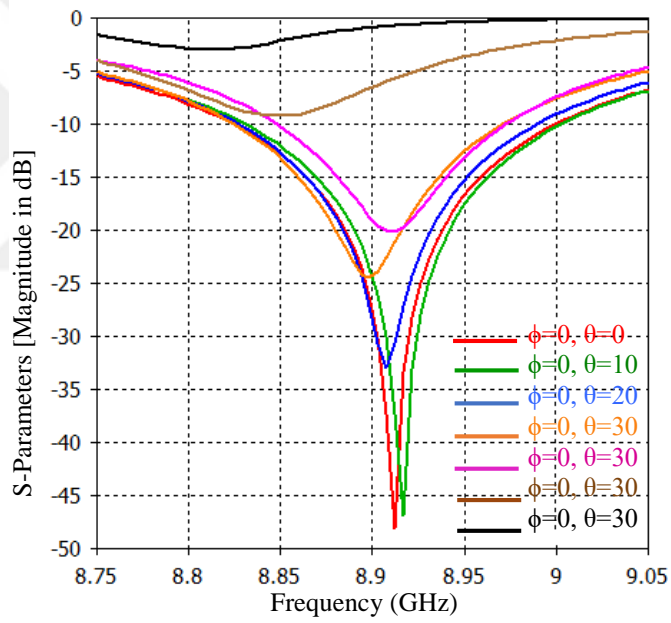
Figure 4. 6 Reflection and absorption ratio simulated and measured results.

The results show that the proposed structure can be used for perfect absorption applications. Note that, the discrepancies between the experimental and simulation data are imputed to fabrication tolerances and dielectric dispersion of the substrate. The misalignment during the experiment may also be considered as another source of error.

The S-parameter and the absorption characteristics are simulated for different polarization angles in 8.75-9.05 GHz frequency band. In Figure 4.7, S_{11} is presented for normal and oblique incidences. It is observed that reflection achieves its lowest value in normal incidence case and the resonance occurs around 8.912 GHz. As the polarization varies from normal to oblique incidence, the reflection also varies and a stable frequency response can be obtained for $\theta < 40^\circ$ when $\phi = 0^\circ$.

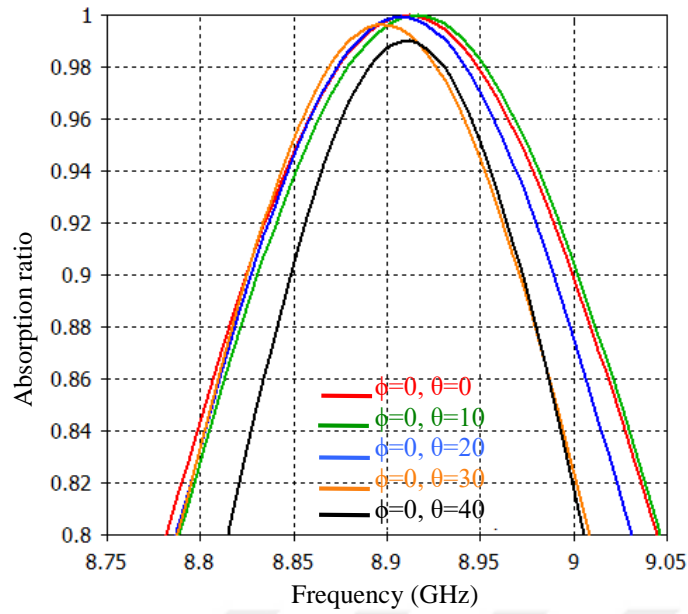


(a)

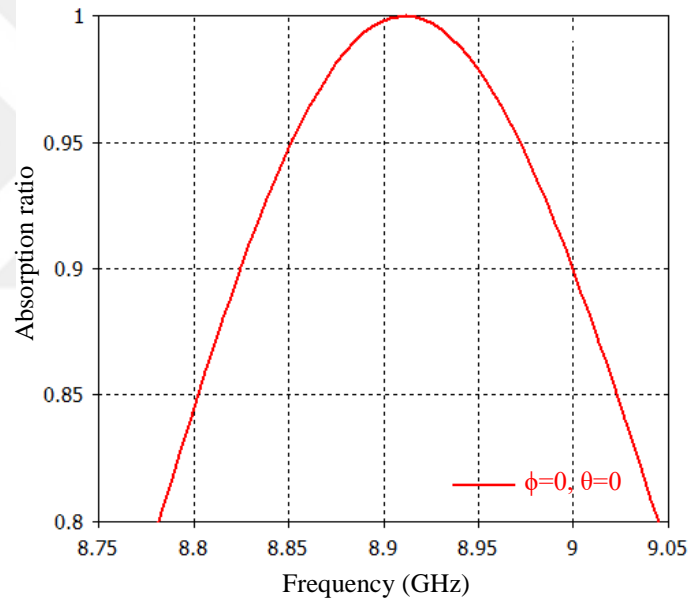


(b)

Figure 4.7 Frequency response of for different polarization angles $\theta = 0^\circ$ and ϕ varies, (b) θ varies and $\phi = 0^\circ$.



(a)



(b)

Figure 4.8 Absorption for different polarization angles, (a) θ varies and $\phi = 0^\circ$, (b) $\theta = 0^\circ$ and $\phi = 0^\circ$.

In Figure 4.8, the absorption characteristics provides the frequency band 8.75-9.05 GHz for the polarization angle θ between 0° and 40° . It can be deduced that the proposed metamaterial can be used as a narrow-band 175 MHz perfect absorbers with absorption over 90% in 8.825-9.0 GHz. At the resonant frequency around 8.912 GHz,

S_{11} is 0.0039. Correspondingly, the absorption rate is 99.99% at the resonance and the device can be used as a perfect absorber at the mentioned frequency.

4.2 Fishnet Mushroom-Like EBG Results

Recently, the fishnet structure has been attracted a great potential approved in the studies. Basically, the strategy to acquire the negative permeability is to create exciting circular currents that can generate a strong magnetic resonance, while expected to produce the negative permittivity by virtue of the electric plasma response with added continuous wires. When negative refraction index is consistent with the negative permeability, consequently most of fishnet structure researches concentrated on characterizing and modeling their magnetic resonance [86-89].

4.2.1 Dispersion Diagram and EBG Location

The bandgap characterization for EBG unit cell that is shown in Figure 3.2. According to the finite element model, the field for the first mode is TM dominant started at zero frequency, and the eigen frequency increases with the wave number, reaching the maximum frequency 8.45GHz. It also decreases following the light line down to a certain frequency. The second mode starts at a higher frequency, and continues increasing with a slope under the vacuum's speed of light, which is set by a straight line. Figure 4.9 shows the band gap is near 4 GHz for this particular structure between (8.45-13.15) GHz. [90,91]

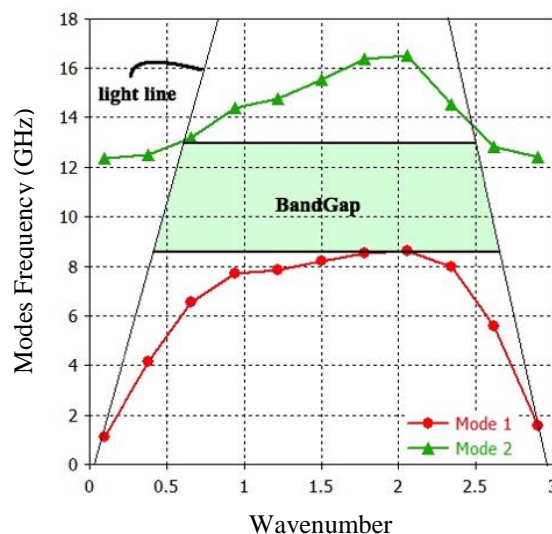


Figure 4. 9 EBG Dispersion Diagram.

4.2.2 S-Parameters and retrieval characteristic parameters

Corresponding to the method described before, surface waves propagating and travelling through the circuit board were detected, and the amplitude and phase for the reflection and transmission data are measured

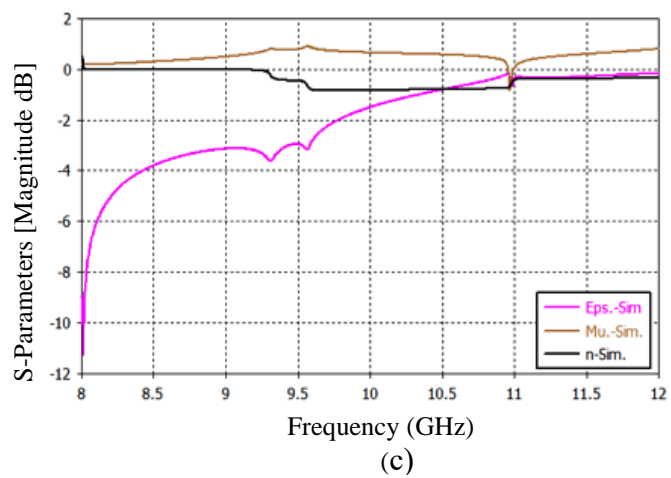
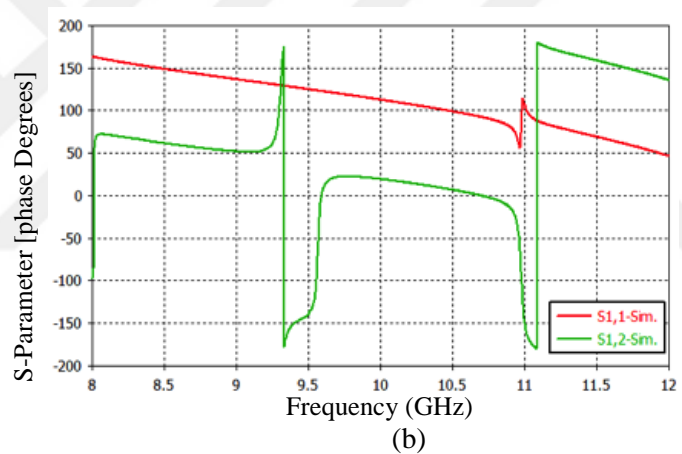
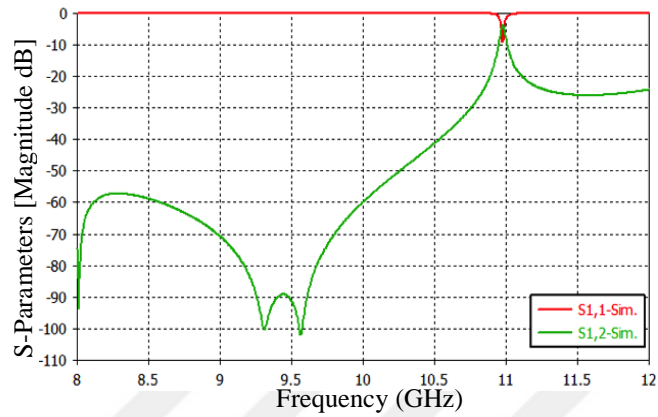
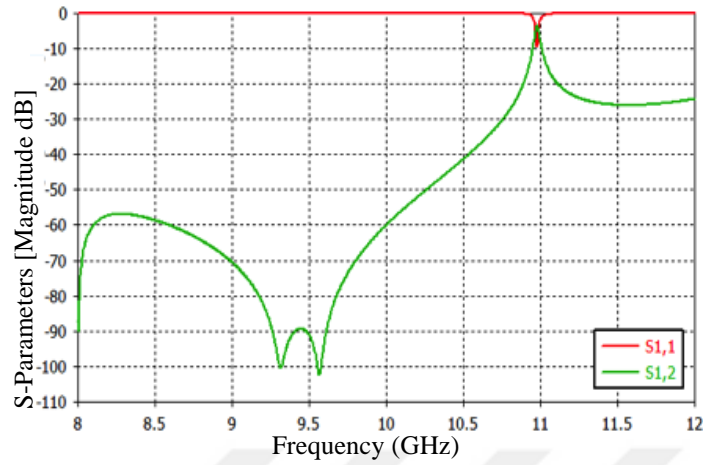
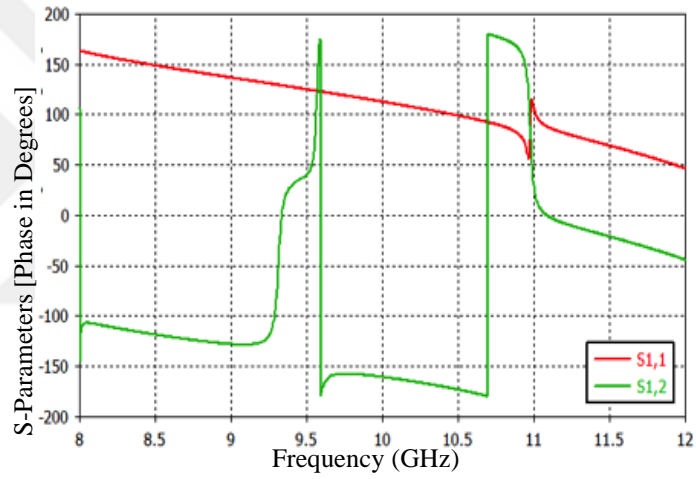


Figure 4. 10 3x8 Array arrangement, simulated parameters (a) magnitude in dB (b) phase in degree, (c) retrieval characteristic parameters.

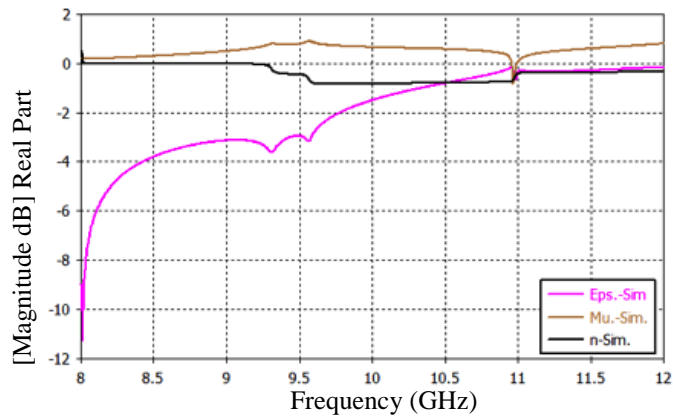
The previous Figures show simulated S-parameter data and retrieval characteristic parameters that extracted to investigate the different array arrangements structure to find the best agreement between them and suitable to be tested practically.



(a)

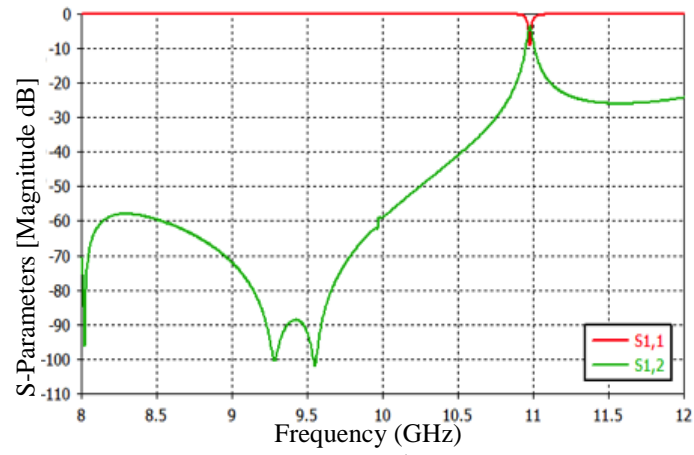


(b)

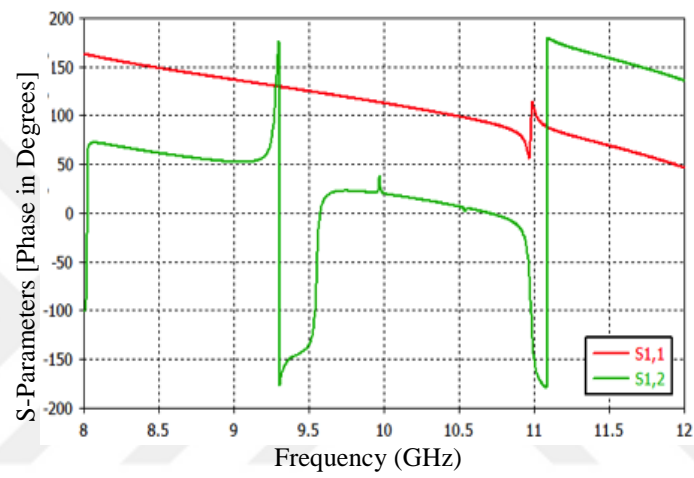


(c)

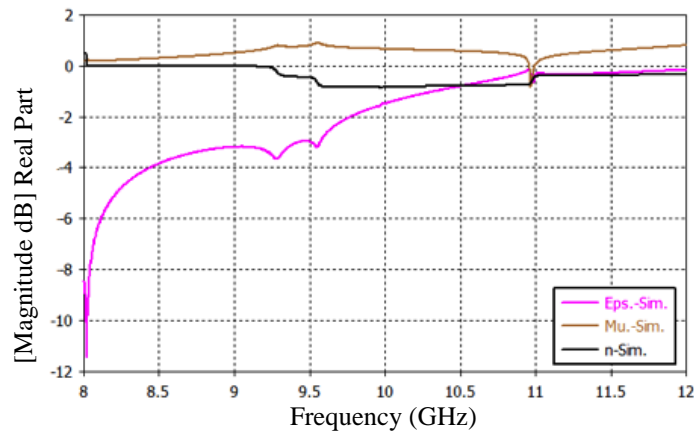
Figure 4. 11 4x8 Array arrangement, simulated parameters, (a) magnitude in dB, (b) phase in degree, (c) retrieval characteristic parameters.



(a)



(b)



(c)

Figure 4. 12 6x8 Array arrangement simulated parameters, (a) magnitude in dB, (b) phase in degree, (c) retrieval characteristic parameters.

4.2.3 Simulated and Measured Results for 4x8 Array Arrangement

For experimental reason to suit in the WR-90 dimensions and to decrease the misalignment experiment duration such as position of the fabricated sample plate the array 4x8 arrangement is chosen to be fabricate (see Figure 4.13).

The reflection coefficient S_{11} , transmission coefficient S_{21} and the retrieval characteristic parameters have a negative index, whereas the permittivity and the permeability are in the X-Band frequency range. The simulation results exhibit that the structure has been designed successfully, that is, the simulation results and the obtained experimental data are agreed with each other quite well.

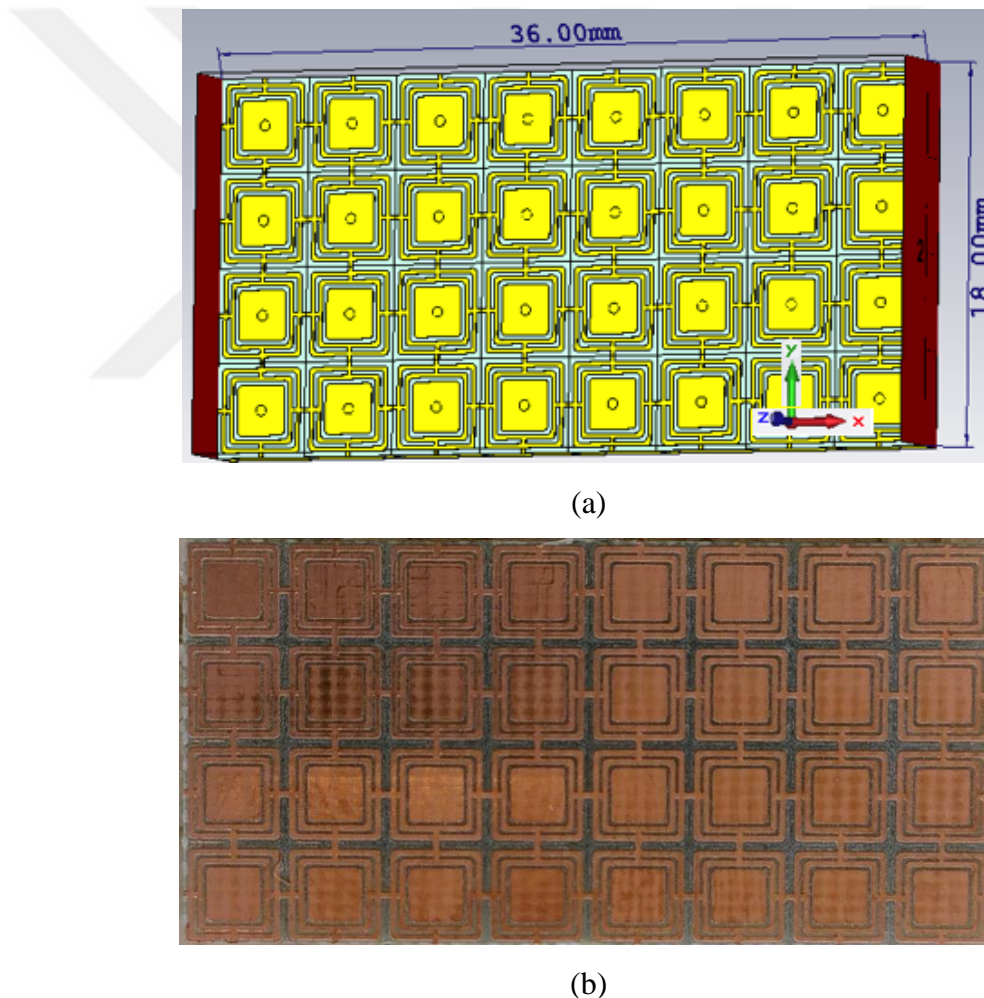


Figure 4. 13 (a) The simulated 4x8 arrangement sample, (b) the fabricated 4x8 arrangement sample.

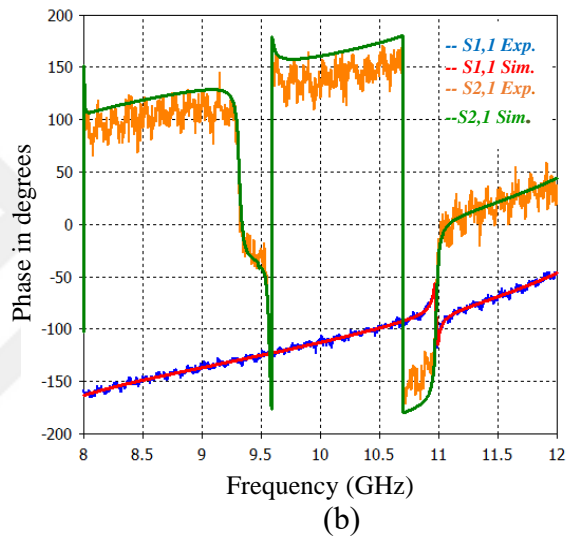
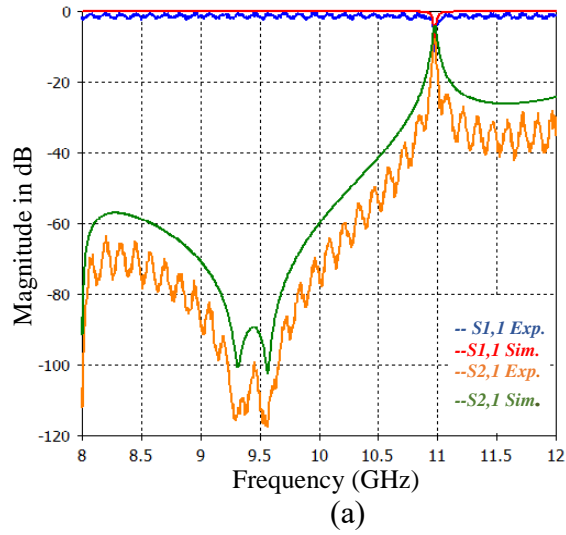


Figure 4. 14 Comparison of the simulated and measured S-parameters.

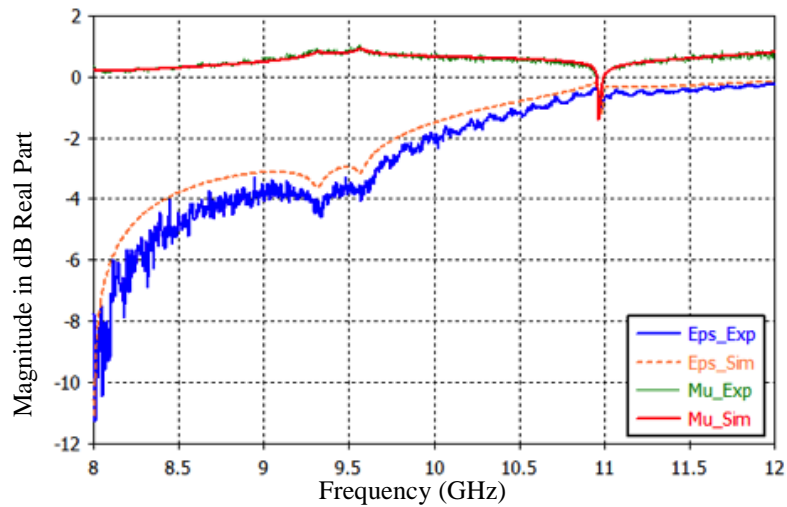


Figure 4. 15 Comparison of the simulated and measured retrieval characteristic parameters.

The experimental and the simulated results in Figure 4.15 show a small difference in minor deviations between the measured and the simulated data are pointed to manufacture allowance that related to PCB fabrication and the gathering process and the quality of the dielectric FR4 dispersion, which used as substrate. Likewise, the misalignment experiment duration such as position of the fabricated sample plate, which cannot be neglected, port receptacle locations, loss characteristics of the materials are possible regarded as another root of error. On the other hand, the extent of measurement accuracy can be elucidated through the convergence between the results of experimental and simulations outcome.

The effective parameters for the investigated structure material can be obtained, based on; the effectively homogeneous medium is occurred when the periodicity of the structure is much less then the propagation wavelength in the propagation direction. The experimented metamaterial behaved as a LHM in the region between (10.95 and 11) GHz and the transmission peak is indicated at 10.975 GHz.

It is clear that the boundary conditions selected to treat the designed structure as an infinite homogeneous material in a certain region is led to frequency observation [91], where both the dielectric permittivity and magnetic permeability are simultaneously negative.

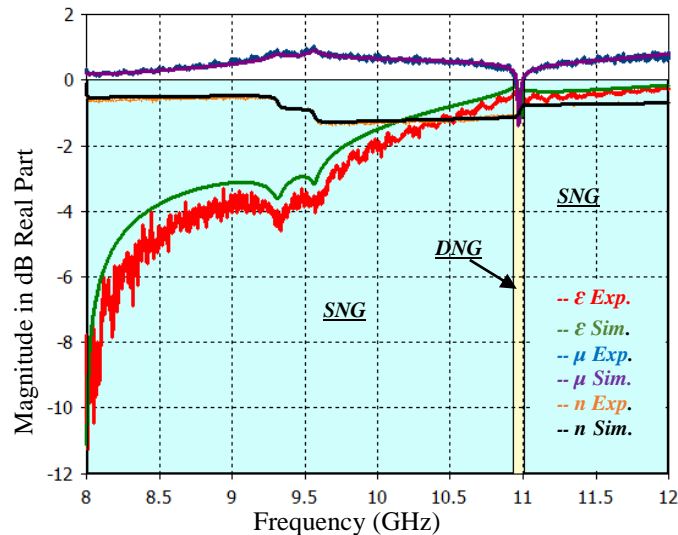


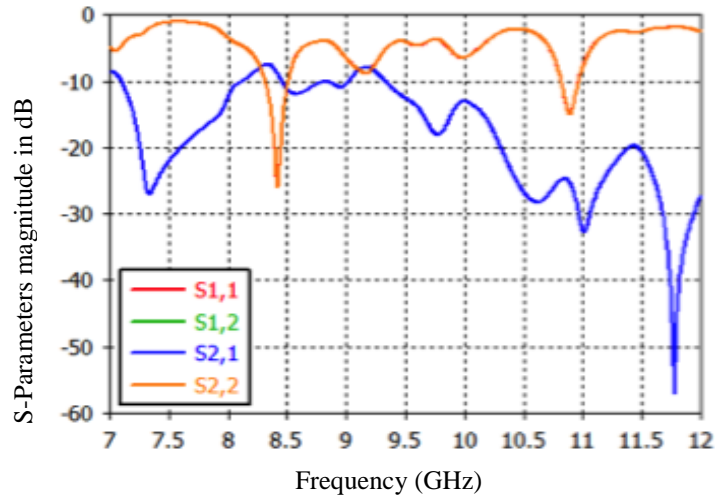
Figure 4. 16 SNG and DNG regions.

The NRW method is used in the material parameters calculation that are extracted and presented in Figure 4.14 a, b. As the figure shows, the metamaterial structure exhibits a negative permittivity in all X-band simultaneously with negative permeability in a band between 10.950 and 11 GHz, where a high band transmission peak covered. In spite of the NRI wide-band is included all the X-Band see Figure 4.15, that type of the Negative Refraction Index is not supporting the LH behavior, Mention that Figure 4.16, is the representation of the SNG occurred only with negative real part of the permittivity. Consequently, both the SNG (between 8 and 10.95 GHz and between 11 and 12 GHz), and or the DNG (between 10.95 and 11 GHz, LH region) characteristics have been supported by the real part of the negative refractive index [65,83]. Due to the coupling between the electric field and the copper parts and because of strips as in the continuous-wires case; the permittivity exhibits a Drude-like behavior. Also, the permeability shows Lorentz-like behaviour, through a strong resonant response to the magnetic field during the magnetic resonators condition.

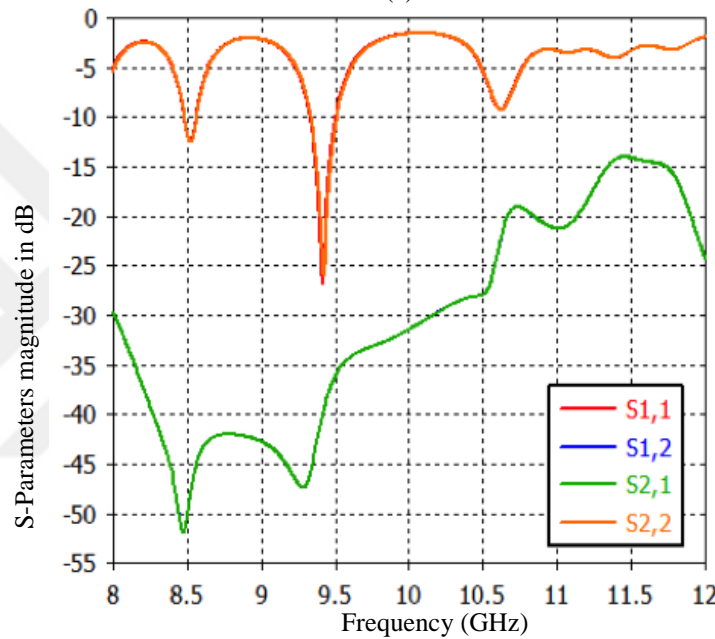
4.2.4 Mutual Coupling Reduction of Dual-Band For Two Microstrip Antennas

The return loss and the coupling coefficient of the antenna array with and without the EBG structures are shown in Figure 4.17. It is observed that the antennas resonate around 8.42 GHz is -27.02dB and -8.3dB coupling coefficient and at 9.415GHz the return loss equal to -5.5dB and -8.83dB coupling coefficient.

Three columns with eight lines (3x8) of the proposed EBG have been inserted between the two microstrip Antennas Figure 3.11, all structures parameters are shown in the Table 3.3 (see page 41), as the proposed EBG separation band is predicted, where it has ability to suppress surface waves, and exhibit a good isolation improvement (mutual coupling) between the Antenna elements, meanwhile, the EBG structure the mutual coupling characteristics improved around the resonate frequencies 8.52GHz (-12.41dB) return loss and -26.2dB coupling coefficient, simultaneously, at 9.415GHz (-27.1dB) return loss and -42.5dB coupling coefficient. The results obtained from the simulations exhibit high mutual coupling.



(a)



(b)

Figure 4. 17 The return loss and the coupling coefficient (a)without EBG structure, (b)with EBG structure.

Since the EBG unit cell is a resonating element, the simulation results indicate that the existence of the EBG structure has some effects on effective resonance frequency f_o position and shifted them as well as affecting the $S_{1,1}$ parameters. Figure 4.18 a, b, shows E-Field intensity with and without EBG structure at 8.42GHz and also Figure 4.19 a, b, shows the H-Field intensity, Figure 4.20 a, b, shows E-Field intensity with and without EBG structure at 9.415 GHz and also Figure 4.21 a, b, shows the H-Field intensity.

Figure 4.20 a, b, shows E-field intensity with and without EBG structure at 9.415 GHz and also Figure 4.21 a, b, shows the H-field intensity.

It was clear that the E and H-fields intensity has been reduced on the second antenna surface substrate due to the EBG structure, dictating the reduction in mutual coupling and improvement in the isolation between the array elements. Furthermore, Figure 4.22 and Figure 4.23 show the radiation characteristics at 8.52 GHz and Figure 4.24 and Figure 4.25 show the radiation characteristics 9.415 GHz respectively for both array configurations. The radiation patterns are not disturbed after EBG structure existence and in considerable amount although it is slightly improved. The figures exhibit that the radiation efficiencies show that presence of the EBG there is an enhancement more than 14% in the vicinity of the resonance frequency.

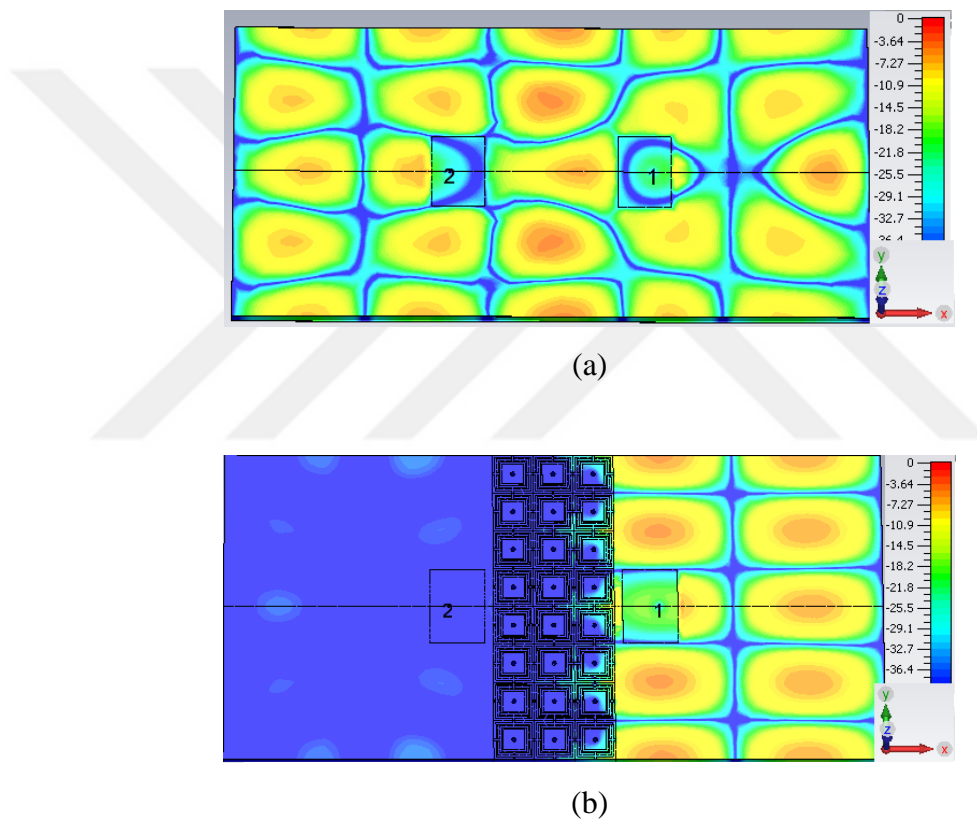
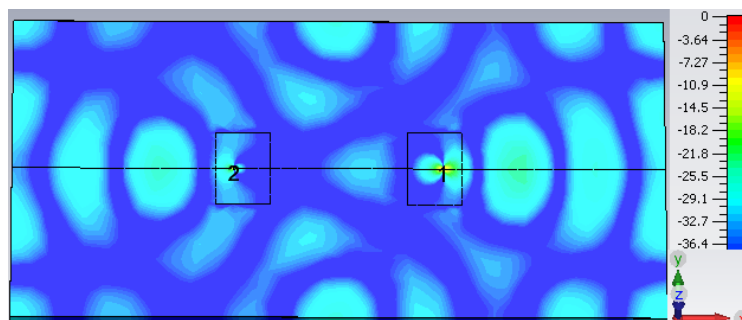


Figure 4. 18 E-field intensity, (a) without EBG, (b) with EBG at 8.42 GHz.



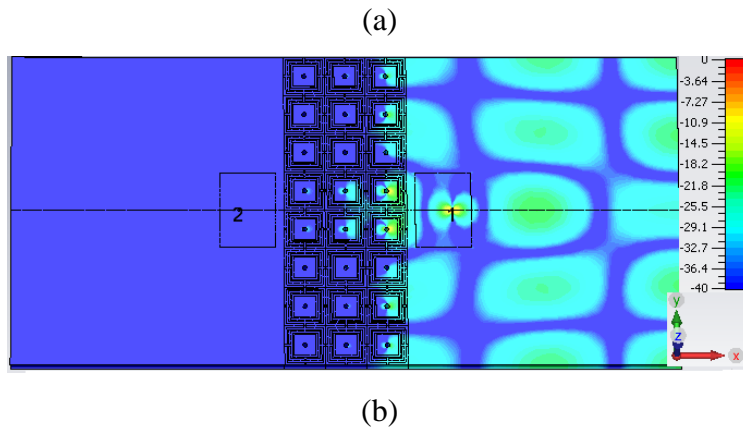


Figure 4. 19 H- field intensity, (a) without EBG, (b) with EBG at 8.42 GHz.

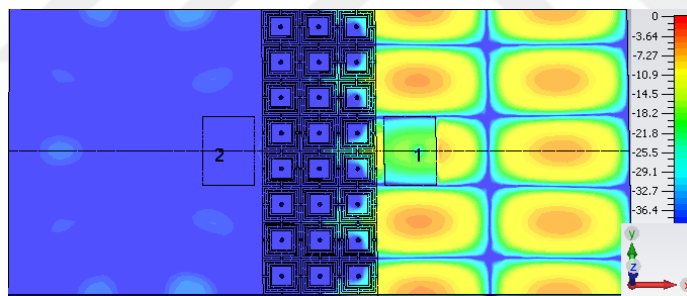
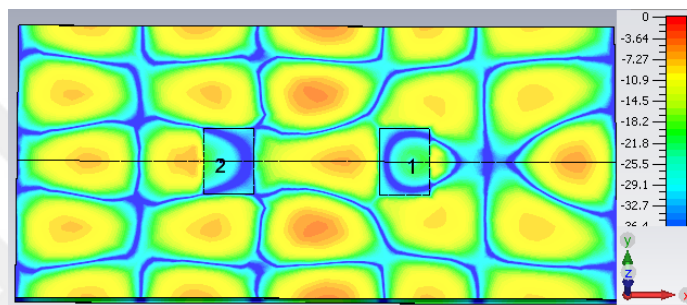
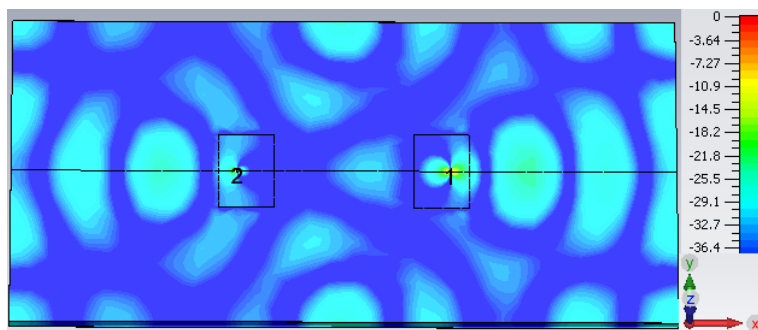
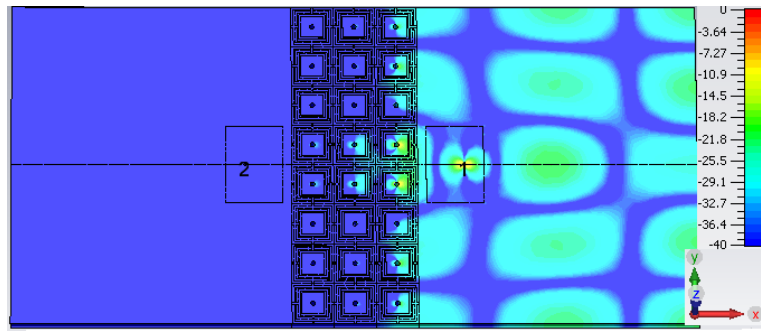


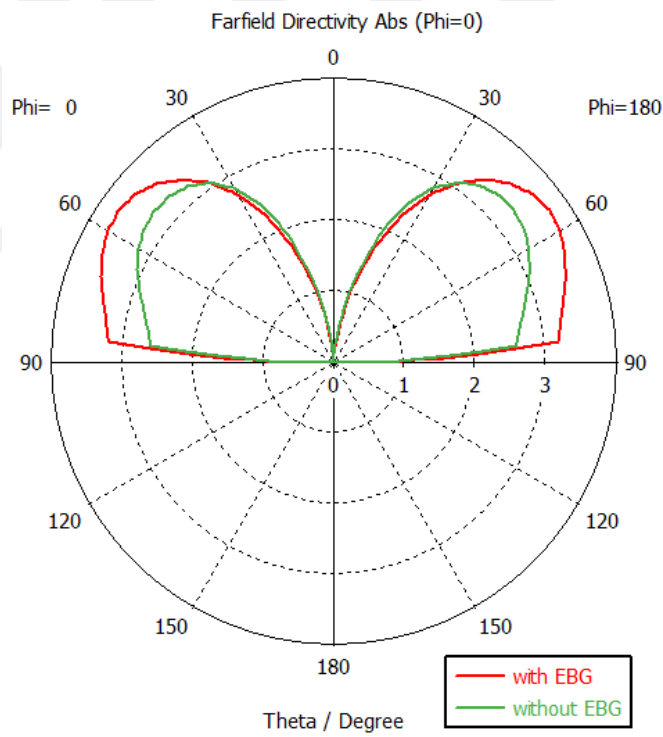
Figure 4. 20 E-field intensity, (a) without EBG, (b) with EBG at 9.415 GHz.



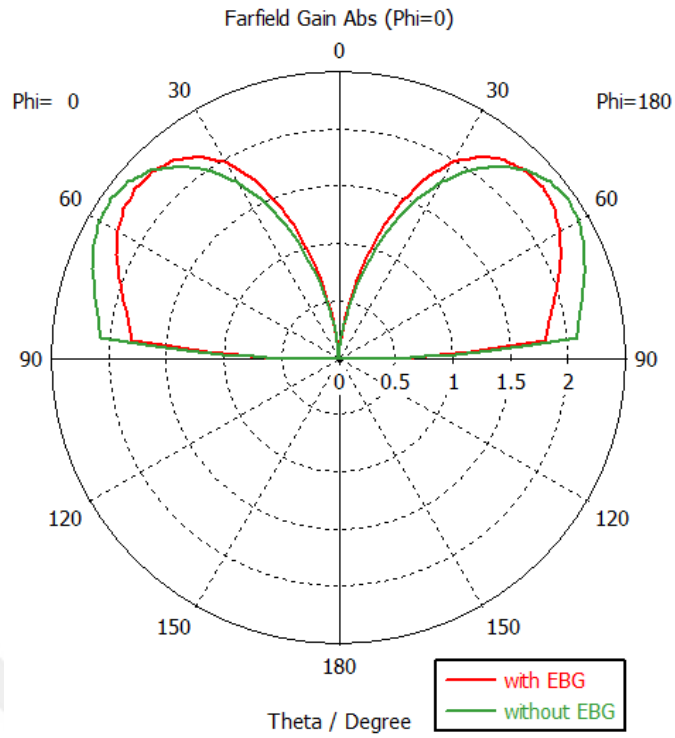


(b)

Figure 4. 21 H-field intensity, (a) without EBG, (b) with EBG at 9.415GHz.

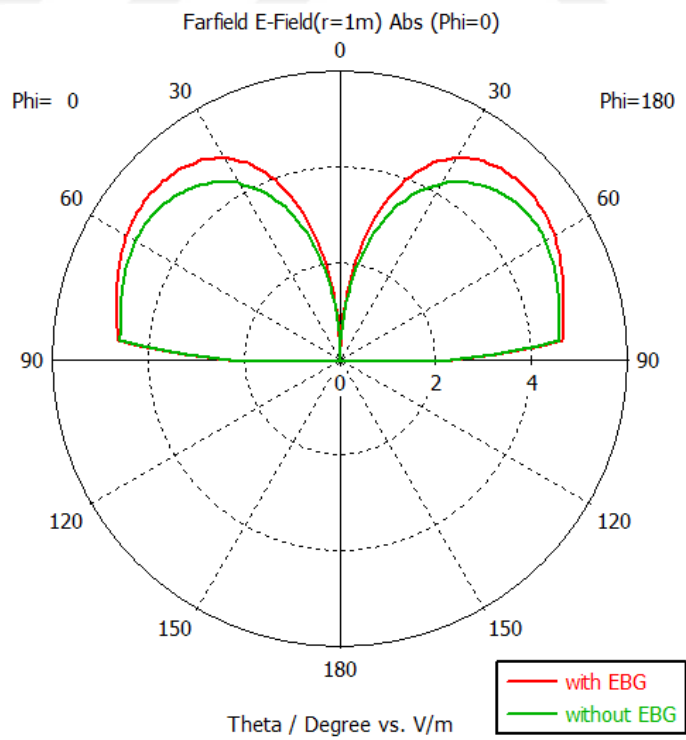


(a) Directivity

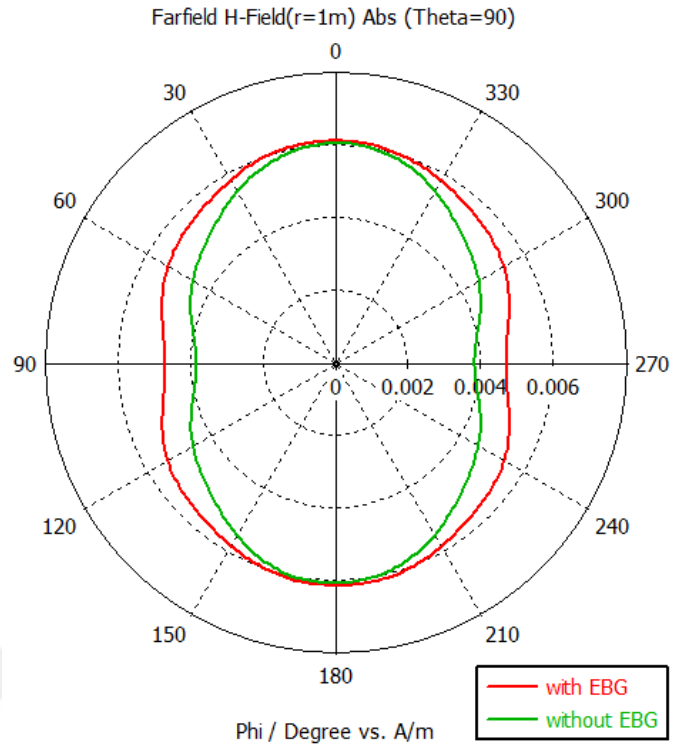


(b) Gain

Figure 4. 22 The radiation pattern compression between with and without EBG structure at 8.52 GHz, (a) directivity, (b) Gain.

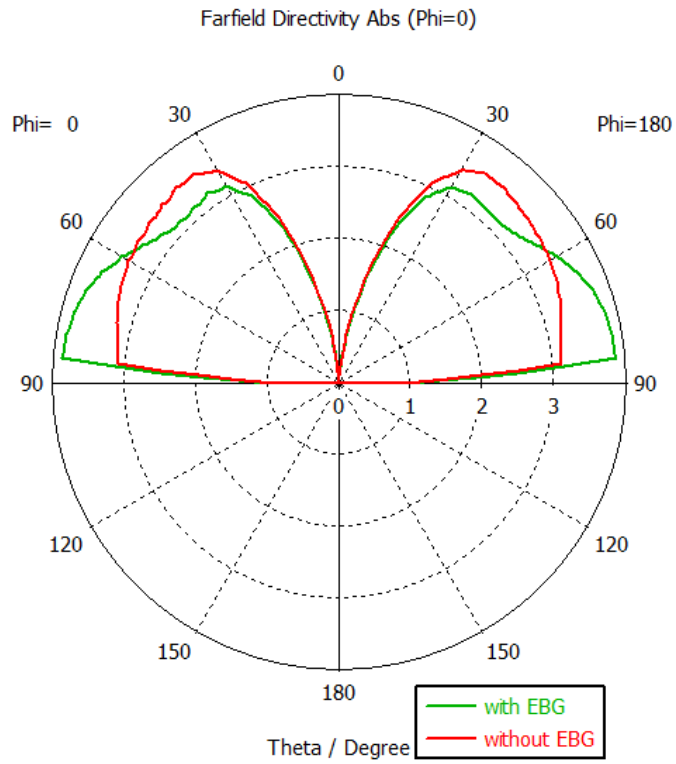


(a) E-Field

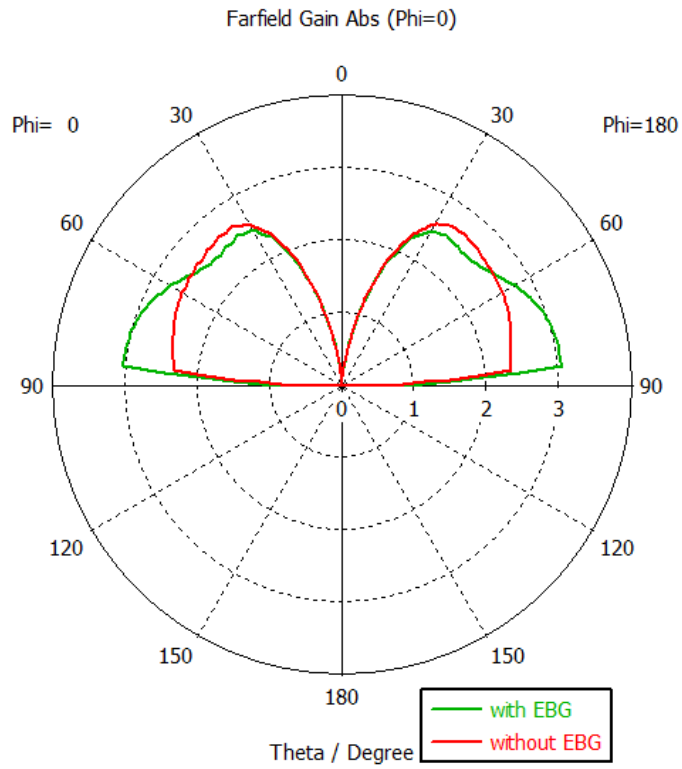


(b) H-Field

Figure 4. 23 The radiation pattern compression between with and without EBG structure at 8.52 GHz, a) E-Field, b) H-Field.

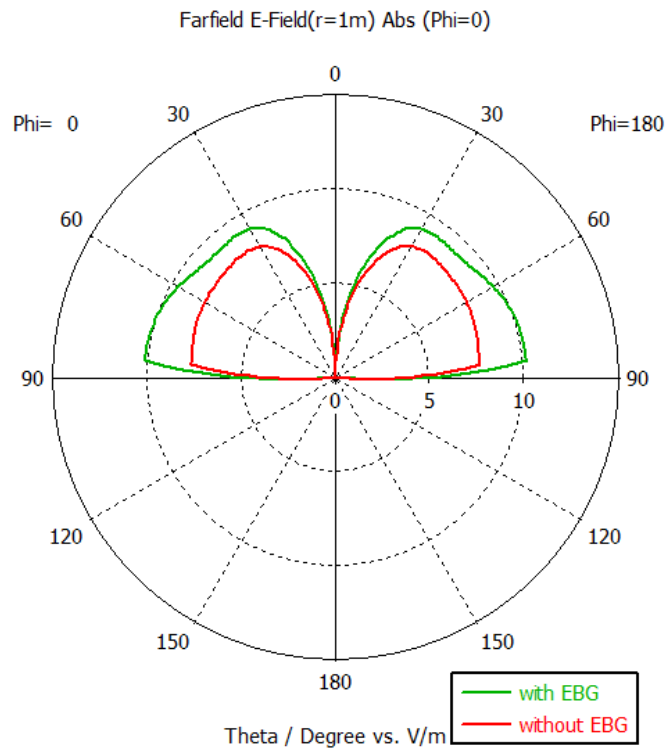


(a) Directivity

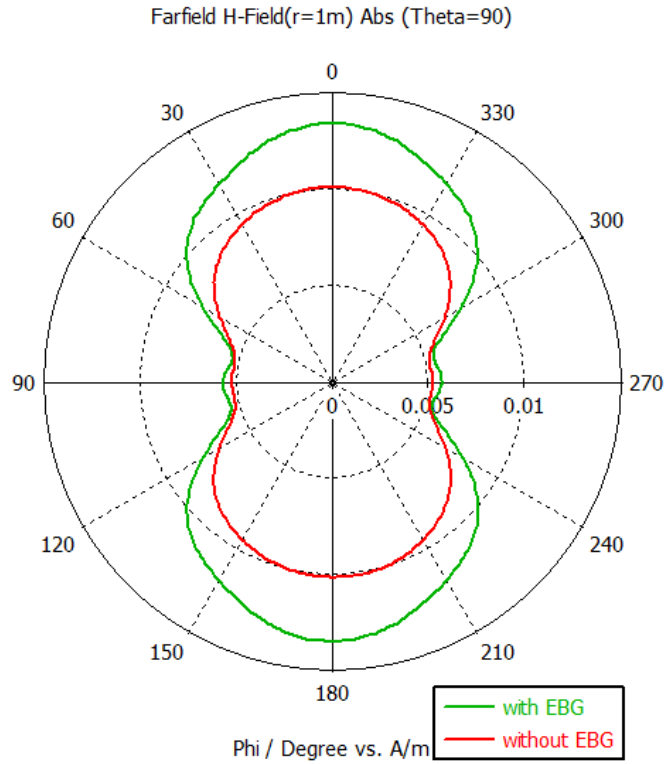


(b) Gain

Figure 4. 24 The radiation pattern compression between with and without EBG structure at 9.415 GHz, (a) directivity, (b) Gain.



(a) E-Field



(b) H-Field

Figure 4. 25 The radiation pattern compression between with and without EBG structure at 9.415 GHz, a) E-Field, b) H-Field.

Table 4. 1 Comparison Between 8.52 GHz and 9.415 GHz conventional and EBG's antenna.

Parameter	8.48 GHz without ENG	8.52 GHz with ENG	9.415 GHz without ENG	9.415 GHz with ENG
Coupling Coefficient, dB	-8.3	-48.2	-8.83	-40
Directivity, linear scaling	3.37	4.87	4.29	4.74
Gain, linear scaling	2.35	3.47	3.24	3.7
E-Field ,V/m	4.61	6.68	8.74	9.79
H-Field, A/m	0.0122	0.0177	0.0232	0.026

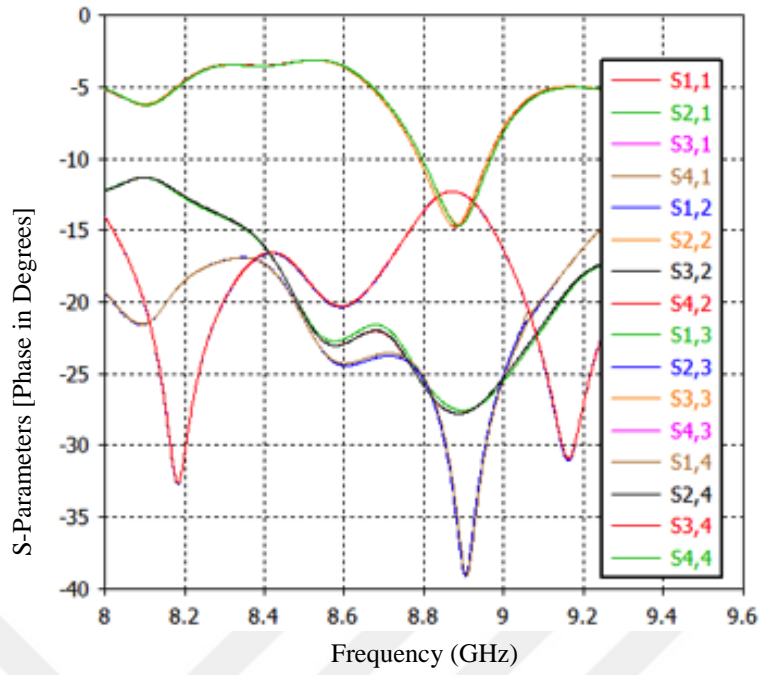
Table 4.1 shows the result summary compression of (coupling coefficient, Directivity, gain, E-Field, H-Field) for 8.52GHz and 9.415GHz resonant frequency.

4.2.5 Mutual Coupling Reduction of Dual-Band for Four Microstrip Antennas

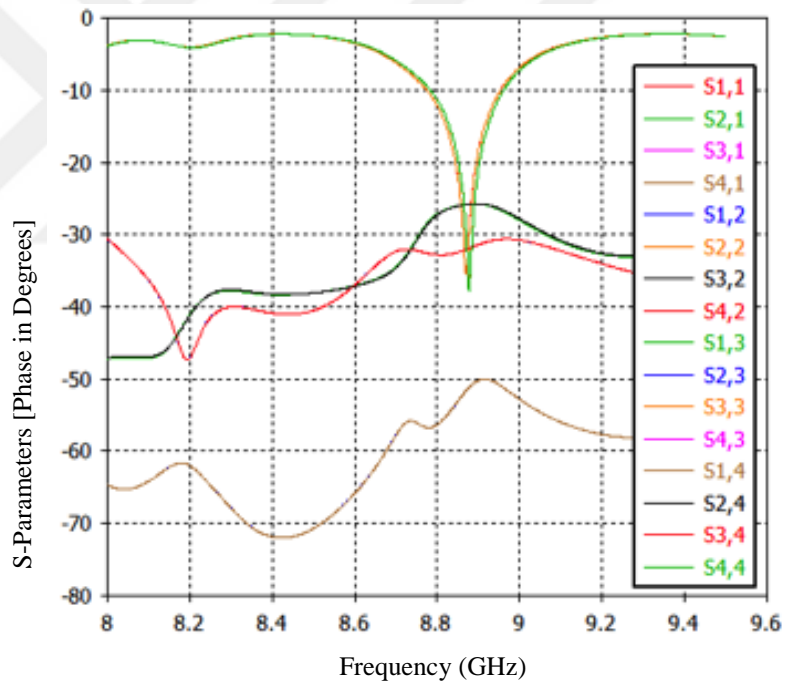
A high permittivity substrate exhibit at the E-plane coupled microstrip antennas have been founded and can provide very strong mutual coupling due to the severe surface wave. While the electromagnetic band-gap (EBG) structures have the capability to stop the propagation of the surface wave and reduce mutual coupling between antenna elements at certain operating frequency or in a specific band.

First, four conventional microstrip Antennas separated with 17.35mm Figure 3.14.a is simulated. It is observed that the antennas resonate around 8.87 GHz is -12.3dB coupling coefficient and the return loss equal to -14.75dB as shown in Figure 4.26.a,b respectively .





(a)

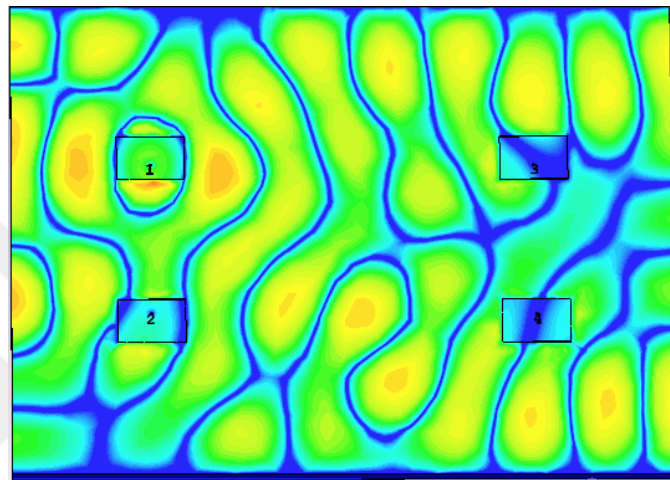


(b)

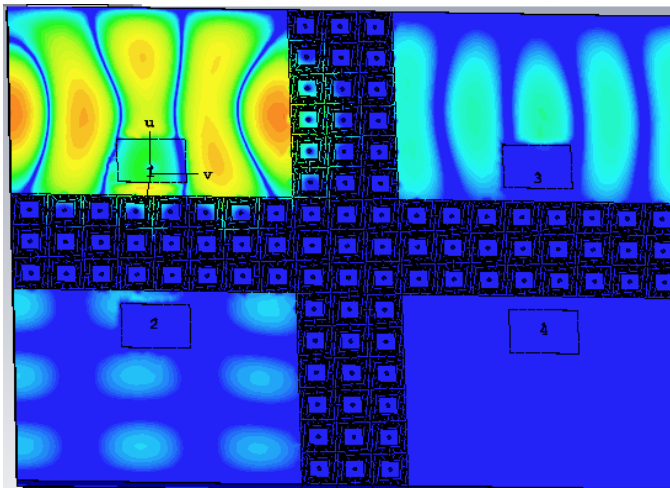
Figure 4. 26 The return loss and the coupling coefficient for the four coupling antennas S-parameters, a) w/o EBG, b) with EBG.

Second, three column of the proposed EBG has been inserted between the four microstrip Antennas Figure. 3.14.b, all structures parameters are shown in the Table 3.4 (see page 43), as the proposed EBG separation band is predicted, where it able to suppress surface waves, and exhibit a good isolation improvement (mutual coupling)

between the Antennas elements, Meanwhile, with the EBG structure the mutual coupling characteristics improved around the resonate frequencies 8.89 GHz to -35.5dB return loss and -32dB coupling coefficient. Although, concerning the EBG unit cell is a resonating element, the existence of the EBG structure has some effects on effective resonance frequency f_o position and shifted them. Figure 4.27.a, b, shows E-Field density with and without EBG structure existence and Figure 4.28.a, b, shows H-Field density with and without EBG structure existence.

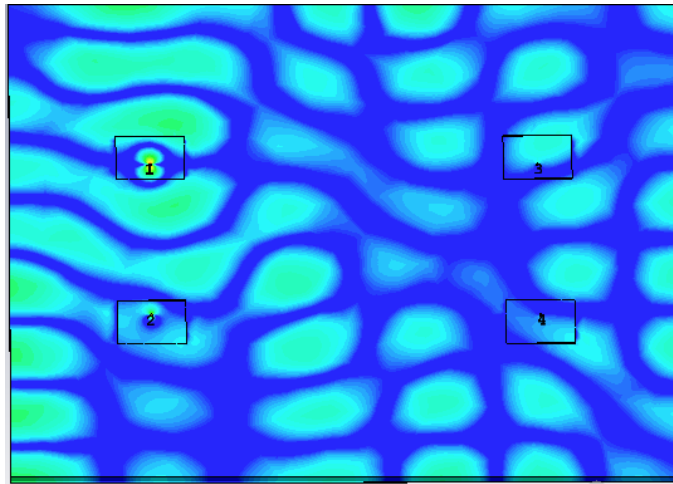


(a)

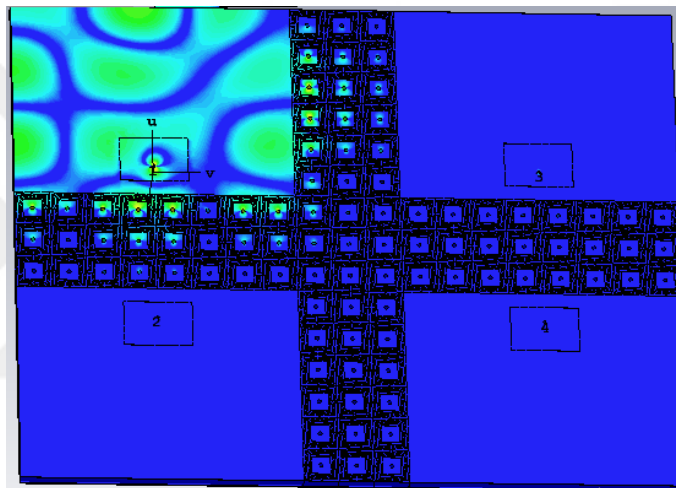


(b)

Figure 4. 27 E-field intensity, (a) without EBG, (b) with EBG at 8.89 GHz.



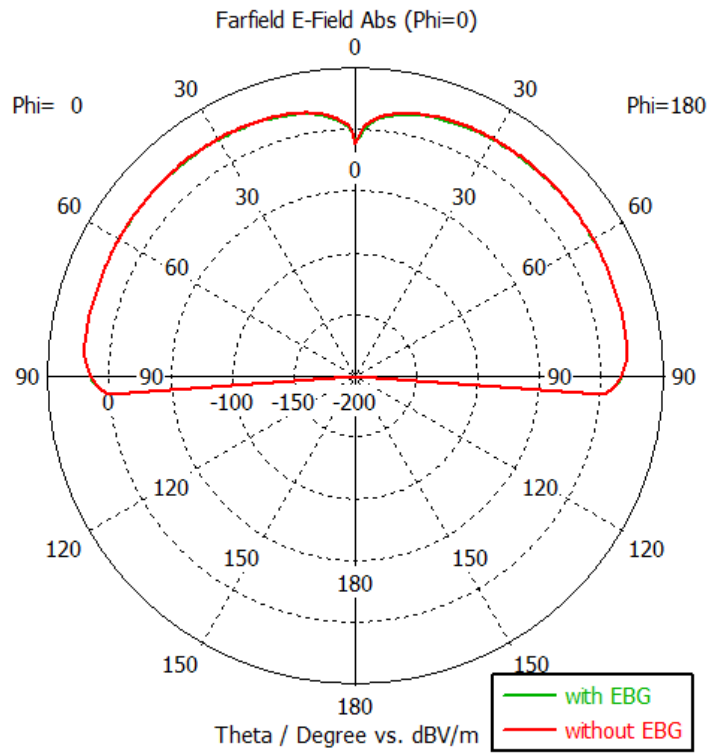
(a)



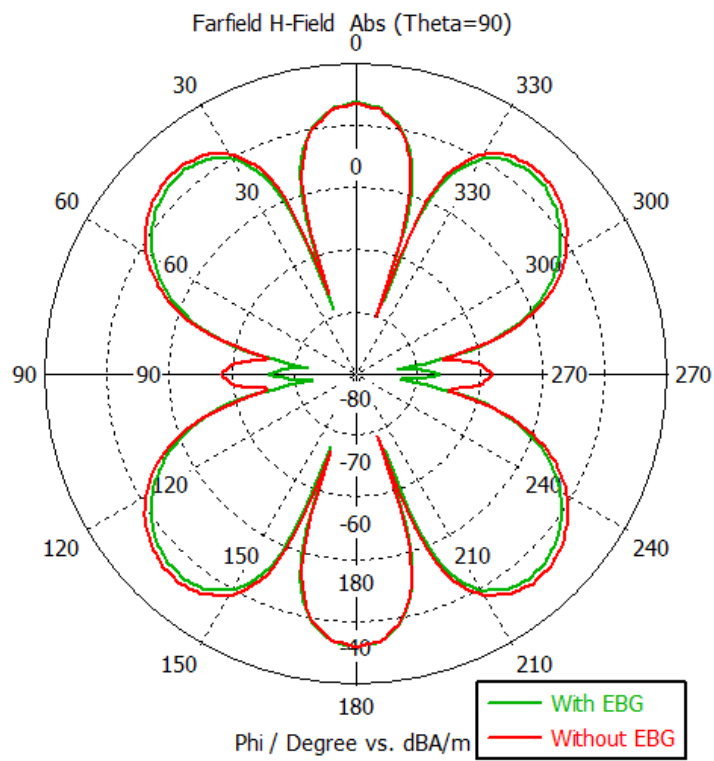
(b)

Figure 4.28 H-field intensity, (a) without EBG, (b) with EBG at 8.89 GHz.

It was clear that the E, H-Fields density has been reduced on the other antennas surfaces substrate due to the EBG structure effect. Which dictates the reduction in mutual coupling and improvement in the isolation between the array elements. Additionally, Figure 4.29 shows the radiation characteristics for the both array configurations. The radiation patterns are not disturbed after EBG structure existence and in considerable the patterns shapes although it is unchanged.



(a)



(b)

Figure 4. 29 The radiation pattern compression between with and without EBG structure (a) E-Field, (b) H-Field.

Table 4.2 Comparison Between with and without EBG structure at 8.89 GHz for a conventional four array microstrip antenna.

Parameter at 8.89 GHz	without EBG	with EBG
Coupling Coefficient, dB $S_{11}, S_{12}, S_{13}, S_{14}$	-14.9,-12.5,-27.2,-38 Respectively	-39,-26,-32,-50 Respectively
Directivity, linear scaling	6.9	7.41
Gain, linear scaling	5.06	5.51
E-Field ,V/m	13.7	13.4
H-Field, A/m	0.0355	0.0177

Table 4.2 shows the result summary compression of (coupling coefficient, Directivity, gain, E-Field, H-Field) for 8.89 GHz resonant frequency.

CHAPTER 5

CONCLUSION

The dissertation tackles two main designs, therefore the conclusion is divided into **A** and **B** regarding the two designs respectively:

A- The modified S-shaped of ring resonator in periodic arrangement is introduced and investigated both numerically and experimentally. Based on the obtained experiment results, it is found that:

1. The proposed metamaterial exhibits wideband DNG properties in the frequency band of interest.
2. The experimented novel LHMs is well designed and successfully worked around the operation frequency to provide simultaneously Double-negative permittivity and permeability and negative refraction index in X-Band Frequency.
3. The currents distribution which formed in the metal surfaces are anti-symmetric, lead current flow and concentrated on the border edge of metal sides and generate a magnetic reaction achieving a negative permeability, and the structure characteristics assisted the electric reaction to provide the negative permittivity.
4. Simple fabricating of this novel LHM is one of the design advantages.
5. An absorber application is simulated and the results of S-parameters, the absorption rate are provided for different polarization angles which can achieve high absorption for oblique incidence up to 40° and with absorption peak more than 90% (8.825-9) GHz. A perfect absorber can be obtained at the resonance frequency around 8.912 GHz. [94-101].
6. The unit cell low profile is smallest and ultrathin than previously proposed absorbers.
7. It is possible to use the proposed absorber promising applications for radar cross section (RCS) reduction in stealth technology and special filters.

B- The proposed Fishnet-Mushroom-like MTM is fabricated and measured.

The following conclusions are based on obtained results.

1. There were two cases of MTMs, the first one of which is a wide band negative-permittivity (between 8 and 10.95 GHz and between 11 and 12 GHz) and the second one is DNG (between 10.95 and 11 GHz, LH region and 10.975 GHz is indicated as transmission peak).
2. The electromagnetic behavior represented in S-parameters numerically and experimentally studied for the X-Band regime.
3. This structure can be used in wide band ENG applications such as efficient electrically small antenna enhancement applications, and also for double-negativity antenna and radar cross section (RCS) property enhancement applications. [102-104].
4. The structure simulated and the results compared with and without the array EBGs insertion for two and four array antenna. The final results for the two antenna structure shows near to -40dB reduction in mutual coupling improvement at 8.52GHz as will at 9.415GHz.simulatinuasly,and The final results for the four antenna structure shows near to -35.5dB return loss and -32dB coupling coefficient at resonate frequencies 8.89 GHz.

The contributions of this study started from pre-research task and the structure designs through its simulations that experimentally compared it was achieving its goals.

The contributions of this study started from pre-research task to the experimentally compared simulated structure designs are achieved its stated objectives.

CHAPTER 6

Future Research

The future work could include more detailed research about the inductance and capacitance that would be used in equal ratio to the impedance of free space, which is used in the design of different periodic structures, such as the existence of a multi-band gap, and higher-order bands and simultaneous EBG and AMC properties (to the best of the author's knowledge, this problem stills outstanding so far). The developed methodology could be a very helpful tool in the case of complex periodic structures. On the other hand, the use of superstrates in antenna technology is another interesting and perspective task. Due to the highly frequency dependent gain of the Superstrate, new alternatives should be explored to eliminate this drawback. Explore inductive and capacitive loading with their tenderness to limit the bandwidth; this could be done using the passive or active elements possible techniques.

In addition, studying the nature of these features, and their possible usefulness for electromagnetic devices can provide many opportunities for future research.

Finally, the methodology based on full-wave simulations in connection with optimization algorithms can be an effective and powerful tool in the hand of a designer to find the required solution for any type of complex electromagnetic problem.

REFERENCES

- [1] Sandora, J. (2012). Isolation Improvement with Electromagnetic Band Gap Surfaces. *Lincoln Laboratory Journal*, **19**(1).
- [2] Porter, J., Arzberger, P., Braun, H. W., Bryant, P., Gage, S., Hansen, T., Michener, W. (2005). Wireless sensor networks for ecology. *BioScience*, **55**(7), 561-572.
- [3] Bullock, T. H. (2005). Electoreception. Springer handbook of auditory research.
- [4] Thomson, J. J. (1893). Notes on recent researches in electricity and magnetism: intended as a sequel to Professor Clerk-Maxwell's Treatise on electricity and magnetism. Clarendon Press.
- [5] Keithley, J. F. (1999). The story of electrical and magnetic measurements: from 500 BC to the 1940s. *John Wiley & Sons*.
- [6] Kirby, Richard S. (1990). Engineering in History. *Courier Dover Publications*, 331–333.
- [7] Engheta, N., Ziolkowski, R. W. (2005). A positive future for double-negative metamaterials. *IEEE Transactions on Microwave Theory and Techniques*, **53**(4), 1535-1556.
- [8] Veselago, V. (1964). The Electrodynamics of Substances with Simultaneously egative. *Usp. Fiz. Nauk*, **92**, 517-526.
- [9] Pendry, J. B. (2000). Negative refraction makes a perfect lens. *Physical review letters*, **85**(18), 3966.
- [10] Smith, D. R., Padilla, W. J., Vier, D. C., Nemat-Nasser, S. C., Schultz, S. (2000). Composite medium with simultaneously negative permeability and permittivity. *Physical review letters*, **84**(18), 4184.
- [11] Kaharpardeshi, K. T., Ullah, S. U., Zafar, S. (2014). Influence of circular patched EBG substrate on SAR and far-field pattern of dipole phase-array antenna. In *Electrical, Electronics and Computer Science (SCEECS), 2014 IEEE Students' Conference on* (pp. 1-5). IEEE.
- [12] Rayleigh, L. (1885). On waves propagated along the plane surface of an elastic solid. *Proceedings of the London Mathematical Society*, **1**(1), 4-11.

- [13] Johnson, S. G., Joannopoulos, J. D. (2003). Introduction to photonic crystals: Bloch's theorem, band diagrams, and gaps (but no defects). *Photonic Crystal Tutorial*, 1-16.
- [14] Yablonovitch, E. (1987). Inhibited spontaneous emission in solid-state physics and electronics. *Physical review letters*, **58(20)**, 2059.
- [15] Johns, S. (1987). Strong localization of photons in certain disordered dielectric super-lattice. *Phys. Rev. Lett*, **58(23)**, 2486-2489.
- [16] Bowden, C. M., Dowling, J. P., Everitt, H. O. (1993). Development and Applications of Materials Exhibiting Photonic Band Gaps Introduction. *Journal of the Optical Society of America B Optical Physics*, **10**, 280-282.
- [17] Chang, C., Qian, Y., Itoh, T. (2003). Analysis and applications of uniplanar compact photonic bandgap structures. *Progress In Electromagnetics Research*, **41**, 211-235.
- [18] Pirhadi, A., Keshmiri, F., Hakkak, M., Tayarani, M. (2007). Analysis and design of dual band high directive EBG resonator antenna using square loop FSS as superstrate layer. *Progress In Electromagnetics Research*, **70**, 1-20.
- [19] Bell, J. M., Iskander, M. F. (2004). A low-profile Archimedean spiral antenna using an EBG ground plane. *IEEE Antennas and Wireless Propagation Letters*, **3(1)**, 223-226.
- [20] Stratton, J. A. *Electromagnetic Theory*. Wiley, 1941. Rayleigh, L. (1885). On waves propagated along the plane surface of an elastic solid. *Proceedings of the London Mathematical Society*, **1(1)**, 4-11.
- [21] Bell, J. M., Iskander, M. F., Lee, J. J. (2007). Ultrawideband hybrid EBG/ferrite ground plane for low-profile array antennas. *IEEE Transactions on Antennas and Propagation*, **55(1)**, 4-12.
- [22] Goussetis, G., Guo, Y., Feresidis, A. P., Vardaxoglou, J. C. (2004). Miniaturised and multiband artificial magnetic conductors and electromagnetic band gap surfaces. In *Antennas and Propagation Society International Symposium, 2004. IEEE*, **1**, pp. 293-296.
- [23] Mosallaei, H., Sarabandi, K. (2005). A compact wide-band EBG structure utilizing embedded resonant circuits. *IEEE Antennas and Wireless Propagation Letters*, **4(1)**, 5-8.
- [24] Tse, S., Izquierdo, B. S., Batchelor, J. C., Langley, R. J. (2003). Reduced sized

- cells for high impedance (HIP) ground planes. In *Antennas and Propagation, 2003.(ICAP 2003). Twelfth International Conference on (Conf. Publ. No. 491)*, **Vol. 2**, pp. 473-476. IET.
- [25] Yang, L., Feng, Z., Chen, F., Fan, M. (2004). A novel compact electromagnetic band-gap (EBG) structure and its application in microstrip antenna arrays. In *Microwave Symposium Digest, 2004 IEEE MTT-S International*, **Vol. 3**, pp. 1635-1638. IEEE.
- [26] Shaker, G. S., Safavi-Naeini, S. (2005). A novel approach for designing miniaturized artificial magnetic conductors (AMCs) and electromagnetic band gap structures (EBGs). In *Antennas and Propagation Society International Symposium, 2005 IEEE*, **Vol. 3**, pp. 770-773. IEEE.
- [27] Shaker, G. S., Safavi-Naeini, S. (2005). Reduced size Electromagnetic Band Gap (EBG) structures for antenna applications. In *Electrical and Computer Engineering, 2005. Canadian Conference on* (pp. 1198-1201). IEEE.
- [28] Yang, L., Feng, Z. (2004). Advanced methods to improve compactness in EBG design and utilization. In *Antennas and Propagation Society International Symposium, 2004. IEEE*, **Vol. 4**, pp. 3585-3588. IEEE.
- [29] Sievenpiper, D., Zhang, L., Broas, R. F., Alexopolous, N. G., Yablonovitch, E. (1999). High-impedance electromagnetic surfaces with a forbidden frequency band. *IEEE Transactions on Microwave Theory and techniques*, **47(11)**, 2059-2074.
- [30] Zheng, Q. R., Yan, Y. M., Cao, X. Y., Yuan, N. C. (2008). High impedance ground plane (HIGP) incorporated with resistance for radar cross section (RCS) reduction of antenna. *Progress In Electromagnetics Research*, **84**, 307-319.
- [31] Gurwinder S. R., Anupma M. (2015). A Review of Metamaterials and its Applications. *International Journal of Engineering Trends and Technology (IJETT)* – **Vol. 19**, No. 6.
- [32] Tung, N. T., Lam, V. D., Cho, M. H., Park, J. W., Jang, W. H., Lee, Y. P. (2009). Influence of the dielectric-spacer thickness on the left-handed behavior of fishnet metamaterial structure. *Photonics and Nanostructures-Fundamentals and Applications*, **7(4)**, 206-211.
- [33] Chappell, W. J., Gong, X. (2003). Wide bandgap composite EBG substrates. *IEEE Transactions on Antennas and Propagation*, **51(10)**, 2744-2750.
- [34] Shelby, R. A., Smith, D. R., Nemat-Nasser, S. C., Schultz, S. (2001). Microwave transmission through a two-dimensional, isotropic, left-handed metamaterial. *Applied Physics Letters*, **78(4)**, 489-491.

- [35] Joannopoulos, John D., Steven G. Johnson, Joshua N. Winn, and Robert D. Meade. (2011). *Photonic crystals: molding the flow of light*. Princeton university press.
- [36] S. Germani, L. Minelli, M. Bozzi, and L. Perregrini, and P. de Maagt, (2004). Modelling of MD-EBG by the Mom/BI-REM Method. *27th ESA Antenna Workshop on Innovative Periodic Antennas, PROCEEDINGS ESA WPP-222*.
- [37] Axmann, W., Kuchment, P., Kuyansky, L. (1999). Asymptotic methods for thin high-contrast two-dimensional PBG materials. *Journal of Lightwave Technology*, 17(11), 1996-2007.
- [38] Thevenot, M., Cheype, C., Reineix, A., & Jecko, B. (1999). Directive photonic-bandgap antennas. *IEEE Transactions on microwave theory and techniques*, 47(11), 2115-2122.
- [39] Meade, R. D., Brommer, K. D., Rappe, A. M., Joannopoulos, J. D. (1991). Photonic bound states in periodic dielectric materials. *Physical Review B*, 44(24), 13772.
- [40] Halim, S. B. (2007). Antenna with metamaterial design. *Universiti Teknologi Malaysia*. [L¹SEP]
- [41] Stratton, J. A., 1941. *Electromagnetic Theory*. Wiley.
- [42] Smith, D. R., Kroll, N. (2000). Negative refractive index in left-handed materials. *Physical Review Letters*, 85(14), 2933.
- [43] Kolinko, P., Smith, D. R. (2003). Numerical study of electromagnetic waves interacting with negative index materials. *Optics Express*, 11(7), 640-648.
- [44] Sanada, A. (2005). Planar single-and double negative metamaterial implementations and applications. URSI .
- [45] Mahmoud, S. F. (2004). A new miniaturized annular ring patch resonator partially loaded by a metamaterial ring with negative permeability and permittivity. *IEEE Antennas and Wireless Propagation Letters*, 3(1), 19-22.
- [46] Gündüz, S., Çakır, M., Çakır, G., Sevgi, L. (2007). Metamaterials and FDTD based numerical modeling studies. In *ELECO 2007* (pp. 6-10).
- [47] Moura-tiago, T. A. M. Metamaterials and Double Negative (DNG) Media: General Properties of Unbounded Media and Guided Wave Propagation.
- [48] Joannopoulos, J. D., Johnson, S. G., Winn, J. N., Meade, R. D. (2011). *Photonic crystals: molding the flow of light*. Princeton university press.

- [49] Johnson, S. G., Joannopoulos, J. D. (2003). Introduction to photonic crystals: Bloch's theorem, band diagrams, and gaps (but no defects). *Photonic Crystal Tutorial*, 1-16.
- [50] Kumar, A., Majumder, A., Das, S., Kar, S. (2013). Simulation based characterization of negative permeability plasmonic structures at X band. In *Science and Information Conference (SAI), 2013* (pp. 675-679). IEEE.
- [51] Yao, Y., Wang, X., Feng, Z. (2006). A novel dual-band compact electromagnetic bandgap (EBG) structure and its application in multi-antennas. In *Antennas and Propagation Society International Symposium 2006, IEEE* (pp. 1943-1946). IEEE.
- [52] Sadeghzadeh, R. A., Khajehmohammadlou, R., Jalali, M. (2013). A novel high directive EBG structure and metamaterial superstrate for microstrip antenna. *International Journal of Engineering Science & Emerging Technologies*, **4(2)**, 1-12.
- [53] Palikaras, G. K., Feresidis, A. P., & Parini, C. G. (2011). Advances in conformal metamaterial antennas using High Impedance (HIS) and Electromagnetic Bandgap (EBG) surfaces. In *Antennas and Propagation (EUCAP), Proceedings of the 5th European Conference on* (pp. 3466-3469). IEEE.
- [54] Brown, E. R., Parker, C. D., Yablonovitch, E. (1993). Radiation properties of a planar antenna on a photonic-crystal substrate. *JOSA B*, **10(2)**, 404-407.
- [55] Sievenpiper, D., Zhang, L., Broas, R. F., Alexopolous, N. G., & Yablonovitch, E. (1999). High-impedance electromagnetic surfaces with a forbidden frequency band. *IEEE Transactions on Microwave Theory and techniques*, **47(11)**, 2059-2074.
- [56] Collin, R. E. (1991). *Field Theory of Guided Waves* 2nd edn (New York: IEEE).
- [57] Pozar, D. (1982). Input impedance and mutual coupling of rectangular microstrip antennas. *IEEE Transactions on Antennas and Propagation*, **30(6)**, 1191-1196.
- [58] Institute of Electrical and Electronics Engineers. (1983). *IEEE Standard Definitions of Terms for Antennas*. IEEE.
- [59] Segovia-Vargas, D., Martin-Cuerdo, R., Sierra-Perez, M. (2002). Mutual coupling effects correction in microstrip arrays for direction-of-arrival (DOA) estimation. *IEE Proceedings-Microwaves, Antennas and Propagation*, **149(2)**, 113-118.
- [60] Wallace, J. W., Jensen, M. A. (2004). Mutual coupling in MIMO wireless systems: A rigorous network theory analysis. *IEEE Transactions on Wireless Communications*, **3(4)**, 1317-1325.

- [61] Qiu, L., Zhao, F., Xiao, K., Chai, S. L., Mao, J. J. (2012). Transmit–receive isolation improvement of antenna arrays by using EBG structures. *IEEE Antennas and Wireless Propagation Letters*, **11**, 93-96.
- [62] Shelby, R. A., Smith, D. R., Nemat-Nasser, S. C., Schultz, S. (2001). Microwave transmission through a two-dimensional, isotropic, left-handed metamaterial. *Applied Physics Letters*, **78**(4), 489-491.
- [63] Ziolkowski, R. W., Kipple, A. D. (2003). Application of double negative materials to increase the power radiated by electrically small antennas. *IEEE Transactions on Antennas and Propagation*, **51**(10), 2626-2640. [11]
- [64] McVay, J., Engheta, N., & Hoorfar, A. (2004). High impedance metamaterial surfaces using Hilbert-curve inclusions. *IEEE Microwave and Wireless components letters*, **14**(3), 130-132.
- [65] Sadeghzadeh, R. A., Khajehmohammadlou, R., Jalali, M. (2013). A novel high directive EBG structure and metamaterial superstrate for microstrip antenna. *International Journal of Engineering Science & Emerging Technologies*, **4**(2), 1-12.
- [66] Kaabal, A., Ahyoud, S., Asselman, A. (2016). A Low Mutual Coupling Design for Array Microstrip Antennas Integrated with Electromagnetic Band-Gap Structures. *Procedia Technology*, **22**, 549-555.
- [67] Abdel-Rahman, A. B., Bakry, M. (2013). B4. Coupling Reduction Between Microstrip Antenna Array Elements Using Metamaterial. In *Radio Science Conference (NRSC), 2013 30th National* (pp. 40-47). IEEE.
- [68] Gangwar, D., Das, S., Yadava, R. L. (2014). Reduction of Mutual Coupling in Metamaterial Based Microstrip Antennas: The Progress in Last Decade. *Wireless personal communications*, **77**(4), 2747-2770.
- [69] Mackenzie, A. I. (2015). Microwave band gaps produced by varying numbers of mushroom metamaterial cells. In *Antennas and Propagation & USNC/URSI National Radio Science Meeting, 2015 IEEE International Symposium on* (pp. 1102-1103). IEEE.
- [70] Sandora, J. (2012). Isolation improvement with electromagnetic band gap surfaces. *Lincoln Laboratory Journal*, **19**(1).
- [71] Goswami, C., Pal, M., Ghatak, R., Poddar, D. R. (2014, December). Metamaterial based miniaturized dual band antenna. In *Emerging Technology Trends in Electronics, Communication and Networking (ET2ECN), 2014 2nd International Conference on* (pp. 1-4). IEEE.

- [72] Nicolson, A. M., Ross, G. F. (1970). Measurement of the intrinsic properties of materials by time-domain techniques. *IEEE Transactions on instrumentation and measurement*, **19(4)**, 377-382.
- [73] Weir, W. B. (1974). Automatic measurement of complex dielectric constant and permeability at microwave frequencies. *Proceedings of the IEEE*, **62(1)**, 33-36.
- [74] Milosevic, V., Jokanovic, B., Bojanic, R. (2013). Effective electromagnetic parameters of metamaterial transmission line loaded with asymmetric unit cells. *IEEE Transactions on Microwave Theory and Techniques*, **61(8)**, 2761-2772.
- [75] Mahmood, A., Ögücü Yetkin, G., Sabah, C. (2017). Design and Fabrication of a Novel Wideband DNG Metamaterial with the Absorber Application in Microwave X-Band. *Advances in Condensed Matter Physics*, 2017.
- [76] Consultants from metamaterial laboratory group in Iskenderun Teknik University/Turkey, <https://metamaterialgroup.wixsite.com>.
- [77] Mackenzie, A. I. (2015, March). Comparison of two AMC's on a high-permittivity substrate. In *Applied Computational Electromagnetics (ACES), 2015 31st International Review of Progress in* (pp. 1-2). IEEE.
- [78] Mackenzie, A. I. (2015). Microwave band gaps produced by varying numbers of mushroom metamaterial cells. In *Antennas and Propagation & USNC/URSI National Radio Science Meeting, 2015 IEEE International Symposium on* (pp. 1102-1103). IEEE.
- [79] Mahmood, A., Ogucu Yetkin, G., Sabah, C. (2017). Wideband Negative Permittivity and Double Negative Fishnet-Mushroom-Like Metamaterial in X-Band Waveguide. *Advances in Condensed Matter Physics*, 2017.
- [80] Sabah, C. (2016). Realization of polarization-angle-independent fishnet-based waveguide metamaterial comprised of octagon shaped resonators with sensor and absorber applications. *Journal of Materials Science: Materials in Electronics*, **27(5)**, 4777-4787.
- [81] S. Sahandabadi, F.H. Kashani and M. Fallah. (2014). Sierpinski Triangular Antenna on a Mushroom-like EBG Metamaterial Ground Plane. *Journal Of Telecommunication*, **Vol. 23**, Issue 2.
- [82] Aravind, V. S., Gupta, S. (2014). Compact EBG ground plane microstrip antenna for high gain applications. In *Emerging Technology Trends in Electronics*,

Communication and Networking (ET2ECN), 2014 2nd International Conference on (pp. 1-3). IEEE.

- [83] Segovia-Vargas, D., Martin-Cuerdo, R., Sierra-Perez, M. (2002). Mutual coupling effects correction in microstrip arrays for direction-of-arrival (DOA) estimation. *IEE Proceedings-Microwaves, Antennas and Propagation*, **149(2)**, 113-118.
- [84] Chen, H., Ran, L. X., Huang-Fu, J. T., Zhang, X. M., Chen, K. S., Grzegorzczk, T. M., Kong, J. A. (2005). Magnetic properties of S-shaped split-ring resonators. *Progress In Electromagnetics Research*, **51**, 231-247.
- [85] Horestani, A. K., Duran-Sindreu, M., Naqui, J., Fumeaux, C., Martin, F. (2014). Coplanar waveguides loaded with s-shaped split-ring resonators: modeling and application to compact microwave filters. *IEEE Antennas and Wireless Propagation Letters*, **13**, 1349-1352.
- [86] Landy, N. I., Sajuyigbe, S., Mock, J. J., Smith, D. R., Padilla, W. J. (2008). Perfect metamaterial absorber. *Physical review letters*, **100(20)**, 207402.
- [87] Lam, V. D., Kim, J. B., Lee, S. J., Lee, Y. P. (2008). Left-handed behavior of combined and fishnet structures. *Journal of Applied Physics*, **103(3)**, 033107.
- [88] Aydin, K., Li, Z., Sahin, L., Ozbay, E. (2008). Negative phase advance in polarization independent, multi-layer negative-index metamaterials. *Optics Express*, **16(12)**, 8835-8844.
- [89] Tung, N. T., Lam, V. D., Cho, M. H., Park, J. W., Jang, W. H., Lee, Y. P. (2009). Influence of the dielectric-spacer thickness on the left-handed behavior of fishnet metamaterial structure. *Photonics and Nanostructures-Fundamentals and Applications*, **7(4)**, 206-211.
- [90] Islam, S. S., Faruque, M. R. I., Islam, M. T. (2014). The design and analysis of a novel Split-H-Shaped metamaterial for multi-band microwave applications. *Materials*, **7(7)**, 4994-5011.
- [91] Sabah, C., Cakmak, A. O., Ozbay, E., Uckun, S. (2010). Transmission measurements of a new metamaterial sample with negative refraction index. *Physica B: Condensed Matter*, **405(14)**, 2955-2958.
- [92] Tung, N. T., Lam, V. D., Park, J. W., Cho, M. H., Rhee, J. Y., Jang, W. H., Lee, Y. P. (2009). Single-and double-negative refractive indices of combined metamaterial structure. *Journal of Applied Physics*, **106(5)**, 053109.

- [93] Sabah, C., Roskos, H. G. (2011). Numerical and experimental investigation of fishnet-based metamaterial in a X-band waveguide. *Journal of Physics D: Applied Physics*, **44(25)**, 255101.
- [94] Dincer, F., Akgol, O., Karaaslan, M., Unal, E., Sabah, C. (2014). Polarization angle independent perfect metamaterial absorbers for solar cell applications in the microwave, infrared, and visible regime. *Progress In Electromagnetics Research*, **144**, 93-101.
- [95] Sabah, C. (2012). Electric and magnetic excitations in anisotropic broadside-coupled triangular-split-ring resonators. *Applied Physics A*, **108(2)**, 457-463.
- [96] Ghosh, S., Bhattacharyya, S., Kaiprath, Y., Vaibhav Srivastava, K. (2014). Bandwidth-enhanced polarization-insensitive microwave metamaterial absorber and its equivalent circuit model. *Journal of Applied Physics*, **115(10)**, 104503.
- [97] Ghosh, S., Bhattacharyya, S., Srivastava, K. V. (2013). Design of a bandwidth-enhanced ultra thin metamaterial absorber. In *PIERS Proceedings*, **Vol. 2**, pp. 1097-1101.
- [98] Yoo, M., Lim, S. (2014). Polarization-independent and ultra wideband metamaterial absorber using a hexagonal artificial impedance surface and a resistor-capacitor layer. *IEEE transactions on antennas and propagation*, **62(5)**, 2652-2658.
- [99] Sabah, C., Urbani, F. (2013). Experimental analysis of Λ -shaped magnetic resonator for mu-negative metamaterials. *Optics Communications*, **294**, 409-413.
- [100] Sabah, C., Turkmen-Kucuksari, O., Turhan-Sayan, G. (2014). Metamaterial absorber-based sensor embedded into X-band waveguide. *Electronics Letters*, **50(15)**, 1074-1076.
- [101] Abdalla, M. A., Hu, Z. (2012). On The Study of Development of X Band Metamaterial Radar Absorber. *Advanced Electromagnetics*, **1(3)**, 94-98.
- [102] Gunduz, O. T., & Sabah, C. (2015). Alternative design of left-handed metamaterial based on circular resonator and wire strip for waveguide configurations with sensing and absorber applications. *Optical Engineering*, **54(8)**, 087101-087101.
- [103] Kafesaki, M., Tsiapa, I., Katsarakis, N., Koschny, T., Soukoulis, C. M., Economou, E. N. (2007). Left-handed metamaterials: The fishnet structure and its variations. *Physical Review B*, **75(23)**, 235114.
- [104] Tung, N. T., Lam, V. D., Park, J. W., Cho, M. H., Rhee, J. Y., Jang, W. H., Lee, Y. P. (2009). Single-and double-negative refractive indices of combined metamaterial structure. *Journal of Applied Physics*, **106(5)**, 053109.



CURRICULUM VITAE

PERSONAL INFORMATION

Name and Surname: Ahmed Mamoon Mahmood Al-Kadi

Nationality: Republic of Iraq

Birth place and Date: Iraq, 1974

Phone number: +905417230730

Email: metamaterial74@gmail.com

EDUCATION

	Graduate school	Year
Master	University of Technology/ Laser Engineering	2004
Bachelor	University of Al-Rasheed/ General Electric Engineering	1997
High School	Baghdad College High School	1992

WORKING EXPERIENCE

	Place	Enrollment
2007-2010	University of Salahaddin/ Electric & Electronic Engineering	Lecturer
2006-2007	University of Al Mustansiriya / Electric & Electronic Engineering	Lecturer
1998-2003	Ministry of Defense/	Radar Maintenance Engineering

PUBLICATIONS

1. Mahmood, A., Yetkin, G. Ö, Sabah, C. (2017). Design and Fabrication of a Novel Wideband DNG Metamaterial with the Absorber Application in Microwave X-Band, *Advances in Condensed Matter Physics*, Article ID 1279849, 8 pages.
2. Mahmood, A., Ogucu Yetkin, G., Sabah, C. (2017). Wideband Negative Permittivity and Double Negative Fishnet-Mushroom-Like Metamaterial in X-

Band Waveguide, *Advances in Condensed Matter Physics*, Article ID 2439518, 7 pages.

Languages

Arabic, English, and Turkish.

